On localization of Dirac fermions by disorder

Proefschrift

ter verkrijging van
de graad van Doctor aan de Universiteit Leiden,
op gezag van de Rector Magnificus
prof. mr P. F. van der Heijden,
volgens besluit van het College voor Promoties
te verdedigen op dinsdag 3 mei 2011
te klokke 15.00 uur

door

Mariya Vyacheslavivna Medvedyeva

geboren te Dnipropetrovsk, Oekraïne in 1985

Promotiecommissie

Promotor:	prof. dr. C. W. J. Beenakker
Co-Promotor:	dr. Ya. M. Blanter (Technische Universiteit Delft)
Co-Promotor:	dr. J. Tworzydło (Universiteit Warschau)
Overige leden:	prof. dr. A. Achúcarro
	prof. dr. E. R. Eliel
	prof. dr. A. D. Mirlin (Universiteit Karlsruhe)
	prof. dr. J. M. van Ruitenbeek
	prof. dr. ir. H. S. J. van der Zant (Technische Universiteit Delft)

Casimir PhD Series, Delft-Leiden, 2011-09
ISBN 978-90-8593-099-0

Dit werk maakt deel uit van het onderzoekprogramma van de Stichting voor Fundamenteel Onderzoek der Materie (FOM), die deel uit maakt van de Nederlandse Organisatie voor Wetenschappelijk Onderzoek (NWO).

This work is part of the research programme of the Foundation for Fundamental Research on Matter (FOM), which is part of the Netherlands Organisation for Scientific Research (NWO).

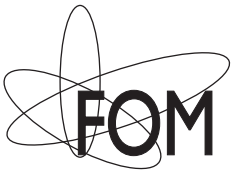

Cover: Artistic impression of the phase diagram of Dirac fermions in symmetry class D and of Majorana-Shockley bound states on the lattice, as it is calculated in chapter 2 of this thesis (see Fig. 2.1) and in chapter 4 (see Fig. 4.4) respectively.

to my Father, Mother,
Grandfather, Grandmothers,
Sister, Uncle,
and to all other people, whom I call my Family

моей Семье

Optimism is the faith that leads to achievement.
Nothing can be done without hope and confidence.
Albert Einstein

Contents

Chapter 1

Introduction

1.1 Preface

Nonrelativistic quantum mechanics is based on the Schrödinger equation, which describes particles with a quadratic dependence of energy on momentum. Conduction electrons in metals and semiconductors follow this equation. The effective mass is different from the free electron mass, due to the effect of the lattice potential, but it does not vanish.

In recent years materials were discovered in which the energy of excitations near the Fermi level depends linearly rather than quadratically on momentum. This is the same linear dispersion relation as for photons, so these materials mimic the dynamics of massless relativistic particles (although the Fermi velocity is much less than the speed of light). The excitations could be electrons or holes in a carbon monolayer (graphene), or they could be neutral quasiparticle excitations in an unconventional superconductor (with p-wave or d-wave symmetry of the order parameter).

The massless excitations are called Dirac fermions, because they satisfy a Dirac equation rather than a Schrödinger equation. The Dirac equation was studied extensively in the context of relativistic quantum mechanics, but questions related to the effect of disorder did not play a role in that context. These effects are, however, central to the behavior of Dirac fermions in condensed matter.

Localization is a purely quantum mechanical effect of disorder, discovered by P.W. Anderson in 1958 [7]. Interference prevents the spreading of a wave packet, turning a metal into an insulator. This effect is now well understood, both by an intuitive scaling theory [1] and by field theoretical

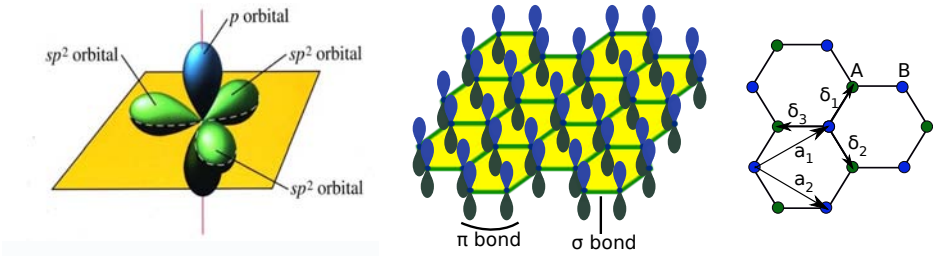

Figure 1.1. The left panel shows the sp^2-hybridized orbitals of a carbon atom, the central panel shows their arrangement in a honeycomb lattice known as graphene. The right panel shows the A and B sublattices that form the honeycomb lattice, with lattice vectors $\boldsymbol{a}_1$, $\boldsymbol{a}_2$ and nearest neighbor vectors $\boldsymbol{\delta}_1$, $\boldsymbol{\delta}_2$, $\boldsymbol{\delta}_3$. From Ref. [22].

approaches [125]. It has been tested by numerical simulations [65] and by experiments [37].

These studies considered massive electrons, starting from the Schrödinger equation. Localization of massless Dirac fermions is qualitatively different. Some aspects of the localization of Dirac fermions are studied in this thesis.

In this introductory chapter we present background material, and an outline of the following chapters. We start by introducing the physical realizations of Dirac fermions that we will be considering.

1.2 Dirac fermions in graphene

1.2.1 Gapless graphene

Graphene is a monolayer of graphite. The atomic configuration of the carbon atoms is $1s^2 2s^2 2p^2$, in graphene their electronic configuration is $1s^2 2s 2p^3$. Due to sp^2-hybridization the atoms form a hexagonal lattice (σ-bonds), see Fig. 1.1. The p_z orbitals do not participate in the hybridization (π-bond). Electrical conduction is due to hopping between the p_z orbitals.

The unit cell of the hexagonal lattice consists of two atoms, which form the A and B sublattices. The tight-binding model with nearest neighbor hopping only couples different sublattices, corresponding to the

off-diagonal blocks in the Hamiltonian

$$\mathcal{H} = \begin{pmatrix} 0 & t^* \sum_{j=1,2,3} \exp(-i\boldsymbol{k}\cdot\boldsymbol{\delta}_j) \\ t \sum_{j=1,2,3} \exp(i\boldsymbol{k}\cdot\boldsymbol{\delta}_j) & 0 \end{pmatrix}. \tag{1.1}$$

The $\boldsymbol{\delta}_j$'s are three nearest neighbor vectors,

$$\boldsymbol{\delta}_1 = \frac{a}{2}(1,\sqrt{3}), \quad \boldsymbol{\delta}_2 = \frac{a}{2}(1,-\sqrt{3}), \quad \boldsymbol{\delta}_3 = a(1,0),$$

$a \approx 1.42$ Å is the lattice constant, and $t \approx 2.8$ eV is the nearest neighbor hopping energy.

The Hamiltonian (1.1) has energy bands $E(\boldsymbol{k})$ given by

$$E = \pm t \sqrt{3 + 2\cos\sqrt{3}k_y a + 4\cos\frac{\sqrt{3}k_y a}{2}\cos\frac{3k_x a}{2}}. \tag{1.2}$$

At the points

$$K = \left(\frac{2\pi}{3a}, \frac{2\pi}{3\sqrt{3}a}\right), \quad K' = \left(\frac{2\pi}{3a}, -\frac{2\pi}{3\sqrt{3}a}\right)$$

the gap in the spectrum is closed. Near these two socalled Dirac points the energy-momentum relation is linear.

Linearization of the tight-binding Hamiltonian near a Dirac point gives the two-dimensional massless Dirac Hamiltonian,

$$\mathcal{H} = \hbar v_F \begin{pmatrix} 0 & \delta k_x \mp i\delta k_y \\ \delta k_x \pm i\delta k_y & 0 \end{pmatrix}, \tag{1.3}$$

which can be written more compactly in terms of Pauli matrices,

$$\mathcal{H} = \hbar v_F (\sigma_x \delta k_x \pm \sigma_y \delta k_y). \tag{1.4}$$

The wave vector $\delta\boldsymbol{k}$ is measured relative to point K (upper sign) or relative to point K' (lower sign). The Fermi velocity v_F is expressed through the parameters of the lattice as $v_F = 3at/2 \approx 10^6$ m/s. This is relatively large, but still much smaller than the speed of light, so the dynamics only mimics that of relativistic particles.

The literature on graphene has exploded, since the first isolation of carbon monolayers in 2004 by A. K. Geim and K. S. Novoselov with their group (recently honored by a Nobel prize). We refer to a comprehensive review [22] for references.

1.2.2 Gapped graphene

The relatively large Fermi velocity in graphene is promising for transistor applications, but the absence of a band gap is a complication: It is impossible to completely switch off the conductivity. A band gap is represented by an additional term $mv_F^2\sigma_z$ in Dirac equation, which in the relativistic analogue would correspond to a mass term,

$$\mathcal{H} = mv_F^2\sigma_z + \hbar v_F(\sigma_x\delta k_x \pm \sigma_y\delta k_y). \tag{1.5}$$

The physical meaning of this term is a potential which takes on different values on the two sublattices. Such a staggered potential can be imposed on graphene in different ways, for example, by chemisorption of atoms to the π-bonds or by a substrate.

Let us consider the first possibility in some more detail [27]. We assume that the adatom deposited on graphene forms a covalent bond with a particular carbon atom (fluorine, hydrogen, or hedroxyl groups are known to act like this). Then the sublattice symmetry is locally broken. In general the concentration of adatoms on the two sublattices is almost equivalent. But spontaneous sublattice symmetry breaking can happen if it is energetically more favorable for adatoms to be on the same sublattice. Namely, each adsorbent locally changes the electronic density and interacts via this change of electronic density with another adatom, in such a way that the interaction depends on which sublattice the adatom is placed.

If the configuration with adatoms on the same sublattice has lower energy than with adatoms on different sublattices, then domains with broken sublattice symmetry are generated. This can happen if the adatoms may move along the flake, which requires that the activation barrier is smaller than the desorption barrier. This condition is not met for hydrogen adatoms, but it can be valid for other adatoms, for example the halogens.

Turning to the second possibility, there are substrates for graphene which break the sublattice symmetry [46, 130], for example SiC or BN. Such substrates have a hexagonal lattice structure and almost the same lattice constant as graphene. The onsite potentials are different for each sublattice, due to different atoms on the sublattices, see Fig. 1.2. If the graphene lattice is matched with the substrate lattice, then the sublattice symmetry is broken, which leads to a band gap (estimated in Ref. [46] at 53 meV for BN).

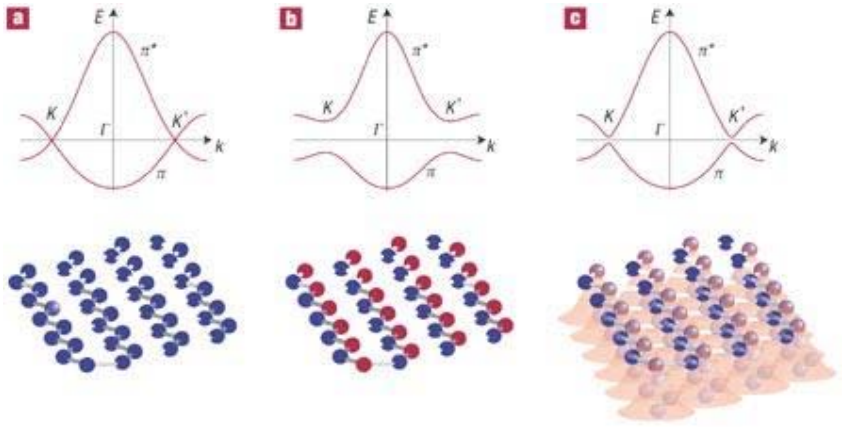

Figure 1.2. Schematic representation of crystal structure and dispersion relation: a) free-standing graphene; b) boron-nitride, BN (with different atoms represented by different colours); c) graphene on BN. As different atoms of the substrate have different potentials, the sublattice symmetry is broken and a gap is opened. From Ref. [89].

1.3 Dirac fermions in superconductors

In conventional superconductors an electron with spin up, momentum $\boldsymbol{k}$ forms a Cooper pair with an electron with spin down, momentum $-\boldsymbol{k}$. This spin-singlet, s-wave pairing is isotropic both with respect to the spin and with respect to the orbital degree of freedom. Superconductors with anisotropic pairing are called unconventional. The high-T_c cuprate superconductors are a notable example, where the Cooper pairs have spin singlet, d-wave symmetry. Spin-triplet, p-wave pairing appears in strontium ruthenate (Sr_2RuO_4). Quasiparticle excitations in these superconductors are Dirac fermions, as we will discuss in this section.

1.3.1 Pairing symmetry

Let us first classify the types of electron pairing, consistent with the requirement of an antisymmetric wave function. The wave function of two electrons consists of a spin part χ and orbital part Δ (also called the pair potential). The full wave function should be antisymmetric with respect to interchange of the two fermions: $\Delta(\boldsymbol{k})\chi_{12} = -\Delta(-\boldsymbol{k})\chi_{21}$, with $\boldsymbol{k}$ the momentum of the relative motion of the electron pair.

The spin state is given in terms of the Pauli matrices

$$\sigma_x = \begin{pmatrix} 0 & 1 \\ 1 & 0 \end{pmatrix}, \ \sigma_y = \begin{pmatrix} 0 & -i \\ i & 0 \end{pmatrix}, \ \sigma_z = \begin{pmatrix} 1 & 0 \\ 0 & -1 \end{pmatrix}. \tag{1.6}$$

The basis states for a single spin are the spinors

$$|\uparrow\rangle = \begin{pmatrix} 1 \\ 0 \end{pmatrix}, \ |\downarrow\rangle = \begin{pmatrix} 0 \\ 1 \end{pmatrix}. \tag{1.7}$$

The basis states for two spins are

$$|\uparrow\uparrow\rangle = \begin{pmatrix} 1 & 0 \\ 0 & 0 \end{pmatrix}, \ |\uparrow\downarrow\rangle = \begin{pmatrix} 0 & 1 \\ 0 & 0 \end{pmatrix}, \ |\downarrow\uparrow\rangle = \begin{pmatrix} 0 & 0 \\ 1 & 0 \end{pmatrix}, \ |\downarrow\downarrow\rangle = \begin{pmatrix} 0 & 0 \\ 0 & 1 \end{pmatrix}. \tag{1.8}$$

The spin-singlet state is given by

$$|\uparrow\downarrow\rangle - |\downarrow\uparrow\rangle = \begin{pmatrix} 0 & 1 \\ -1 & 0 \end{pmatrix} = i\sigma_y, \tag{1.9}$$

which is antisymmetric with respect to interchange of the particles. Hence for spin-singlet superconductivity the Cooper pair wave function is

$$\Psi = \Delta(\boldsymbol{k}) i\sigma_y, \tag{1.10}$$

with $\Delta(-\boldsymbol{k}) = \Delta(\boldsymbol{k})$.

For s-wave pairing the pair potential $\Delta = \Delta_0$ is a constant. The superconducting gap is then isotropic, equal to Δ_0. For d-wave pairing one has an anisotropic pair potential,

$$\Delta(\boldsymbol{k}) = (\Delta_0/k_F^2)(k_x^2 - k_y^2). \tag{1.11}$$

The gap in this case vanishes along the nodal lines $|k_x| = |k_y|$.

Spin-triplet pairing is described by the wave function

$$\Psi = \Delta_{\uparrow\uparrow}(\boldsymbol{k}) \, |\uparrow\uparrow\rangle + \Delta_{\uparrow\downarrow}(\boldsymbol{k})(|\uparrow\downarrow\rangle + |\downarrow\uparrow\rangle) + \Delta_{\downarrow\downarrow}(\boldsymbol{k}) \, |\downarrow\downarrow\rangle. \tag{1.12}$$

An equivalent representation is in terms of the three-dimensional vector $\boldsymbol{d}(\boldsymbol{k})$ and the vector of Pauli matrices $\boldsymbol{\sigma}$,

$$\Psi = i(\boldsymbol{d} \cdot \boldsymbol{\sigma})\sigma_y = \begin{pmatrix} -d_x + id_y & d_z \\ d_z & d_x + id_y \end{pmatrix}. \tag{1.13}$$

For p-wave pairing the function $\boldsymbol{d}(\boldsymbol{k})$ is linear in $\boldsymbol{k}$. In Sr_2RuO_4 it has the form [57]

$$\boldsymbol{d}(\boldsymbol{k}) = (\Delta_0/k_F)(k_x \pm ik_y)\boldsymbol{d}_0. \tag{1.14}$$

This state breaks time-reversal symmetry (by choosing the sign $\pm$). It is called a chiral p-wave state.

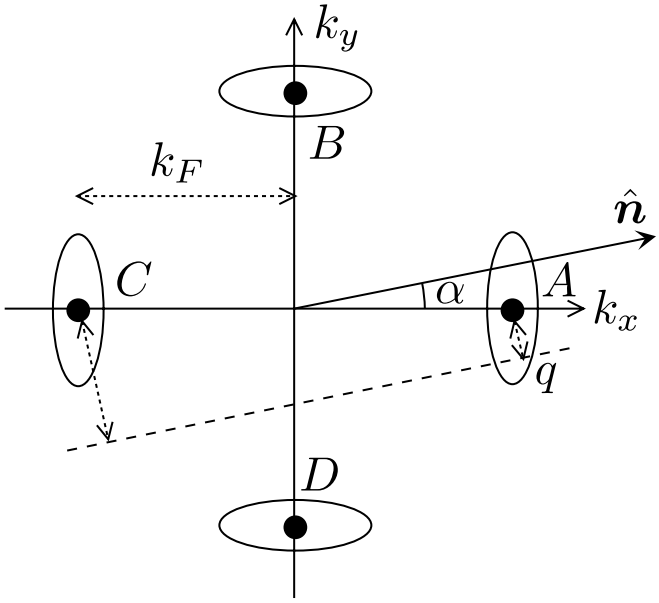

Figure 1.3. Ellipsoidal equal-energy contours of low-energy excitations in the Brillouin zone of superconductor with d_{xy} symmetry. The contours are centered at the four nodal points (solid dots), where the order parameter vanishes on the Fermi surface. From Ref. [9].

1.3.2 Dirac fermions in *d*-wave superconductors

In the vicinity of the nodal lines (where the pair potential (1.11) vanishes) the Hamiltonian for the quasiparticle excitations can be linearized, resulting in a Dirac Hamiltonian, see Fig. 1.3.

To see how this works out, we start from a tight-binding Hamiltonian in second quantization,

$$H = \sum_{ij} (c^\dagger_{i\uparrow}, c_{i\downarrow}) \begin{pmatrix} t_{ij} - \mu\delta_{ij} & \Delta_{ij} \\ \Delta_{ij} & -t_{ij} + \mu\delta_{ij} \end{pmatrix} \begin{pmatrix} c_{j\uparrow} \\ c^\dagger_{j\downarrow} \end{pmatrix}. \tag{1.15}$$

Here $c_{i\sigma}$ is the annihilation operator for an electron with spin σ on site i of a square lattice (lattice constant a), the t_{ij}'s are hopping matrix elements, μ is the Fermi energy, and Δ_{ij} is the d-wave pair potential.

Upon particle-hole transformation $d_\uparrow = c_\uparrow$, $d_\downarrow = c^\dagger_\downarrow$, rotation of operators $(d_\uparrow, d_\downarrow) \equiv d \mapsto \exp(i\pi\sigma_x/4)d$, and Fourier transformation the Hamil-

tonian becomes:

$$H = \sum_k d^\dagger \left[(t(\boldsymbol{k}) - \mu)\sigma_y + \Delta(\boldsymbol{k})\sigma_x \right] d, \tag{1.16}$$

with $t(\boldsymbol{k}) = t_0[\cos(k_x a) + \cos(k_y a)]$ and $\Delta(\boldsymbol{k}) = \Delta_0[\cos(k_x a) - \cos(k_y a)]$.

For a half-filled band, the superconducting gap closes at the Fermi level in four points, namely at $(k_x, k_y) = (\pm\pi/2a, \pm\pi/2a)$. Expansion near these four nodal points, $k_x = \pm\pi/2a + \delta k_x$, $k_y = \pm\pi/2a + \delta k_y$, gives the linear dispersion relation

$$E = \pm a\sqrt{t_0^2(\delta k_x + \delta k_y)^2 + \Delta_0^2(\delta k_x - \delta k_y)^2}. \tag{1.17}$$

The linearized Hamiltonian takes the form, after rotation by $\pi/4 + \pi n/2$, of an anisotropic Dirac Hamiltonian,

$$\mathcal{H} = \hbar v_F \begin{pmatrix} 0 & \delta k_x - i(\Delta_0/t_0)\delta k_y \\ \delta k_x + i(\Delta_0/t_0)\delta k_y & 0 \end{pmatrix}, \tag{1.18}$$

with $v_F = at_0/\hbar$. The anisotropy is typically large, $\Delta_0/t_0 \simeq 0.07$ in the cuprate superconductor $YBa_2Cu_3O_{7-\epsilon}$.

Electrostatic potential fluctuations move the location of the nodal points, thereby shifting the vector $\delta\boldsymbol{k} \mapsto \delta\boldsymbol{k} + \boldsymbol{A}$ by some offset vector $\boldsymbol{A}$. If the potential varies slowly on the scale of $1/a$, different nodal points remain uncoupled and we may fully account for the potential fluctuations by the effect on each node separately. The slowly varying function $\boldsymbol{A}(\boldsymbol{r})$ then enters into the Dirac equation as a fictitious vector potential.

1.3.3 Dirac fermions in chiral *p*-wave superconductors

The chiral p-wave superconductor Sr_2RuO_4 is a two-dimensional layered structure in the $x - y$ plane. The vector $\boldsymbol{d}_0$ in Eq. (1.14) is oriented along the perpendicular z-direction in zero magnetic field, which implies the antiparallel-spin-triplet pairing $|\uparrow\downarrow\rangle + |\downarrow\uparrow\rangle$. In a perpendicular magnetic field, it is energetically more favorable for $\boldsymbol{d}_0$ to lie in the $x - y$ plane, where it can rotate freely. This implies equal-spin pairing, with decoupled pairs $|\uparrow\uparrow\rangle$ and $|\downarrow\downarrow\rangle$.

Chiral p-wave superconductors with equal-spin pairing can be in two topologically distinct phases, distinguished by the sign of the mass term in

the Dirac equation [122]. To see how this arises, we start from the pairing Hamiltonian

$$H = \sum_{\boldsymbol{k}} \left[\xi_k c^\dagger_{\boldsymbol{k}} c_{\boldsymbol{k}} + \tfrac{1}{2}(\Delta^*_{\boldsymbol{k}} c_{-\boldsymbol{k}} c_{\boldsymbol{k}} + \Delta_{\boldsymbol{k}} c^\dagger_{\boldsymbol{k}} c^\dagger_{-\boldsymbol{k}}) \right]. \tag{1.19}$$

The operator $c_{\boldsymbol{k}}$ is the fermionic annihilation operator (wave vector $\boldsymbol{k}$, spin omitted). We denote by $\xi_k = \hbar^2 k^2/2m - \mu$ the single-particle kinetic energy (relative to the Fermi energy μ). The pair potential has the chiral p-wave form

$$\Delta_{\boldsymbol{k}} = (\Delta_0/k_F)(k_x - ik_y), \tag{1.20}$$

where we have chosen a specific chirality.

The Hamiltonian (1.19) is diagonalized, $H = \sum_{\boldsymbol{k}} \alpha^\dagger_{\boldsymbol{k}} \alpha_{\boldsymbol{k}} + \text{constant}$, via a Bogoliubov transformation,

$$\alpha_{\boldsymbol{k}} = u_{\boldsymbol{k}} c_{\boldsymbol{k}} - v_{\boldsymbol{k}} c^\dagger_{-\boldsymbol{k}}, \quad \alpha^\dagger_{\boldsymbol{k}} = u^*_{\boldsymbol{k}} c^\dagger_{\boldsymbol{k}} - v^*_{\boldsymbol{k}} c_{-\boldsymbol{k}}. \tag{1.21}$$

The electron and hole wave amplitudes $u_{\boldsymbol{k}}$ and $v_{\boldsymbol{k}}$ satisfy the Bogoliubov-De Gennes equations,

$$E_k u_{\boldsymbol{k}} = \xi_k u_{\boldsymbol{k}} - \Delta^*_{\boldsymbol{k}} v_{\boldsymbol{k}}, \quad E_k v_{\boldsymbol{k}} = -\xi_k v_{\boldsymbol{k}} - \Delta_{\boldsymbol{k}} u_{\boldsymbol{k}}. \tag{1.22}$$

Upon substitution of Eq. (1.20), we see that the electron-hole wave function $\psi = (u, v)$ is an eigenstate of the Hamiltonian

$$\begin{aligned} H &= \begin{pmatrix} \xi_k & (\Delta_0/k_F)(-k_x - ik_y) \\ (\Delta_0/k_F)(-k_x + ik_y) & -\xi_k \end{pmatrix} \\ &= \xi_k \sigma_z + (\Delta_0/k_F)(-k_x \sigma_x + k_y \sigma_y), \end{aligned} \tag{1.23}$$

which is a Dirac Hamiltonian with a k-dependent mass ξ_k.

At low energies, $k \to 0$ and we may approximate $\xi_k \approx -\mu$. The sign of μ is a topological invariant, in the sense that it cannot change without closing the excitation gap in the system. Superconductors have typically $\mu > 0$, so a negative mass in the Dirac equation. This is the socalled weak-pairing state. (The strong-pairing state with $\mu < 0$ and positive mass can appear in superfluids [122].)

Electrostatic potential fluctuations cause fluctuations in μ and hence in the mass of the Dirac fermions in the chiral p-wave superconductor. This is in contrast to what we saw in the previous subsection for the d-wave superconductor, where electrostatic potential fluctuations appear as a vector potential for the Dirac fermions.

1.4 Majorana fermions

The Bogoliubov-De Gennes equations (1.22) have particle-hole symmetry, such that if $\big(u(\boldsymbol{r}), v(\boldsymbol{r})\big)$ is an eigenstate at energy E then $(v^*(\boldsymbol{r}), u^*(\boldsymbol{r}))$ is an eigenstate at energy $-E$. (We work in real space, with $\boldsymbol{k} = -i\partial/\partial\boldsymbol{r}$.) In terms of the quasiparticle annihilation operator $\alpha(E)$ of an eigenstate at energy E, this symmetry relation reads $\alpha(E) = \alpha^\dagger(-E)$. At zero excitation energy, $\alpha = \alpha^\dagger$, so the excitation is a Majorana fermion (particle equal to antiparticle). Because zero energy is measured relative to the Fermi level, at the center of the excitation gap, such Majorana bound states are midgap states.

Chiral p-wave superconductors can have Majorana bound states, trapped inside the normal core of a magnetic vortex [122]. A vortex in a conventional s-wave superconductor also traps states inside the gap, but these are displaced from $E = 0$ by the energy Δ_0^2/E_F of zero-point motion, so they are not midgap states.

Because the Majorana bound states are all at the same energy, tunneling from one vortex to the other is a resonant process. For a sufficient density of vortices the wave functions extend throughout the system, rather than being localized inside the vortices. The superconductor is then a *thermal metal* rather than a *thermal insulator*. The adjective "thermal" is added because the excitations in a superconductor are charge neutral, so they transport thermal energy but no electrical charge.

One of the findings of our thesis, is that Majorana fermions can be created in chiral p-wave superconductors by a purely electrostatic mechanism, without requiring a magnetic vortex. A change in the sign of the mass $\mu(\boldsymbol{r})$ along a line defect creates Majorana bound states at the two end points.

One might wonder whether this mechanism would be operative also in graphene, if a staggered potential would create a similar line defect. The answer is negative, as we will show later in the thesis, for the following reason: A sign change in the mass will only produce a Majorana bound state if the mass has a nonzero k^2 term. This is the case for the mass term $\xi_k = \hbar^2k^2/2m - \mu$ in the chiral p-wave superconductor Hamiltonian (1.23), but not for the graphene Hamiltonian (1.5).

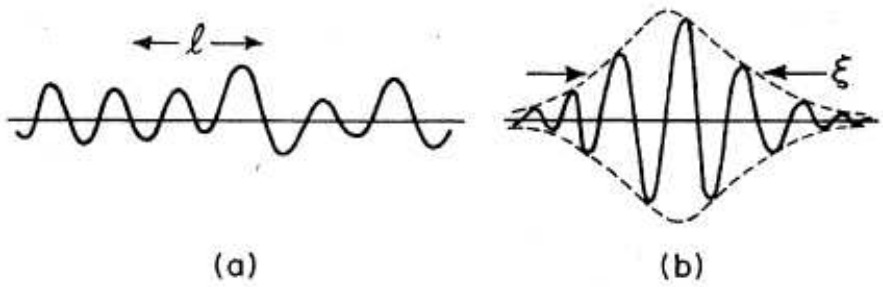

Figure 1.4. Typical wavefunction for a) delocalized and b) localized states, with the mean free path l and the localization length ξ indicated. From Ref. [69].

1.5 Scaling theory of localization

We will study the phase transition from a thermal metal to a thermal insulator within the context of the scaling theory of localization [69]. A summary of that theory is presented here, for the *electrical* metal-insulator transition. We will see later in the thesis what qualitative differences appear for the *thermal* metal-insulator transition.

1.5.1 Single-parameter scaling

The single-parameter scaling hypothesis [1] states that the conductance of a d-dimensional conductor of linear size L depends on the microscopic parameters of the system through a single length scale ξ, called the localization length in the insulator and the correlation length (or mean free path) in the metal. (See Fig. 1.4.) In units of e^2/h, the dimensionless conductance $g = f(L/\xi)$ is therefore a function of the ratio L/ξ. The function f may depend on the dimensionality d and on fundamental symmetries of the system (for example, the presence or absence of time-reversal symmetry), but it may not depend on microscopic parameters (such as the mean free path l).

In a metal, Ohm's law implies that $g \propto L^{d-2}$ depends as a power law on L. In an insulator, the conductance decays exponentially, $g \propto e^{-L/\xi}$. In order to interpolate between these two limits, it is convenient to work with the logarithmic derivative $\beta = d\ln g/d\ln L$. According to single-parameter scaling, $\beta(g)$ can be expressed as a function of g itself. The two limits are

$$\beta(g) = \ln(g/g_c), \tag{1.24}$$

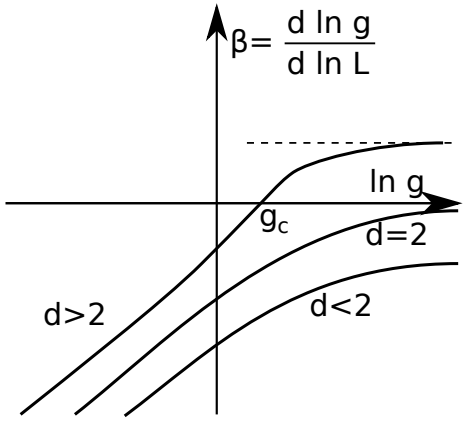

Figure 1.5. Schematic β-function for the electrical metal-insulator transition in different dimensions, in the presence of time-reversal symmetry.

in an insulator and

$$\beta(g) = d - 2 + \delta(g), \tag{1.25}$$

in a metal. The first quantum correction to Ohm's law, $\delta(g) = a/g$ with $a < 0$, can be calculated by perturbation theory.

The β-function for the electrical metal-insulator transition is shown in Fig. 1.5, for different dimensions and in the presence of time-reversal symmetry [1]. (We also assumed that spin is a conserved quantity.) For $d = 3$ there is a critical point g_c where the β-function equals zero, meaning that the conductance of the system is scale invariant (independent of L). This fixed point signals the metal-insulator transition. It is an unstable fixed point, since on one side the system scales to a metal and on the other side to an insulator.

1.5.2 Critical exponent

The critical exponent ν quantifies how unstable the fixed point is. Let us assume that $1/\nu$ is the slope of the β-function at g_c, with $\beta(g_c) = 0$. Integration of $\beta(g) = d \ln g / d \ln L$ from the metallic side gives

$$\ln \frac{g}{g_c} = \left(\frac{L}{\lambda}\right)^{1/\nu} \ln \frac{g_\lambda}{g_c}, \tag{1.26}$$

where (λ, g_λ) is some point on the scaling curve in the vicinity of g_c with $\beta(g_\lambda) > 0$. Integration from the insulating side gives

$$g \sim g_c \exp(-BL\delta g^\nu/\lambda), \tag{1.27}$$

with B a constant and $\delta g = g_c - g$.

In the metallic regime the point $\beta(g_\xi) = 1$ is determined by the correlation length

$$\xi = \lambda \left(\frac{1}{\nu} \ln \frac{g_\lambda}{g_c} \right)^{-\nu}. \tag{1.28}$$

The correlation length (or mean free path) is the minimal length when Ohm's law is applicable. In the insulating regime the localization length ξ following from the definition $g = g_c \exp(-L/\xi)$ is

$$\xi = \frac{\lambda}{B\delta g^\nu}. \tag{1.29}$$

1.5.3 Finite-size scaling

The hypothesis of single-parameter scaling holds in the large-L limit. For finite L corrections appear, which one needs to take into account in order to reliably determine the critical conductance and critical exponent [65].

Let us consider a finite system which is characterized by several parameters $\{x_i\}$, for example, mean free path, electron density, etc. We consider the L dependence of a variable F which becomes scale invariant at the metal-insulator transition. Typically, F is the conductance, but other quantities can be useful in computer simulations.

According to the scaling hypothesis, the function $F_L = F(\{x_i\}, L)$ can be written in the form

$$F_L = F(\chi L^{1/\nu}, \phi_1 L^{y_1}, \phi_2 L^{y_2}, \dots), \tag{1.30}$$

with $\nu > 0$ the critical exponent and all $y_i < 0$. So in the large-L limit the terms with y_i die out and the parameters ϕ_i become irrelevant.

Near the phase transition χ as a function of a control parameter x can be expanded as

$$\chi = \chi_1(x - x_c) + \chi_2(x - x_c)^2 + \dots. \tag{1.31}$$

The vanishing of χ at the phase transition x_c implies that F becomes scale invariant in the large-L limit.

1.5.4 Symmetry classes

The electrical metal-insulator transition discussed so far, with the scaling function shown in Fig. 1.5, holds for electrons described by the Schrödinger equation, in the presence of time-reversal symmetry and spin-rotation symmetry. This symmetry class is denoted as AI. (The name comes from the mathematics literature.)

The thermal metal-insulator transition in a chiral p-wave superconductor is in a different universality class: The excitations are described by a Dirac equation, with time-reversal symmetry and spin-rotation symmetry both broken, but with an additional symmetry, which is particle-hole symmetry. This symmetry class is denoted as BD or D (depending on whether or not there is vortex disorder).

There are in total 10 symmetry classes in the theory of localization, depending on the presence or absence of time-reversal symmetry, spin-rotation symmetry, particle-hole symmetry, and sublattice (or chiral) symmetry [36]. In this thesis we will be concerned mainly with class BD/D. One other symmetry class will appear for d-wave superconductors, which is class AIII (chiral symmetry without time-reversal symmetry).

The β-function is different in each symmetry class. In particular, in class BD there can be a metal-insulator transition already in two dimensions, which is not possible in class AI. In class AIII there is no insulating phase at all.

1.6 Dirac fermions on a lattice

Our numerical studies of localization of Dirac fermions are based on a transfer matrix discretization of the Dirac equation, either in real space or in momentum space. We will introduce the different discretization schemes in this section.

An alternative approach, which we have not taken, is based on models which are in the same universality class D as the Dirac equation, but which do not approach the Dirac equation in the continuum limit [36]. These generic class D models are variations of the Chalker-Coddington network model [24]. Our preference for a discretization of the Dirac equation is that we can stay closer to a specific physical system (graphene or a chiral p-wave superconductor) and have direct access to a physical observable (electrical or thermal conductance).

One obvious requirement of any discretization is that it should preserve Hermiticity of the Hamiltonian. In a transfer matrix formulation this requirement appears as the requirement of current conservation. Two further requirements are special for Dirac fermions: we should avoid fermion doubling and preserve symplectic symmetry.

1.6.1 Avoid fermion doubling

Dirac fermions on a lattice were introduced in the context of QCD [100]. It was discovered in that context that a straightforward discretization of the Dirac equation introduces a spurious second Dirac point in the spectrum. This is the notorious fermion doubling problem.

A simple one-dimensional discretization shows the nature of the problem. Let us assume that there is a lattice with lattice spacing a and number of lattice points N. We want to discretize on it the equation

$$-i\partial_x \psi(x) = \lambda \psi(x). \tag{1.32}$$

Notice that the spectrum of the continuous equation is $\lambda(k) = k$. A naive discretization of the derivative,

$$\partial_x \psi(x) \longrightarrow \frac{\psi(x+a) - \psi(x)}{a}, \tag{1.33}$$

does not produce a Hermitian operator $-i\partial_x \psi$ on the lattice. There is a simple way to make it Hermitian, namely by symmetrization,

$$\partial_x \psi(x) \longrightarrow \frac{\psi(x+a) - \psi(x-a)}{2a}. \tag{1.34}$$

Fourier transformation, $\psi(x) = \sum_p \exp(ipx)\psi(p)$ with $p = 2\pi m/aN$, $m = 1, 2, \ldots, N$, gives the spectrum

$$\lambda(p) = \sin(pa)/a. \tag{1.35}$$

Near $p = 0$ we recover the linear spectrum of the continuous equation (1.32). The derivative $\partial\lambda/\partial p > 0$ near $p = 0$, so the particles are right-moving. But in the vicinity of $p = \pi/a$ there is one more zero in the dispersion relation (see Fig. 1.6), with $\partial\lambda/\partial p < 0$, so a second species of left-moving particles has appeared — which is not present in the continuous equation.

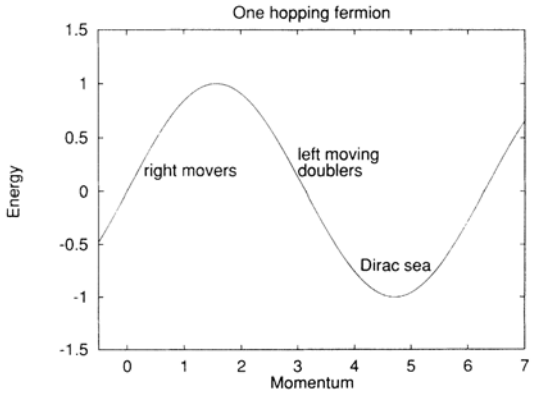

Figure 1.6. Illustration of fermion doubling in one dimension. From Ref. [30].

The Nielsen-Ninomiya "no-go" theorem [85] states that fermion doubling (with an equal number of left-movers and right-movers) is unavoidable for a discretization scheme which is Hermitian, local, and translationally invariant. The reason is that periodicity in lattice momentum p gives an equal number of zeros with positive and negative slopes.

If some of the conditions of the theorem are not met, then it is possible to avoid fermion doubling. The transfer matrix discretization schemes that we will use in this thesis (in real space and momentum space) are nonlocal. This complicates the algorithm, but it has the great advantage that it preserves the symplectic symmetry of the Dirac equation. An alternative approach is to make one of the two fermion species massive (Wilson fermion). This produces an easier algorithm, but breaks symplectic symmetry.

1.6.2 Conserve current and preserve symmetries

The transfer matrix of the Dirac Hamiltonian

$$H = v_F(p_x\sigma_x + p_y\sigma_y) + m(\boldsymbol{r})v_F^2\sigma_z + u(\boldsymbol{r}), \tag{1.36}$$

can be calculated by integrating the eigenvalue equation $H\Psi = E\Psi$ in the form

$$\partial_x\Psi = \Big[-ip_y\sigma_z/\hbar - iU(\boldsymbol{r})\sigma_x - M(\boldsymbol{r})\sigma_y\Big]\Psi, \tag{1.37}$$

with $U = (u - E)/\hbar v_F$ and $M = mv_F/\hbar$.

For this integration we discretize a rectangular strip on an $M \times N$ lattice, with M columns in the x-direction and N rows in the y-direction. We take periodic boundary conditions in the y-direction. The values $\Psi_{m,n} = \Psi(x_m, y_n)$ of the wave function at a lattice point are collected into a set vectors $\mathbf{\Psi}_m$. The transfer matrix $\mathcal{T}_m$ of slice m is defined by

$$\mathbf{\Psi}_{m+1} = \mathcal{T}_m \mathbf{\Psi}_m. \tag{1.38}$$

The transfer matrix $\mathcal{T}$ through the entire strip is then the product of the $\mathcal{T}_m$'s.

Current conservation, with current operator $\mathcal{J}_x$ along the strip, requires that

$$\langle \Psi_1 | \mathcal{J}_x | \Psi_1 \rangle = \langle \Psi_M | \mathcal{J}_x | \Psi_M \rangle \Rightarrow \mathcal{J}_x = \mathcal{T}^\dagger \mathcal{J}_x \mathcal{T}. \tag{1.39}$$

Preservation of symplectic symmetry imposes an additional condition on the transfer matrix. Symplectic symmetry is the invariance of the Hamiltonian under inversion of momentum and spin. It is broken by a mass term, so this is not an important requirement if one studies, for example, gapped graphene.

For massless Dirac fermions in a scalar potential u the Hamiltonian $H = v_F \boldsymbol{p} \cdot \boldsymbol{\sigma} + u(\boldsymbol{r})$ is invariant under inversion $\boldsymbol{p} \mapsto -\boldsymbol{p}$, $\boldsymbol{\sigma} \mapsto -\boldsymbol{\sigma}$. This symmetry can equivalently be written as $H = \sigma_y H^* \sigma_y$, where the complex conjugation is carried out in the real space basis (when $\boldsymbol{p} = -i\hbar\partial/\partial\boldsymbol{r}$). The condition on the transfer matrix is

$$\mathcal{T} = \sigma_y \mathcal{T}^* \sigma_y. \tag{1.40}$$

The Dirac Hamiltonian $H = v_F(p_x\sigma_x + p_y\sigma_y) + mv_F^2\sigma_z$ with a mass term, but without the scalar potential, has no symplectic symmetry but instead has particle-hole symmetry: $\sigma_x H^* \sigma_x = -H$. This is the relevant Hamiltonian for a chiral p-wave superconductor. The corresponding symmetry relation for the transfer matrix is

$$\mathcal{T}(E) = \sigma_x \mathcal{T}^*(-E)\sigma_x. \tag{1.41}$$

1.6.3 Real space discretization

The transfer matrix resulting from the real space discretization of Eq. (1.37) was calculated in Ref. [119], using the staggered fermion approach from QCD [100]. We summarize this method.

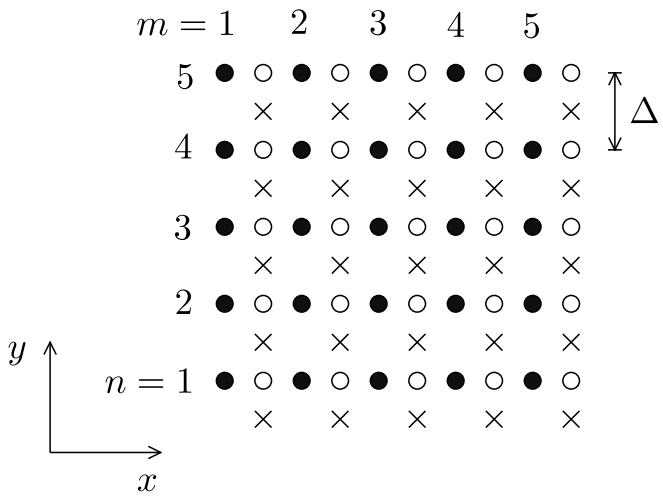

Figure 1.7. Square lattice (filled circles) on which the wave function Ψ is discretized as $\Psi_{m,n}$. The finite differences are evaluated at the displaced points indicated by crosses. The Dirac equation (1.37) is applied at the empty circles, by taking the mean of the contributions from the two adjacent crosses. From Ref. [119].

Discretized operators are defined at points of the displaced lattice shown in Fig. 1.7. The differential operators are discretized by

$$\partial_x \Psi \to \frac{1}{2a}(\Psi_{m+1,n} + \Psi_{m+1,n+1} - \Psi_{m,n} - \Psi_{m,n+1}), \tag{1.42}$$

$$\partial_y \Psi \to \frac{1}{2a}(\Psi_{m,n+1} + \Psi_{m+1,n+1} - \Psi_{m,n} - \Psi_{m+1,n}). \tag{1.43}$$

The potential and mass terms are replaced by averages over adjacent lattice points,

$$M\sigma_z\Psi \to \tfrac{1}{4}M_{m,n}\sigma_z\big(\Psi_{m+1,n} + \Psi_{m+1,n+1} + \Psi_{m,n} + \Psi_{m,n+1}\big), \tag{1.44}$$

$$U\Psi \to \tfrac{1}{4}U_{m,n}\big(\Psi_{m+1,n} + \Psi_{m+1,n+1} + \Psi_{m,n} + \Psi_{m,n+1}\big), \tag{1.45}$$

with $M_{m,n} = M(x_m + a/2, y_n + a/2)$ and $U_{m,n} = U(x_m + a/2, y_n + a/2)$.

The zero-energy Dirac equation $H\Psi = 0$ is applied at the points $(x_m + a/2, y_n)$ by averaging the terms at the two adjacent points $(x_m + a/2, y_n \pm a/2)$. The resulting finite difference equation can be written in a compact form with the help of the $N_y \times N_y$ tridiagonal matrices $\mathcal{J}$, $\mathcal{K}$, $\mathcal{M}^{(m)}$,

defined by the following nonzero elements:

$$\mathcal{J}_{n,n} = 1, \;\; \mathcal{J}_{n,n+1} = \mathcal{J}_{n,n-1} = \tfrac{1}{2}, \tag{1.46}$$

$$\mathcal{K}_{n,n+1} = \tfrac{1}{2}, \;\; \mathcal{K}_{n,n-1} = -\tfrac{1}{2}, \tag{1.47}$$

$$\mathcal{M}^{(m)}_{n,n} = \tfrac{1}{2}(M_{m,n} + M_{m,n-1}), \;\; \mathcal{M}^{(m)}_{n,n+1} = \tfrac{1}{2}M_{m,n}, \mathcal{M}^{(m)}_{n,n-1} = \tfrac{1}{2}M_{m,n-1}, \tag{1.48}$$

$$\mathcal{V}^{(m)}_{n,n} = \tfrac{1}{2}(U_{m,n} + U_{m,n-1}), \;\; \mathcal{U}^{(m)}_{n,n+1} = \tfrac{1}{2}U_{m,n}, \mathcal{U}^{(m)}_{n,n-1} = \tfrac{1}{2}U_{m,n-1}. \tag{1.49}$$

In accordance with the periodic boundary conditions in the transverse direction, the indices $n \pm 1$ should be evaluated modulo N_y.

The discretized Dirac equation is expressed in terms of the matrices (1.46)–(1.49) by

$$\frac{1}{2a}\mathcal{J}(\mathbf{\Psi}_{m+1} - \mathbf{\Psi}_m) = \left(-\frac{i}{2a}\sigma_z\mathcal{K} - \frac{1}{4}v^2\sigma_y\mathcal{M}^{(m)} - \frac{i}{4}v^2\sigma_x\mathcal{V}^{(m)}\right)(\mathbf{\Psi}_m + \mathbf{\Psi}_{m+1}). \tag{1.50}$$

Rearranging Eq. (1.50) we arrive at Eq. (1.38) with the transfer matrix

$$\mathcal{T}_m = \left(\mathcal{J} + i\sigma_z\mathcal{K} + \tfrac{1}{2}v^2a\sigma_y\mathcal{M}^{(m)}\right)^{-1}\left(\mathcal{J} - i\sigma_z\mathcal{K} - \tfrac{1}{2}v^2a\sigma_y\mathcal{M}^{(m)}\right). \tag{1.51}$$

For a uniform mass $M_{mn} = M$ and uniform potential $U_{mn} = \epsilon$, we may calculate the eigenvalues e^{ik_xa} of $\mathcal{T}_m$ analytically. This gives the dispersion relation

$$\tan^2(k_xa/2) + \tan^2(k_ya/2) + (Mav_F/2\hbar)^2 = (\epsilon/2)^2, \tag{1.52}$$

with $k_y = 2\pi l/N_y$, $l = 1, 2, \ldots N_y$. The zero of the dispersion relation at $k_x = \pi/a$, responsible for the fermion doubling, is replaced by a pole. The nonlocality of the staggered discretization scheme works around the no-go theorem.

This discretization scheme conserves the current operator

$$J_x = \tfrac{1}{2}v\sigma_x\mathcal{J}. \tag{1.53}$$

It preserves symplectic symmetry for $M = 0$ and obeys particle-hole symmetry for $U = 0$.

1.6.4 Momentum space discretization

An alternative momentum space discretization was developed in Ref. [11]. The differential equation (1.37) is integrated in the x-direction by a straightforward discretization in real space, but in the y-direction the discretization of p_y is carried out in momentum space. The combination of these two discretizations produces a nonlocal transfer matrix, which works around the no-go theorem for fermion doubling, preserving current and all symmetries.

The algorithm is simplified by carrying out the two discretizations in separate steps. One step accounts for scattering $\mathcal{S}$ by disorder in a single slice, another step accounts for free propagation $\mathcal{P}$ from one slice to the next:

$$\mathcal{S}_m = \exp(-iU_m\sigma_x - M_m\sigma_y), \tag{1.54}$$

$$\mathcal{P} = \exp(-ip_y\sigma_z a/\hbar). \tag{1.55}$$

Here U_m and M_m are diagonal matrices containing the potential and mass at column m on the diagonal.

The transfer matrix is the product

$$\mathcal{T} = \mathcal{P}\mathcal{U}\mathcal{S}_M\mathcal{U}^\dagger\mathcal{P}\mathcal{U}\cdots\mathcal{S}_2\mathcal{U}^\dagger\mathcal{P}\mathcal{U}\mathcal{S}_1\mathcal{U}^\dagger\mathcal{P}, \tag{1.56}$$

with $\mathcal{U}$ the matrix that Fourier transforms from real space to momentum space. The size of this matrix is made finite by truncating the transverse momentum p_y at some large value.

1.7 This thesis

We summarize the contents of the following chapters.

1.7.1 Chapter 2

This chapter is a numerical study of quasiparticle localization in symmetry class *BD* (realized, for example, in chiral p-wave superconductors), by means of a staggered-fermion lattice model for two-dimensional Dirac fermions with a random mass. For sufficiently weak disorder, the system size dependence of the average (thermal) conductivity σ is well described by an effective mass $M_{\rm eff}$, dependent on the first two moments of the random mass $M(\boldsymbol{r})$. The effective mass vanishes linearly when the average

mass $\bar{M} \to 0$, reproducing the known insulator-insulator phase boundary with a scale invariant dimensionless conductivity $\sigma_c = 1/\pi$ and critical exponent $\nu = 1$. For strong disorder a transition to a metallic phase appears, with larger σ_c but the same ν. The intersection of the metal-insulator and insulator-insulator phase boundaries is identified as a *repulsive* tricritical point.

1.7.2 Chapter 3

In this chapter we look at quasiparticle localization in symmetry class *D*. It is different from class *BD* by absence of the bound states at zero energy. The system is modeled by staggered fermions in momentum space and uses convergence in momentum space to realize a smooth potential landscape in real space. Graphene with a random gap in a known realization of such system. It is known that fluctuations in the electrostatic potential allow for metallic conduction (nonzero conductivity in the limit of an infinite system) if the carriers form a single species of massless two-dimensional Dirac fermions. A nonzero uniform mass $\bar{M}$ opens up an excitation gap, localizing all states at the Dirac point of charge neutrality. Here we investigate numerically whether fluctuations $\delta M \gg \bar{M} \neq 0$ in the mass can have a similar effect as potential fluctuations, allowing for metallic conduction at the Dirac point. Our negative conclusion confirms earlier expectations, but does not support the recently predicted metallic phase in a random-gap model of graphene [131].

1.7.3 Chapter 4

Vortices in two-dimensional superconductors with broken time-reversal and spin-rotation symmetry can bind states at zero excitation energy. These socalled Majorana bound states transform a thermal insulator into a thermal metal and may be used to encode topologically protected qubits. We identify an alternative mechanism for the formation of Majorana bound states, akin to the way in which Shockley states are formed on metal surfaces: *An electrostatic line defect can have a pair of Majorana bound states at the end points.* The Shockley mechanism explains the appearance of a thermal metal in vortex-free lattice models of chiral p-wave superconductors and (unlike the vortex mechanism) is also operative in the topologically trivial phase.

1.7.4 Chapter 5

The bulk microwave conductivity of a dirty d-wave superconductor is known to depend sensitively on the range of the disorder potential: long-range scattering enhances the conductivity, while short-range scattering has no effect. In this chapter we show that the three-terminal electrical conductance of a normal-metal–d-wave superconductor–normal-metal junction has a dual behavior: short-range scattering suppresses the conductance, while long-range scattering has no effect.

1.7.5 Chapter 6

In this chapter we investigate nanomechanical properties, namely the conductivity of a clean graphene sheet, deformed by a gate electrode. The effect of the deformation on the conductivity is twofold: The lattice distortion can be represented as a pseudovector potential in the Dirac equation, whereas the gate causes a inhomogeneous density redistribution. We use elasticity theory to find the profile of the graphene sheet and then evaluate the conductivity by means of the transfer matrix approach. We find that the two effects provide qualitatively different contributions to the conductivity. For small deformations and not too high residual stress the correction due to the charge redistribution dominates and leads to the enhancement of the conductivity. For stronger deformations, the effect of the lattice distortion becomes more important and eventually leads to the suppression of the conductivity. We consider homogeneous as well as local deformation. We also suggest that the effect of the charge redistribution can be best measured in a setup containing two gates, one fixing the overall charge density and another one deforming graphene locally.

Chapter 2

Effective mass and tricritical point for lattice fermions localized by a random mass

2.1 Introduction

Superconductors with neither time-reversal symmetry nor spin-rotation symmetry (for example, having chiral p-wave pairing) still retain one fundamental symmetry: the charge-conjugation (or particle-hole) symmetry of the quasiparticle excitations. Because of this symmetry, quasiparticle localization in a disordered chiral p-wave superconductor is in a different universality class than in a normal metal [36]. The difference is particularly interesting in two dimensions, when the quantum Hall effect governs the transport properties. The electrical quantum Hall effect in a normal metal has the thermal quantum Hall effect as a superconducting analogue [97, 109, 121], with different scaling properties because of the particle-hole symmetry.

The thermal quantum Hall transition is analogous to the electrical quantum Hall transition at the center of a Landau level, but the scaling of the thermal conductivity σ near the phase boundary is different from the scaling of the electrical conductivity because of the particle-hole symmetry. A further difference between these two problems appear if the superconducting order parameter contains vortices [97, 17, 98]. A vortex contains a Majorana bound state at zero excitation energy, in the weak-pairing regime [124, 47]. A sufficiently large density of Majorana bound states

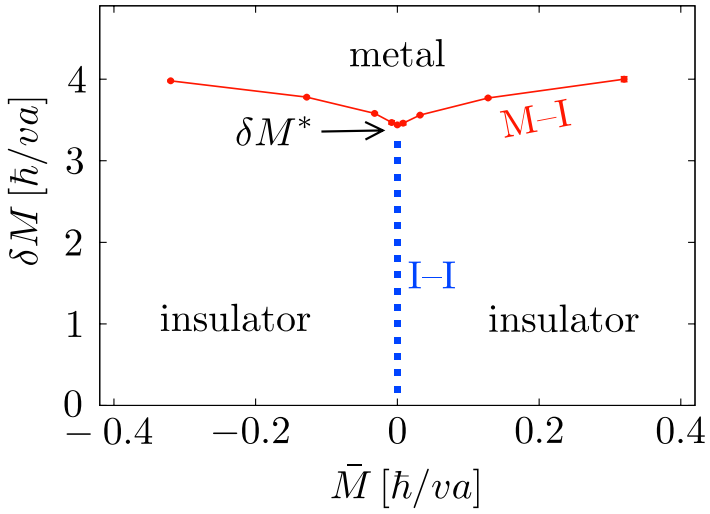

Figure 2.1. Phase diagram in symmetry class *BD*, calculated numerically from the lattice model of staggered fermions described in Sec. 2.3. (A qualitatively similar phase diagram was calculated for a different model [28] in Refs. [23] and [55].) The thermal conductivity decays exponentially $\propto e^{-L/\xi}$ in the localized phase and increases $\propto \ln L$ in the metallic phase. The thermal conductivity is scale invariant on the metal-insulator (M–I) phase boundary (red solid line), as well as on the insulator-insulator (I–I) phase boundary (blue dashed line). The M–I and I–I phase boundaries meet at the tricritical point δM^*.

allows for extended states at the Fermi level, with a thermal conductivity increasing $\propto \ln L$ with increasing system size L [109]. This socalled thermal metal has no counterpart in the electronic quantum Hall effect.

The Bogoliubov-De Gennes Hamiltonian of a disordered chiral p-wave superconductor can be approximated at low energies by a Dirac Hamiltonian with a random mass (see Sec. 2.2). For that reason, it is convenient to parameterize the phase diagram in terms of the average mass $\bar{M}$ and the fluctuation strength δM. As indicated in Fig. 2.1, there are two types of phase transitions [23, 55], a metal-insulator (M–I) transition upon decreasing δM at constant $\bar{M}$ and an insulator-insulator (I–I) transition upon decreasing $\bar{M}$ through zero at constant (not too large) δM. The I–I transition separates phases with a different value of the thermal Hall conductance, while the M–I transition separates the thermal metal from the thermal insulator. Only the I–I transition remains if there are no vortices, or more generally, if there are no Majorana bound states [97, 17, 98].

In the nomenclature of Ref. [17], the symmetry class is called *BD* with Majorana bound states and *D* without.

The *primary purpose* of this chapter is to investigate, by numerical simulation, to what extent the scale dependence of localization by a random mass can be described in terms of an effective non-fluctuating mass: $\sigma(L, \bar{M}, \delta M) = \sigma(L, M_{\rm eff}, 0)$, for some function $M_{\rm eff}(\bar{M}, \delta M)$. Because there is no other length scale in the problem at zero energy, $\sigma(L, M_{\rm eff}, 0)$ can only depend on L and $M_{\rm eff}$ through the dimensionless combination $LM_{\rm eff}v/\hbar \equiv L/\xi$. The effective-mass hypothesis thus implies one-parameter scaling: $\sigma(L, \bar{M}, \delta M) = \sigma_0(L/\xi)$. Two further implications concern the critical conductivity σ_c (which is the scale invariant value of σ on the phase boundary $\bar{M} = 0$) and the critical exponent ν (governing the divergence of the localization length $\xi \propto \bar{M}^{-\nu}$).

Both σ_c and ν follow directly from the effective mass hypothesis. By construction, the scaling function σ_0 is the conductivity of ballistic massless Dirac fermions, which has been calculated in the context of graphene. For a system with dimensions $L \times W$, and periodic boundary conditions in the transverse direction, it is given by [58, 118]

$$\begin{aligned}\sigma_0(L/\xi) &= G_0 \frac{L}{W} \sum_{n=-\infty}^{\infty} \cosh^{-2} \sqrt{(2\pi n L/W)^2 + (L/\xi)^2} \\ &\xrightarrow{W \gg L} G_0 \frac{1}{\pi} \int_0^{\infty} dq \, \cosh^{-2} \sqrt{q^2 + (L/\xi)^2}. \end{aligned} \tag{2.1}$$

A scale invariant conductivity

$$\lim_{\xi \to \infty} \sigma_0(L/\xi) \equiv \sigma_c = G_0 \frac{L}{W} \sum_{n=-\infty}^{\infty} \cosh^{-2}(2\pi n L/W) \tag{2.2}$$

is reached for vanishing effective mass. In the limit of a large aspect ratio $W/L \gg 1$ we recover the known value $\sigma_c = G_0/\pi$ of the critical conductivity for a random mass with zero average [75]. The critical exponent $\nu = 1$ follows by comparing the expansion of the conductivity

$$\sigma(L, \bar{M}, \delta M) = \sigma_c + [L^{1/\nu} \bar{M} f(\delta M)]^2 + \mathcal{O}(\bar{M})^4 \tag{2.3}$$

in (even) powers of $\bar{M}$ with the expansion of the scaling function (2.1) in powers of L. This value for ν is aspect-ratio independent and agrees with the known result for the I–I transition [36].

The description in terms of an effective mass breaks down for strong disorder. We find that the scaling function at the M–I transition differs appreciably from σ_0, with an aspect-ratio independent critical conductivity $\sigma_c \approx 0.4\,G_0$. The critical exponent remains close to or equal to $\nu = 1$ (in disagreement with earlier numerical simulations [55]).

The *secondary purpose* of this chapter is to establish the nature of the tricritical point δM^* at which the two insulating phases and the metallic phase meet. The existence of such a fixed point of the scaling flow is expected on the basis of general arguments [17], but whether it is a repulsive or attractive fixed point has been a matter of debate. From the scale dependence of σ near this tricritical point, we conclude that it is a *repulsive* fixed point (in the sense that σ scales with increasing L to larger values for $\delta M > \delta M^*$ and to smaller values for $\delta M < \delta M^*$). An *attractive* tricritical point had been suggested as a possible scenario [80, 56], in combination with a repulsive critical point at some $\delta M^{**} < \delta M^*$. Our numerics does not support this scenario.

The outline of this chapter is as follows. In the next two Sections we introduce the Dirac Hamiltonian for chiral p-wave superconductors and the lattice fermion model that we use to simulate quasiparticle localization in symmetry class *BD*. We only give a brief description, referring to the Section 1.6.2 and Ref. [119] for a more detailed presentation of the model. The scaling of the thermal conductivity and the localization length near the insulator-insulator and metal-insulator transitions are considered separately in Secs. 2.4 and 2.5, respectively. The tricritical point, at which the two phase boundaries meet, is studied in Sec. 2.6. We conclude in Sec. 2.7.

2.2 Chiral p-wave superconductors

The quasiparticles in a superconductor have electron and hole components ψ_e, ψ_h that are eigenstates, at excitation energy ε, of the Bogoliubov-De Gennes equation

$$\begin{pmatrix} H_0 - E_F & \Delta \\ \Delta^\dagger & -H_0^* + E_F \end{pmatrix} \begin{pmatrix} \psi_e \\ \psi_h \end{pmatrix} = \varepsilon \begin{pmatrix} \psi_e \\ \psi_h \end{pmatrix}. \tag{2.4}$$

In a chiral p-wave superconductor the order parameter $\Delta = \frac{1}{2}\{\chi(\boldsymbol{r}), p_x - ip_y\}$ depends linearly on the momentum $\boldsymbol{p} = -i\hbar\partial/\partial\boldsymbol{r}$, so the quadratic

terms in the single-particle Hamiltonian $H_0 = p^2/2m + U(\boldsymbol{r})$ may be neglected near $p = 0$.

For a uniform order parameter $\chi(\boldsymbol{r}) = \chi_0$, the quasiparticles are eigenstates of the Dirac Hamiltonian

$$H_{\text{Dirac}} = v(p_x\sigma_x + p_y\sigma_y) + v^2 M(\boldsymbol{r})\sigma_z, \tag{2.5}$$

with velocity $v = \chi_0$ and mass $M = (U - E_F)/\chi_0^2$ (distinct from the electron mass m). The Pauli matrices are

$$\sigma_x = \begin{pmatrix} 0 & 1 \\ 1 & 0 \end{pmatrix}, \quad \sigma_y = \begin{pmatrix} 0 & -i \\ i & 0 \end{pmatrix}, \quad \sigma_z = \begin{pmatrix} 1 & 0 \\ 0 & -1 \end{pmatrix}. \tag{2.6}$$

The particle-hole symmetry for the Dirac Hamiltonian is expressed by

$$\sigma_x H^*_{\text{Dirac}} \sigma_x = -H_{\text{Dirac}}. \tag{2.7}$$

Randomness in the electrostatic potential $U(\boldsymbol{r})$ translates into randomness in the mass $M(\boldsymbol{r}) = \bar{M} + \delta M(\boldsymbol{r})$ of the Dirac fermions. The sign of the average mass $\bar{M}$ determines the thermal Hall conductance [97, 109, 121], which is zero for $\bar{M} > 0$ (strong pairing regime) and quantized at $G_0 = \pi^2 k_B^2 T/6h$ for $\bar{M} < 0$ (weak pairing regime).

The Dirac Hamiltonian (2.5) provides a generic low-energy description of the various realizations of chiral p-wave superconductors proposed in the literature: strontium ruthenate [57], superfluids of fermionic cold atoms [116, 105], and ferromagnet-semiconductor-superconductor heterostructures [106, 68, 4]. What these diverse systems have in common, is that they have superconducting order with neither time-reversal nor spin-rotation symmetry. Each of these systems is expected to exhibit the thermal quantum Hall effect, described by the phase diagram studied in this work.

2.3 Staggered fermion model

Earlier numerical investigations [23, 80, 55, 56] of the class *BD* phase diagram were based on the Cho-Fisher network model [28]. Here we use a staggered fermion model in the same symmetry class, originally developed in the context of lattice gauge theory [113, 14] and recently adapted to the study of transport properties in graphene [119]. An attractive feature of the lattice model is that, by construction, it reduces to the Dirac Hamiltonian on length scales large compared to the lattice constant a.

The model is defined on a square lattice in a strip geometry, extending in the longitudinal direction from $x = 0$ to $x = L = N_x a$ and in the transverse direction from $y = 0$ to $y = W = N_y a$. We use periodic boundary conditions in the transverse direction. The transfer matrix $\mathcal{T}$ from $x = 0$ to $x = L$ is derived in Ref. [119][1], and we refer to that paper and to 1.6.2 for explicit formulas.

The dispersion relation of the staggered fermions,

$$\tan^2(k_x a/2) + \tan^2(k_y a/2) + \left(\frac{Mav}{2\hbar}\right)^2 = \left(\frac{\varepsilon a}{2\hbar v}\right)^2, \tag{2.8}$$

has a Dirac cone at wave vectors $|\boldsymbol{k}|a \ll 1$ which is gapped by a nonzero mass. Staggered fermions differ from Dirac fermions by the pole at the edge of Brillouin zone ($|k_x| \to \pi/a$ or $|k_y| \to \pi/a$), which is insensitive to the presence of a mass. We do not expect these large-wave number modes to affect the large-length scaling of the conductivity, because they preserve the electron-hole symmetry.

The energy is fixed at $\varepsilon = 0$ (corresponding to the Fermi level for the superconducting quasiparticles). The transfer matrix $\mathcal{T}$ is calculated recursively using a stable QR decomposition algorithm [65]. An alternative stabilization method [119] is used to recursively calculate the transmission matrix t. Both algorithms give consistent results, but the calculation of $\mathcal{T}$ is more accurate than that of t because it preserves the electron-hole symmetry irrespective of round-off errors.

The random mass is introduced by randomly choosing values of M on each site uniformly in the interval $(\bar{M} - \delta M, \bar{M} + \delta M)$. Variations of $M(\boldsymbol{r})$ on the scale of the lattice constant introduce Majorana bound states, which place the model in the *BD* symmetry class [127]. In principle, it is possible to study also the class *D* phase diagram (without Majorana bound states), by choosing a random mass landscape that is smooth on the scale of a. Such a study was recently performed [12], using a different model [11], to demonstrate the absence of the M–I transition in class *D* [97, 17, 98]. Since here we wish to study both the I–I and M–I transitions, we do not take a smooth mass landscape.

[1] This paper considers scattering of staggered fermions by a potential V rather than by a mass M, but one simply needs to replace V by $v^2 M\sigma_z$ to obtain the transfer matrix required here.

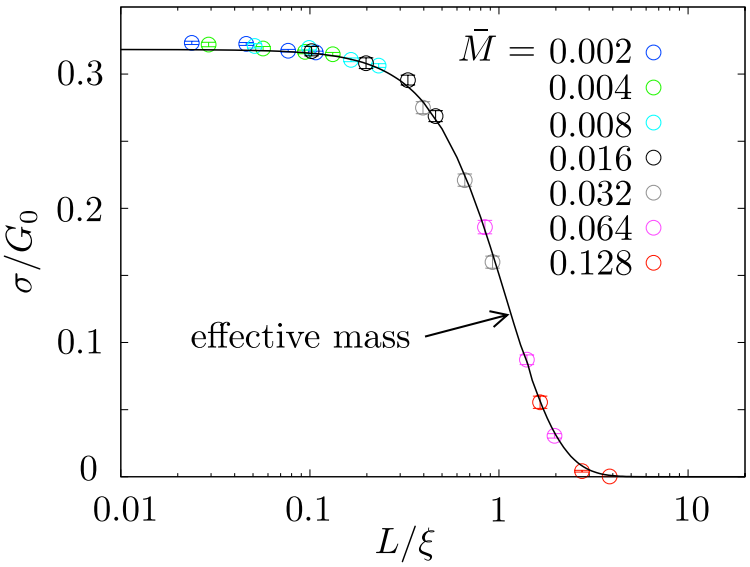

Figure 2.2. Average conductivity σ (with error bars indicating the statistical uncertainty) at fixed disorder strength $\delta M = 2.5\,\hbar/va$, as a function of system size L. The aspect ratio of the disordered strip is fixed at $W/L = 5$. Data sets at different values of $\bar{M}$ (listed in the figure in units of $\hbar/va$) collapse upon rescaling by ξ onto a single curve (solid line), given by Eq. (2.1) in terms of an effective mass $M_{\rm eff} = \hbar/v\xi$.

2.4 Scaling near the insulator-insulator transition

2.4.1 Scaling of the conductivity

In Fig. 2.2 we show the average (thermal) conductivity $\sigma = (L/W)\langle \mathrm{Tr}\, tt^\dagger \rangle$ (averaged over some 10^3 disorder realizations) as a function of L for a fixed δM in the localized phase. Data sets with different $\bar{M}$ collapse on a single curve upon rescaling with ξ. (In the logarithmic plot this rescaling amounts simply to a horizontal displacement of the entire data set.) The scaling curve (solid line in Fig. 2.2) is the effective mass conductivity (2.1), with $M_{\rm eff} = \hbar/v\xi$. Fig. 2.3 shows the linear scaling of σ with $(\bar{M}L)^2$ for small $\bar{M}$, as expected from Eq. (2.3) with $\nu = 1$.

We have studied the aspect ratio dependence of the critical conductivity σ_c. As illustrated in Fig. 2.4 (blue data points), the convergence for $W/L \to \infty$ is to the value $\sigma_c = 1/\pi$ expected from Eq. (2.1). The conductivity of ballistic massless Dirac fermions also has an aspect ratio

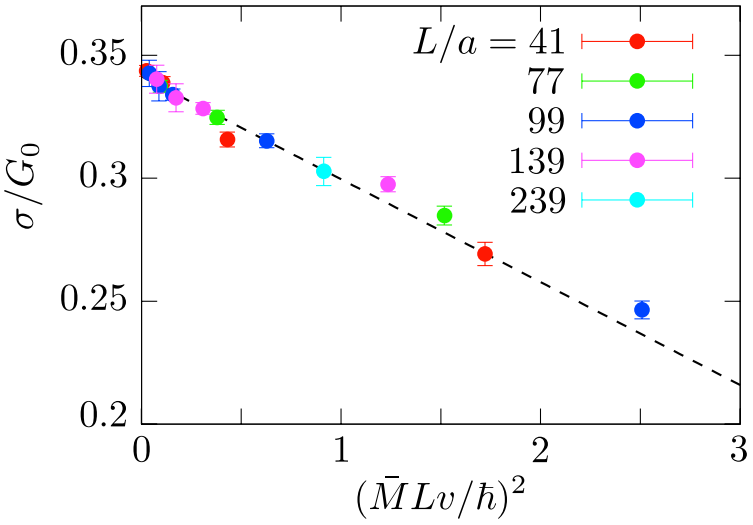

Figure 2.3. Plot of the average conductivity σ versus $(\bar{M}L)^2$, for fixed $\delta M = 2.5\,\hbar/va$ and $W/L = 3$. The dashed line is a least-square fit through the data, consistent with critical exponent $\nu = 1$.

dependence,[118] given by Eq. (2.2) (for periodic boundary conditions). The comparison in Fig. 2.4 of σ_c with Eq. (2.2) shows that σ_c at the I–I transition follows quite closely this aspect ratio dependence (unlike at the M–I transition discussed in Sec. 2.5.1).

2.4.2 Scaling of the Lyapunov exponent

The transfer matrix $\mathcal{T}$ provides an independent probe of the critical scaling through the Lyapunov exponents. The transfer matrix product $\mathcal{T}\mathcal{T}^\dagger$ has eigenvalues $e^{\pm\mu_n}$ with $0 \le \mu_1 \le \mu_2 \le \cdots$. The n-th Lyapunov exponent α_n is defined by

$$\alpha_n = \lim_{L\to\infty} \frac{\mu_n}{L}. \tag{2.9}$$

The dimensionless product $W\alpha_1 \equiv \Lambda$ is the inverse of the MacKinnon-Kramer parameter.[76] We obtain α_1 by increasing L at constant W until convergence is reached (typically for $L/W \simeq 10^3$). The large-L limit is self-averaging, but some improvement in statistical accuracy is reached by averaging over a small number (10–20) of disorder realizations.

We seek the coefficients in the scaling expansion

$$\Lambda = \Lambda_c + c_1 W^{1/\nu}(\bar{M} - M_c) + \mathcal{O}(\bar{M} - M_c)^2, \tag{2.10}$$

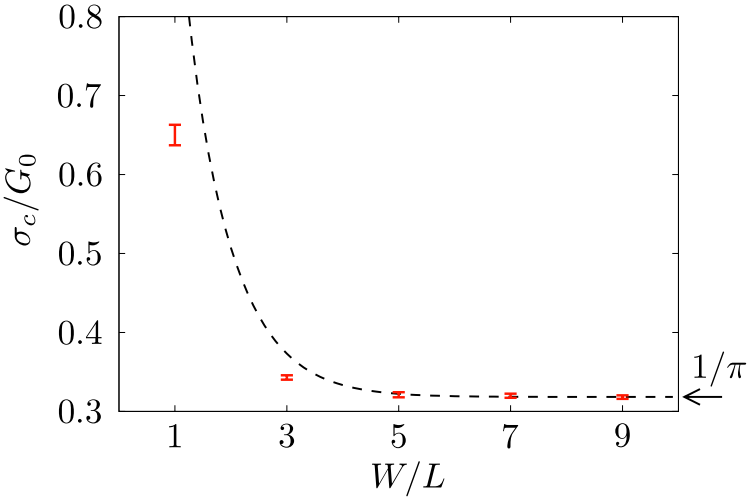

Figure 2.4. Dependence on the aspect ratio W/L of the critical conductivity at the insulator-insulator (I–I) transition ($\bar{M} = 0$, $\delta M = 2.5\,\hbar/va$) and at the metal-insulator (M–I) transition ($\bar{M} = 0.032\,\hbar/va$, δM tuned to the transition). The dashed curve is the aspect ratio dependence of the conductivity of ballistic massless Dirac fermions [Eq. (2.2)]. It describes the I–I transition quite well, but not the M–I transition.

for fixed δM. The fit in Fig. 2.5 gives $\Lambda_c = 0.03$, $\nu = 1.05$, $M_c = 7 \cdot 10^{-4}$, consistent with the expected values [23] $\Lambda_c = 0$, $\nu = 1$, $M_c = 0$.

2.5 Scaling near the metal-insulator transition

2.5.1 Scaling of the conductivity

To investigate the scaling near the metal-insulator transition, we increase δM at constant $\bar{M}$. Results for the conductivity are shown in Fig. 2.6. In the metallic regime $\delta M > \delta M_c$ the conductivity increases logarithmically with system size L, in accord with the theoretical prediction [109, 36]:

$$\sigma/G_0 = \frac{1}{\pi} \ln L + \text{constant}. \tag{2.11}$$

(See the dashed line in Fig. 2.6, upper panel.)

In the insulating regime $\delta M < \delta M_c$ the conductivity decays exponentially with system size, while it is scale independent at the critical

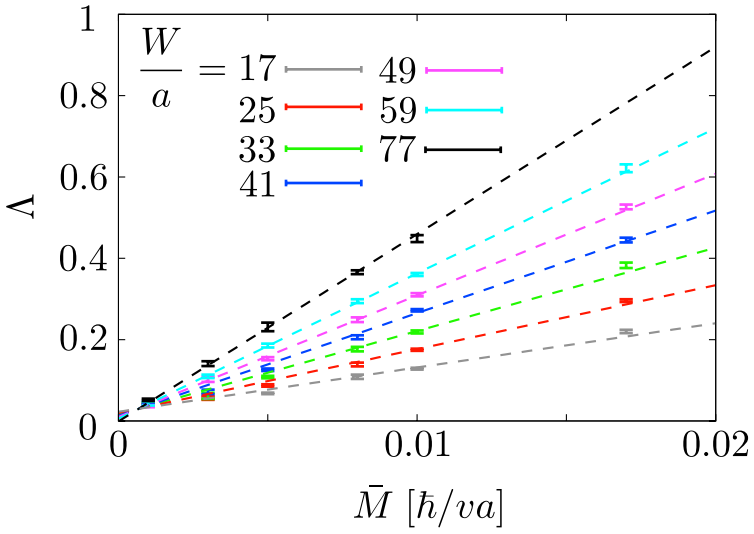

Figure 2.5. Plot of $\Lambda = W\alpha_1$ (with α_1 the first Lyapunov exponent) as a function of $\bar{M}$ near the insulator-insulator transition, for fixed $\delta M = 2.5\,\hbar v/a$ and different values of W. The dashed lines are a fit to Eq. (2.10).

point $\delta M = \delta M_c$. Data sets for different δM collapse onto a single function of L/ξ, but this function is different from the effective mass scaling $\sigma_0(L/\xi)$ of Eq. (2.1). (See the dashed curve in Fig. 2.6, lower panel.) This indicates that the effective mass description, which applies well near the insulator-insulator transition, breaks down at large disorder strengths near the metal-insulator transition. The two transitions therefore have a different scaling behavior, and can have different values of critical conductivity and critical exponent (which we denote by σ_c' and ν').

Indeed, the critical conductivity $\sigma_c' = 0.41\,G_0$ is significantly larger than the ballistic value $G_0/\pi = 0.32\,G_0$. Unlike at the insulator-insulator transition, we found no strong aspect-ratio dependence in the value of σ_c' (red data points in Fig. 2.4). To obtain the critical exponent ν' we follow Ref. [8] and fit the conductivity near the critical point including terms of second order in $\delta M - \delta M_c$:

$$\sigma = \sigma_c' + c_1 L^{1/\nu'}[\delta M - \delta M_c + c_2(\delta M - \delta M_c)^2] + c_3 L^{2/\nu'}(\delta M - \delta M_c)^2. \tag{2.12}$$

Results are shown in Fig. 2.7, with $\nu' = 1.02 \pm 0.06$. The quality of the multi-parameter fit is assured by a reduced chi-squared value close to unity

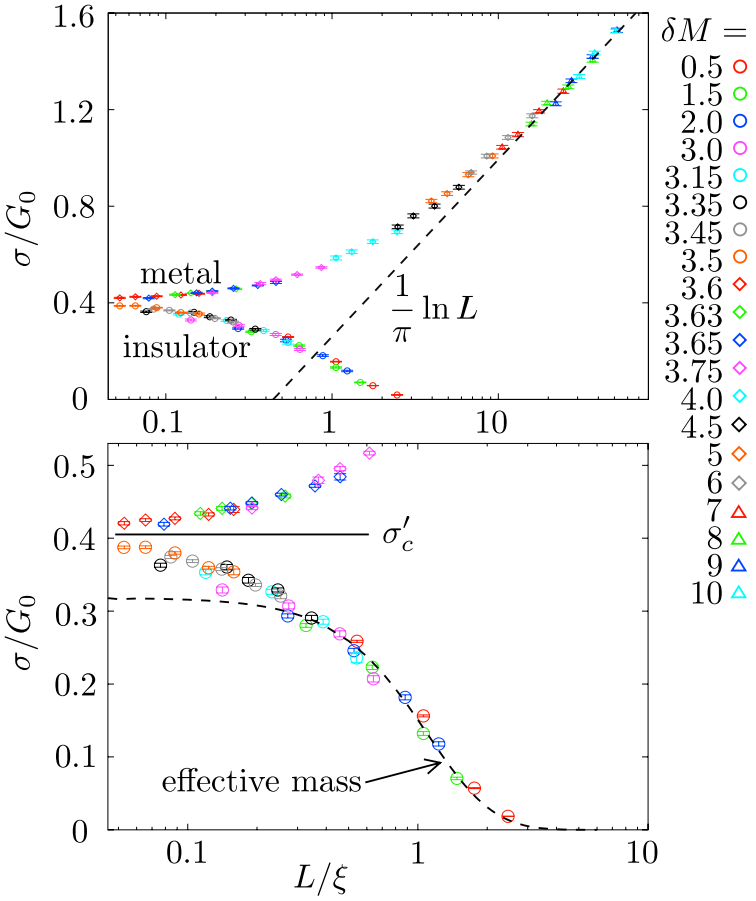

Figure 2.6. Average conductivity σ at fixed average mass $\bar{M} = 0.032\,\hbar/va$, as a function of system size L. (The two panels show the same data on a different scale.) The aspect ratio of the disordered strip is fixed at $W/L = 5$. Data sets at different values of δM (listed in the figure in units of $\hbar/va$) collapse upon rescaling by ξ onto a pair of curves in the metallic and insulating regimes. The metal-insulator transition has a scale invariant conductivity σ_c', larger than the value G_0/π which follows from the effective mass scaling (dashed curve in the lower panel). The upper panel shows that the conductivity in the metallic regime follows the logarithmic scaling (2.11).

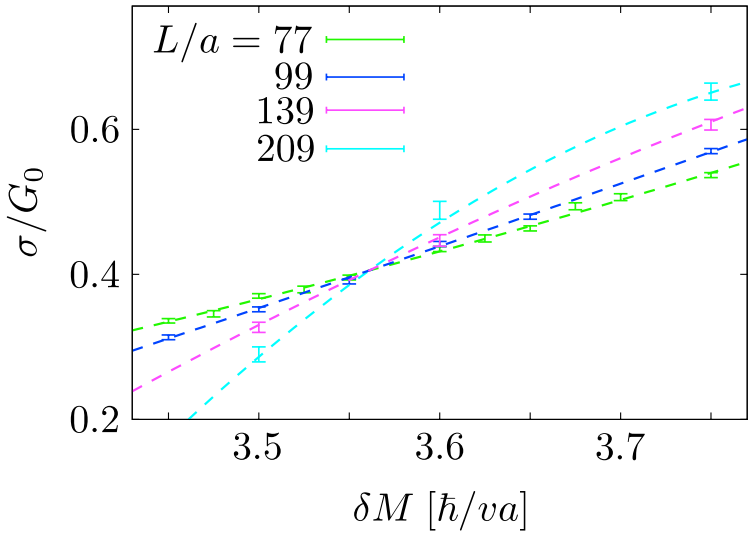

Figure 2.7. Plot of the average conductivity σ as a function of δM near the metal-insulator transition, for fixed $\bar{M} = 0.032\,\hbar/va$. The length L is varied at fixed aspect ratio $W/L = 3$. The dashed curves are a fit to Eq. (2.12).

($\chi^2 = 0.95$). Within error bars, this value of the critical exponent is the same as the value $\nu = 1$ for the insulator-insulator transition.

2.5.2 Scaling of the Lyapunov exponent

As an independent measurement of ν', we have investigated the finite-size scaling of the first Lyapunov exponent. Results are shown in Fig. 2.8. Within the framework of single-parameter scaling, the value of ν' should be the same for σ and Λ, but the other coefficients in the scaling law may differ,

$$\begin{aligned}\Lambda = \Lambda_c &+ c_1' L^{1/\nu'}[\delta M - \delta M_c' + c_2'(\delta M - \delta M_c')^2] \\ &+ c_3' L^{2/\nu'}(\delta M - \delta M_c')^2. \end{aligned} \tag{2.13}$$

Results are shown in Fig. 2.8, with $\nu' = 1.06 \pm 0.05$. The chi-squared value for this fit is relatively large, $\chi^2 = 5.0$, but the value of ν' is consistent with that obtained from the conductivity (Fig. 2.7).

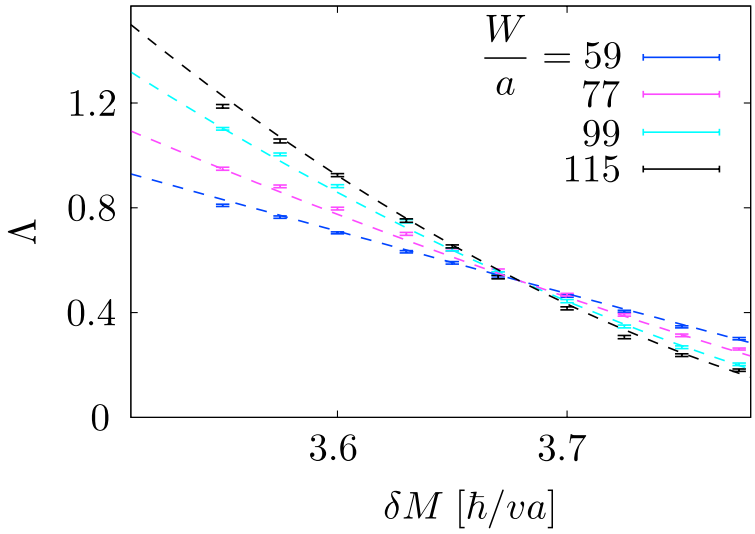

Figure 2.8. Plot of $\Lambda = W\alpha_1$ (with α_1 the first Lyapunov exponent) as a function of δM near the metal-insulator transition, for fixed $\bar{M} = 0.032\,\hbar v/a$ and different values of W. The dashed curves are a fit to Eq. (2.13).

2.6 Tricritical point

As indicated in the phase diagram of Fig. 2.1, the tricritical point at $\bar{M} = 0$, $\delta M = \delta M^*$ is the point at which the insulating phases at the two sides of the I–I transition meet the metallic phase. We have searched for this tricritical point by calculating the scale dependence of the conductivity σ on the line $\bar{M} = 0$ for different δM. Results are shown in Fig. 2.9.

The calculated scale dependence is consistent with the identification of the point $\delta M^* = 3.44\,\hbar/va$ as a *repulsive* fixed point. The conductivity increases with increasing L for $\delta M > \delta M^*$, while for $\delta M < \delta M^*$ it decreases towards the scale invariant large-L limit σ_c.

2.7 Discussion

We have studied quasiparticle localization in symmetry class *BD*, by means of a lattice fermion model [119]. The thermal quantum Hall effect [97, 109, 121] in a chiral p-wave superconductor at weak disorder is in this universality class, as is the phase transition to a thermal metal [109] at strong disorder.

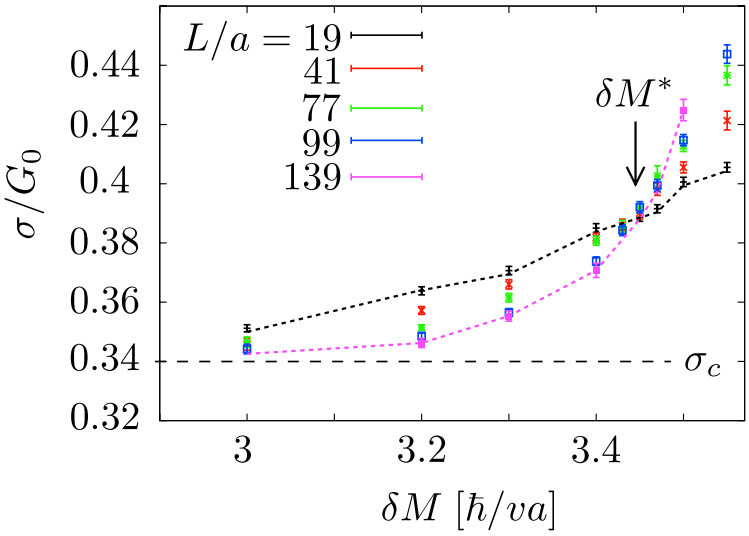

Figure 2.9. Conductivity σ as a function of δM on the critical line $\bar{M} = 0$, for different values of L at fixed aspect ratio $W/L = 3$. (The dotted lines through data points are guides to the eye.) The tricritical point δM^* is indicated, as well as the scale invariant large-L limit σ_c for $\delta M < \delta M^*$.

For weak disorder our lattice model can also be used to describe the localization of Dirac fermions in graphene with a random gap [12, 131, 132] (with σ the electrical, rather than thermal, conductivity and $G_0 = 4e^2/h$ the electrical conductance quantum). The metallic phase at strong disorder requires Majorana bound states [97, 17, 98], which do not exist in graphene (symmetry class D rather than BD). We therefore expect the scaling analysis in Sec. 2.4 at the insulator-insulator (I–I) transition to be applicable to chiral p-wave superconductors as well as to graphene, while the scaling analysis of Sec. 2.5 at the metal-insulator (M–I) transition applies only in the context of superconductivity. (Here we disagree with Refs. [131, 132], which maintain that the M–I transition exists in graphene as well.)

Our lattice fermion model is different from the network model [28] used in previous investigations [23, 80, 55, 56], but it falls in the same universality class so we expect the same critical conductivity and critical exponent. For the I–I transition analytical calculations [36, 75] give $\sigma_c = G_0/\pi$ and $\nu = 1$, in agreement with our numerics. There are no analytical results for the M–I transition. We find a slightly larger critical conductivity

($\sigma_c' = 0.4\,G_0$), which has the qualitatively more significant consequence that the effective mass scaling which we have demonstrated at the I–I transition breaks down at the M–I transition (compare Figs. 2.2 and 2.6, lower panel).

We conclude from our numerics that the critical exponents ν at the I–I transition and ν' at the M–I transition are both equal to unity within a 5% error margin, which is significantly smaller than the result $\nu = \nu' = 1.4 \pm 0.2$ of an earlier numerical investigation [55], but close to the value found in later work by these authors [56]. The logarithmic scaling (2.11) of the conductivity in the thermal metal phase, predicted analytically [109, 36], is nicely reproduced by our numerics (Fig. 2.6, upper panel).

The nature of the tricritical point has been much debated in the literature [80, 56]. Our numerics indicates that this is a repulsive critical point (Fig. 2.9). This finding lends support to the simplest scaling flow along the I–I phase boundary [75], towards the free-fermion fixed point at $\bar{M} = 0$, $\delta M = 0$.

In conclusion, we hope that this investigation brings us closer to a complete understanding of the phase diagram and scaling properties of the thermal quantum Hall effect. We now have two efficient numerical models in the *BD* universality class, the Cho-Fisher network model [28] studied previously and the lattice fermion model [119] studied here. There is a consensus on the scaling at weak disorder, although some disagreement on the scaling at strong disorder remains to be resolved.

Chapter 3

Absence of a metallic phase in charge-neutral graphene with a random gap

3.1 Introduction

Two-dimensional Anderson localization in the Dirac equation shows a much richer phase diagram than in the Schrödinger equation [75]. The discovery of graphene [45] has provided a laboratory for the exploration of this phase diagram and renewed the interest in the transport properties of Dirac fermions [36]. One of the discoveries resulting from these recent investigations [11, 86, 108] was that electrostatic potential fluctuations $V(\boldsymbol{r})$ induce a logarithmic growth of the conductivity $\sigma \propto \ln L$ with increasing system size L. In contrast, in the Schrödinger equation all states are localized by sufficiently strong potential fluctuations [69] and the conductivity decays exponentially with L.

Localized states appear in graphene if the carriers acquire a mass $M(\boldsymbol{r})$, for example due to the presence of a sublattice symmetry breaking substrate [46, 130] or due to adsorption of atomic hydrogen [35, 20]. Anderson localization due to the combination of (long-range) spatial fluctuations in $M(\boldsymbol{r})$ and $V(\boldsymbol{r})$ appears in the same way as in the quantum Hall effect (QHE) [75, 87]: All states are localized except on a phase boundary[1] of

[1]The localized phases at the two sides of the phase boundary at $\bar{M} = 0$ are distinguished by the presence or absence of chiral edge states. This is similar to the QHE, but the edge states produced by a mass in graphene do not lead to a Hall voltage be-

zero average mass $\bar{M} = 0$, where σ takes on a scale invariant value of the order of the conductance quantum $G_0 = 4e^2/h$ (the factor of four accounts for the two-fold spin and valley degeneracies in graphene).

An altogether different phase diagram may result if only the mass fluctuates, at constant electrostatic potential tuned to the charge neutrality point (Dirac point, at energy $E = 0$). The universality class is now different from the QHE, because of the particle-hole symmetry $\sigma_x H^* \sigma_x = -H$ of the single-valley Dirac Hamiltonian

$$H_{\text{Dirac}} = v(p_x\sigma_x + p_y\sigma_y) + v^2 M(\boldsymbol{r})\sigma_z. \tag{3.1}$$

The Pauli matrices σ_i act on the spinor (ψ_A, ψ_B), containing the wave function amplitudes on the A and B sublattices of graphene. The term proportional to σ_z represents a staggered sublattice potential, equal to v^2M ($-v^2M$) on sublattice A (B). Anderson localization in the presence of particle-hole symmetry has been studied extensively [28, 109, 23, 80, 55] in the context of superconductivity, where the Dirac spectrum appears from the superconducting order parameter rather than from the band structure. The (numerical) models used in those studies contain randomly distributed vortices in the order parameter, and are therefore not appropriate models for graphene.

It is the purpose of this chapter to identify, by numerical simulation, what is the phase diagram of the Dirac Hamiltonian with a random mass $M(\boldsymbol{r}) = \bar{M} + \delta M(\boldsymbol{r})$ — in the absence of any other source of disorder. This study was motivated by recent analytical work by Ziegler in the context of graphene [131], which predicted a transition into a metallic phase upon increasing the disorder strength δM at constant average mass $\bar{M} \neq 0$. Such a metal-insulator transition was known in the context of superconductivity [109], but it was understood that this requires vortex disorder [97, 17, 98]. In order to resolve this controversy, we perform a numerical scaling analysis of the conductivity and find no metallic phase as we increase δM.

cause they are counterprogating in the two valleys. In the computer simulations we use periodic boundary conditions, so there are no edge states and the two sides of the phase boundary are equivalent.

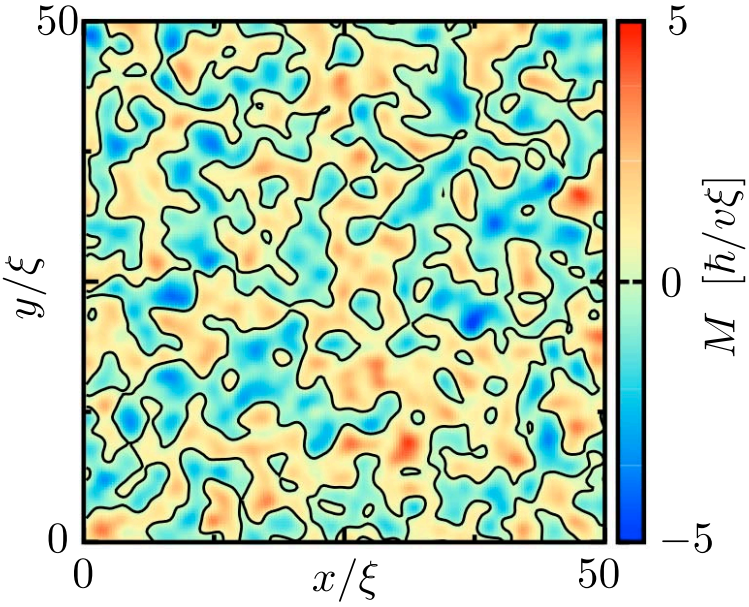

Figure 3.1. Contour plot of a random mass with Gaussian correlator (5.27), for $K_0 = 10$. The zero-mass contours are indicated in black.

3.2 Results

We calculate the conductivity σ for a two-dimensional strip geometry between electron reservoirs (at $x = 0$ and $x = L$, see inset in Fig. 3.2), with periodic boundary conditions in the transverse direction (at $y = 0$ and $y = W$). The Fermi level is tuned to the Dirac point in the strip, while it lies infinitely far above the Dirac point in the reservoirs. For zero mass M and large aspect ratio W/L the conductivity has the scale independent value [58, 118] $\sigma_0 = G_0/\pi$. We generate a random mass with Gaussian correlator

$$\langle \delta M(\boldsymbol{r}) \delta M(\boldsymbol{r}') \rangle = \frac{(\hbar/v)^2 K_0}{2\pi\xi^2} e^{-|\boldsymbol{r}-\boldsymbol{r}'|^2/2\xi^2}, \tag{3.2}$$

characterized by a correlation length ξ and a dimensionless strength

$$K_0 = (v/\hbar)^2 \int d\boldsymbol{r}\, \langle \delta M(0) \delta M(\boldsymbol{r}) \rangle. \tag{3.3}$$

A contour plot for a single realization of the disorder is shown in Fig. 3.1.

The $N \times N$ transmission matrix t through the strip is calculated from $H_{\rm Dirac}$ by application of the numerical method of Ref. [11] to a random

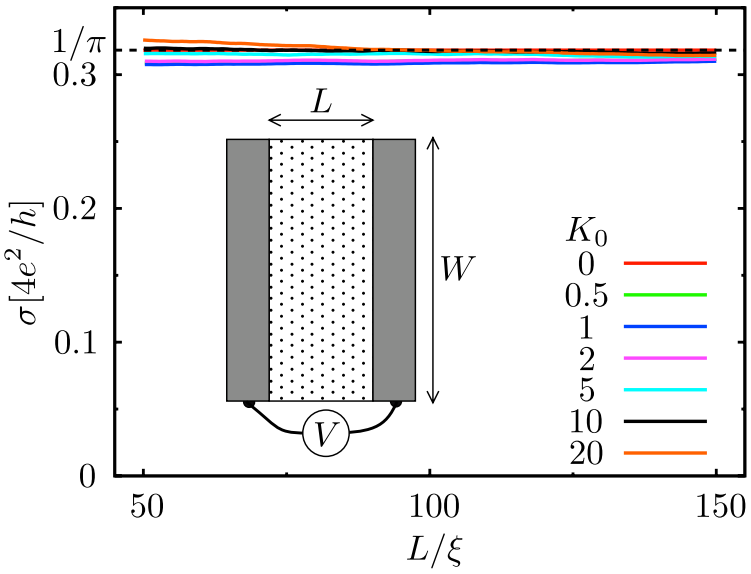

Figure 3.2. Average conductivity σ as a function of length L (for fixed $W = 800\,\xi$). The average mass is set at $\bar{M} = 0$, while the mass fluctuations are varied by varying K_0. The dashed line is at $\sigma_0/G_0 = 1/\pi$. The inset shows the layout of the disordered charge neutral strip (dotted rectangle) between infinitely doped electron reservoirs at a voltage difference V (gray rectangles).

mass rather than to a random scalar potential. We obtain t from the transfer matrix $\mathcal{T}$, which relates $|\psi(x = L)\rangle = \mathcal{T}|\psi(x = 0)\rangle$ and is given by

$$\mathcal{T} = \prod_{n=1}^{N_L} e^{\frac{1}{2}\delta x Q}\delta\mathcal{T}_n e^{\frac{1}{2}\delta x Q}, \quad Q = -i\sigma_z\frac{\partial}{\partial y} - \frac{v}{\hbar}\bar{M}\sigma_y. \tag{3.4}$$

Scattering from the fluctuating mass $\delta M(\boldsymbol{r})$ in the slice $(n-1)\delta x < x < n\delta x$, of incremental length $\delta x = L/N_L$, is approximated by the transfer matrix

$$\delta\mathcal{T}_n = \frac{1 - \frac{1}{2}\delta M_n(y)\sigma_y}{1 + \frac{1}{2}\delta M_n(y)\sigma_y}, \tag{3.5a}$$

$$\delta M_n(y) = \frac{v}{\hbar}\int_{(n-1)\delta x}^{n\delta x} dx\,\delta M(\boldsymbol{r}). \tag{3.5b}$$

The approximation (3.5) becomes exact in the limit $N_L \to \infty$. Moreover, for any N_L it satisfies the requirements of particle-hole symmetry

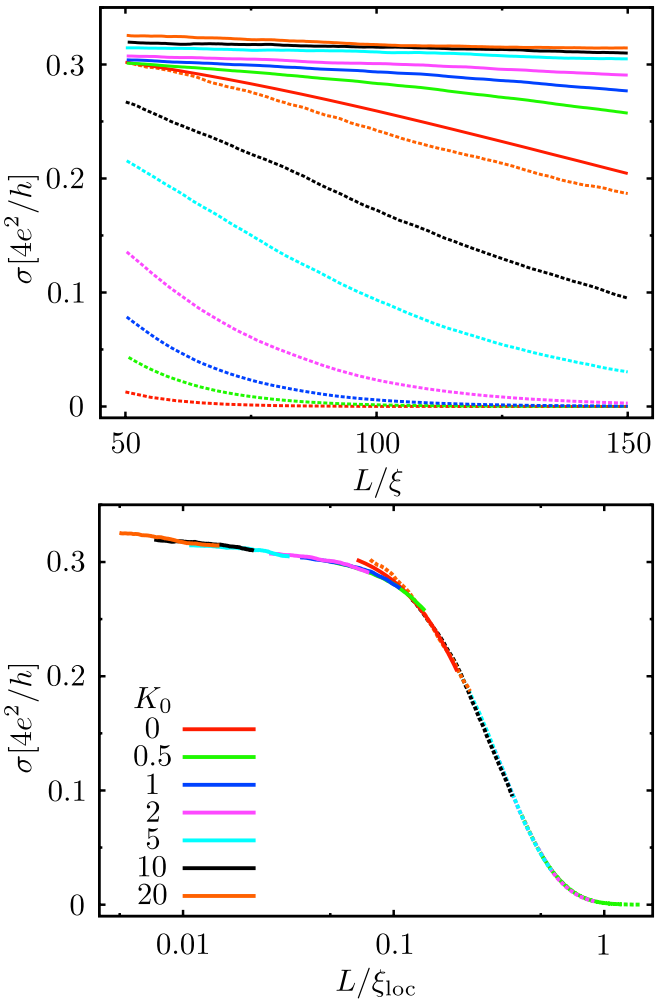

Figure 3.3. Same as Fig. 3.2, but now for a nonzero average mass $\bar{M} = 5 \cdot 10^{-3}\,\hbar/v\xi$ (solid curves, $W = 800\,\xi$) and $\bar{M} = 5 \cdot 10^{-2}\,\hbar/v\xi$ (dashed curves, $W = 400\,\xi$). The lower panel shows the same data on a logarithmic horizontal scale, rescaled by $\xi_{\mathrm{loc}} = \xi/f(K_0, \bar{M})$.

($\sigma_x \mathcal{T}^* \sigma_x = \mathcal{T}$) as well as current conservation ($\sigma_x \mathcal{T}^\dagger \sigma_x = \mathcal{T}^{-1}$).

We thus obtain the conductance $G = G_0 \mathrm{Tr}\, tt^\dagger$ and the conductivity $\sigma = G \times L/W$. The number of transverse modes N and longitudinal slices N_L are truncated at a finite value, which is increased until a sample specific convergence is reached. For the data presented, this is typically achieved when $N = 400$—800 and $N_L = 300$—600, the larger values needed for larger values of K_0. The sample width $W = 400\xi$—800ξ is chosen large enough that the conductivity is independent of the ratio W/L. (Typically, $W/L \gtrsim 3$—5, with the larger values needed for smaller values of $\bar{M}$.) Averages over a large number of disorder configurations (typically 1000) produce the results plotted in Figs. 3.2 and 3.3.

For $\bar{M} = 0$ (Fig. 3.2) the conductivity stays close to the scale invariant value σ_0 (dashed line), no matter how large the disorder strength, while for nonzero $\bar{M}$ (Fig. 3.3) the conductivity decays with increasing L. For sufficiently large L/ξ we expect single-parameter scaling, meaning that the data for different K_0 and $\bar{M}$ should all fall on a single curve upon rescaling $L \to f(K_0, \bar{M})L$. (This amounts to a horizontal displacement of data sets on a logarithmic horizontal scale.) The length $\xi_{\mathrm{loc}} = \xi / f(K_0, \bar{M})$ can then be identified with the localization length (up to a multiplicative constant). As one can see in the lower panel of Fig. 3.3, the data sets collapse reasonably well onto a single curve upon rescaling. (The remaining deviations may well be due to finite-size effects.)

For weak disorder ($K_0 < 1$) our results are similar to earlier work on the superconducting random mass model [28]. That model however shows a metal-insulator transition at values of $K_0 = K_c$ of order unity [23, 55] (weakly dependent on $\bar{M}$), such that for larger disorder the conductivity increases logarithmically with system size [36, 109]:

$$\sigma = \sigma_0 \ln(L/\xi), \quad \text{for} \quad K_0 > K_c \simeq 1. \tag{3.6}$$

As argued by Read, Green, and Ludwig [97, 98] and by Bocquet, Serban, and Zirnbauer [17], metallic conduction in a random mass landscape requires resonant transmission through contours of zero mass (the black contours in Fig. 3.1). These contours support a bound state at zero energy, if and only if they enclose an odd number of vortices. Without vortices, the phase shift accumulated upon circulating once along a zero-mass contour equals π — so there can be no bound state and hence no resonant transmission. (The π phase shift is the Berry phase of the rotating pseudospin $\boldsymbol{\sigma}$ in H_{Dirac}, without any dynamical phase shift because the energy

is zero.) Our numerical finding that there is no metallic conduction in the random mass landscape without vortex disorder is therefore consistent with these analytical considerations.

From the more recent analytical work by Ziegler [131] we would expect a transition into a phase with a scale invariant conductivity

$$\sigma_c = \sigma_0[1 - (\bar{M}/M_c)^2], \tag{3.7}$$

when $M_c = (\hbar/v\xi)\exp(-\pi/K_0)$ becomes larger than $\bar{M}$ with increasing disorder strength K_0. The corresponding critical disorder strength $K_c = \pi/\ln|v\xi/\hbar\bar{M}| \approx 0.6$—$1.0$ for the values of $\bar{M}$ in Fig. 3.3. The numerical findings of Fig. 3.3, with a decaying conductivity for $K_0 > 10K_c$, do not support this prediction of a nonzero M_c. Note that the numerical data of Fig. 3.2, with a scale invariant conductivity $\sigma_c = \sigma_0$ for $\bar{M} = 0$, does agree with Eq. (3.7) — it is the $\bar{M} > 0$ data that is in disagreement.

3.3 Discussion

In conclusion, we have presented numerical calculations that demonstrate the absence of metallic conduction for the Dirac Hamiltonian (3.1), in a random mass landscape with nonzero average and dimensionless variance $K_0 \gg 1$. The decay of the conductivity with system size L is slower for larger disorder strengths, but no metal-insulator transition is observed. A transition into a metallic phase (with $\sigma \propto \ln L$) has been attributed to vortex disorder [97, 17, 98]. Our numerical results are consistent with this attribution, since our model contains no vortices and has no metallic phase even if $K_0 \gg 1$.

Chapter 4

Majorana bound states without vortices in topological superconductors with electrostatic defects

4.1 Introduction

Two-dimensional superconductors with spin-polarized-triplet, p-wave pairing symmetry have the unusual property that vortices in the order parameter can bind a nondegenerate state with zero excitation energy [64, 124, 97, 53]. Such a midgap state is called a Majorana bound state, because the corresponding quasiparticle excitation is a Majorana fermion — equal to its own antiparticle. A pair of spatially separated Majorana bound states encodes a qubit, in a way which is protected from any local source of decoherence [62]. Since such a qubit might form the building block of a topological quantum computer [84], there is an intensive search [57, 116, 105, 106, 68, 4] for two-dimensional superconductors with the required combination of broken time-reversal and spin-rotation symmetries (symmetry class D [6]).

The generic Bogoliubov-De Gennes Hamiltonian H of a chiral p-wave superconductor is only constrained by particle-hole symmetry, $\sigma_x H^* \sigma_x = -H$. At low excitation energies E (to second order in momentum $\boldsymbol{p} =$

$-i\hbar\partial/\partial\boldsymbol{r}$) it has the form

$$H = \Delta\big(p_x\sigma_x + p_y\sigma_y\big) + \big(U(\boldsymbol{r}) + p^2/2m\big)\sigma_z, \tag{4.1}$$

for a uniform (vortex-free) pair potential Δ. The electrostatic potential U (measured relative to the Fermi energy) opens up a band gap in the excitation spectrum. At $U = 0$ the superconductor has a topological phase transition (known as the thermal quantum Hall effect) between two localized phases, one with and one without chiral edge states [123, 109, 121, 122].

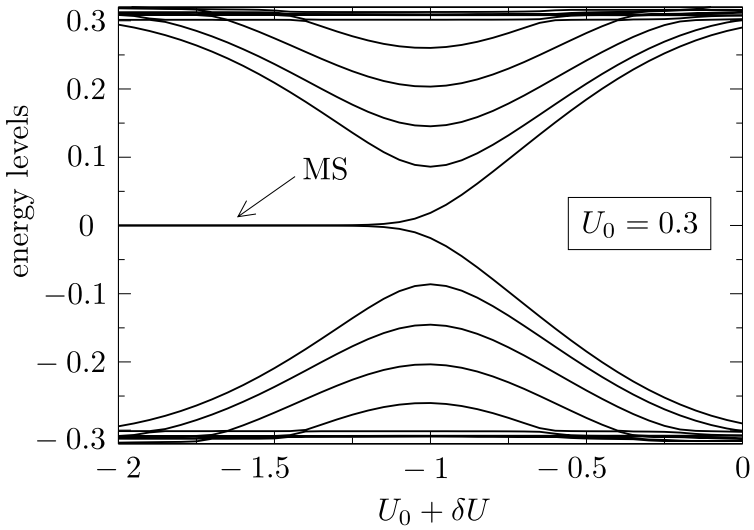

Figure 4.1. Emergence of a pair of zero-energy MS states as the defect potential $U_0 + \delta U$ is made more and more negative, at fixed positive background potential $U_0 = 0.3$. (All energies are in units of $\gamma \equiv \hbar\Delta/a$.) The energy levels are the eigenvalues of the Hamiltonian (4.1) on a square lattice (dimension $100\,a \times 100\,a$, $\beta \equiv \hbar^2/2ma^2 = 0.4\,\gamma$, periodic boundary conditions). The line defect has length $50\,a$. The dense spectrum at top and bottom consists of bulk states.

4.2 Majorana-Shockley bound states in lattice Hamiltonians

Our key observation is that the Hamiltonian (4.1) on a lattice has Majorana bound states at the two end points of a linear electrostatic defect

(consisting of a perturbation of U on a string of lattice sites). The mechanism for the production of these bound states goes back to Shockley [110]: The band gap closes and then reopens upon formation of the defect, and as it reopens a pair of states splits off from the band edges to form localized states at the end points of the defect (see Fig. 4.1). Such Shockley states appear in systems as varied as metals and narrow-band semiconductors [31], carbon nanotubes [107], and photonic crystals [77]. In these systems they are unprotected and can be pushed out of the band gap by local perturbations. In a superconductor, in contrast, particle-hole symmetry requires the spectrum to be $\pm E$ symmetric, so an isolated bound state is constrained to lie at $E = 0$ and cannot be removed by any local perturbation.

We propose the name Majorana-Shockley (MS) bound state for this special type of topologically protected Shockley states. Similar states have been studied in the context of lattice gauge theory by Creutz and Horváth [30, 29], for an altogether different purpose (as a way to restore chiral symmetry in the Wilson fermion model of QCD [126]).

Consider a square lattice (lattice constant a), at uniform potential U_0. The Hamiltonian (4.1) on the lattice has dispersion relation

$$E^2 = [U_0 + 2\beta(2 - \cos ak_x - \cos ak_y)]^2 + \gamma^2 \sin^2 ak_x + \gamma^2 \sin^2 ak_y. \quad (4.2)$$

(We have defined the energy scales $\beta = \hbar^2/2ma^2$, $\gamma = \hbar\Delta/a$.) The spectrum becomes gapless for $U_0 = 0$, -4β, and -8β, signaling a topological phase transition [95]. The number of edge states is zero for $U_0 > 0$ and $U_0 < -8\beta$, while it is unity otherwise (with a reversal of the direction of propagation at $U_0 = -4\beta$). The topologically nontrivial regime is therefore reached for U_0 negative, but larger than -8β.

We now introduce the electrostatic line defect by changing the potential to $U_0 + \delta U$ on the N lattice points at $\boldsymbol{r} = (na, 0)$, $n = 1, 2, \ldots N$. In Figs. 4.1 and 4.2 we show the closing and reopening of the band gap as the defect is introduced, accompanied by the emergence of a pair of states at zero energy. The eigenstates for which the gap closes and reopens have wave vector k_x parallel to the line defect equal to either 0 or $\pm\pi/a$ (in the limit $N \to \infty$ when k_x is a good quantum number).

We have calculated that the gap closing at $k_x = 0$ happens at a critical

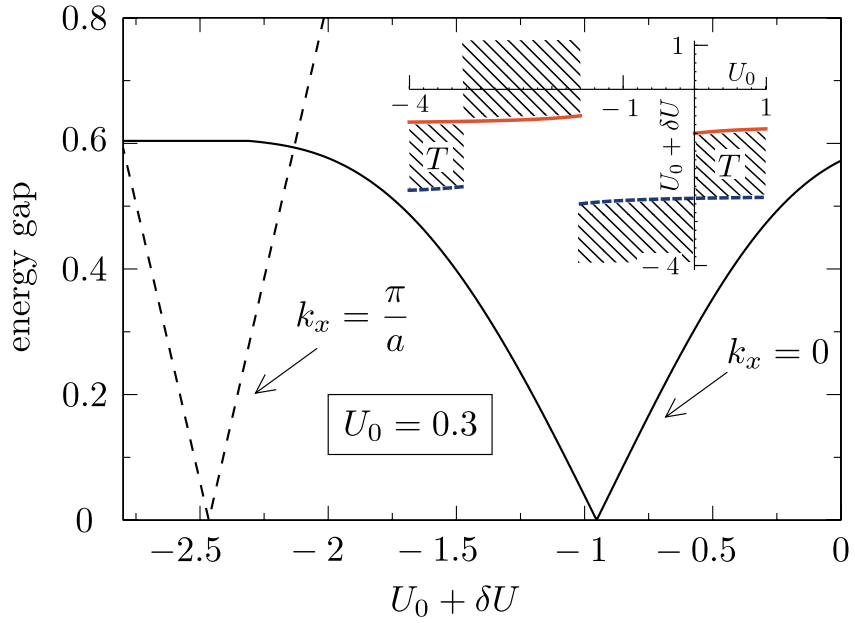

Figure 4.2. Main plot: Closing and reopening of the excitation gap at $U_0 = 0.3$, $\beta = 0.4$ (in units of γ), for states with $k_x = 0$ (black solid curve) and $k_x = \pi/a$ (black dashed curve). The MS states exist for defect potentials in between two gap-closings, indicated as a function of U_0 by the shaded regions in the inset. (The red solid and blue dashed curves show, respectively $U_0 + \delta U_0$ and $U_0 + \delta U_\pi$. The label T indicates the topologically trivial phase.)

potential $\delta U = \delta U_0$ given by (derived in Section 4.A)

$$\delta U_0 = \begin{cases} -\sqrt{U_0(U_0+4\beta)+\gamma^2} & \text{for } U_0 > 0, \\ \sqrt{U_0(U_0+4\beta)+\gamma^2} & \text{for } U_0 < -4\beta, \\ \text{no finite value otherwise.} \end{cases} \tag{4.3}$$

The critical potential δU_π for closing of the gap at $k_x = \pm\pi/a$ is obtained from Eq. (4.3) by the replacement of U_0 with $U_0 + 4\beta$. The MS states appear for defect potentials $U_0 + \delta U$ in between two subsequent gap closings, as indicated in the inset of Fig. 4.2.

We conclude that MS states exist for any value of U_0. In contrast, Majorana bound states in vortices exist only in the topologically nontrivial regime [97, 47]. The index theorem [101] for the production of zero-energy modes by the vortex mechanism, which requires the topologically nontrivial phase, is therefore not applicable to the Shockley mechanism.

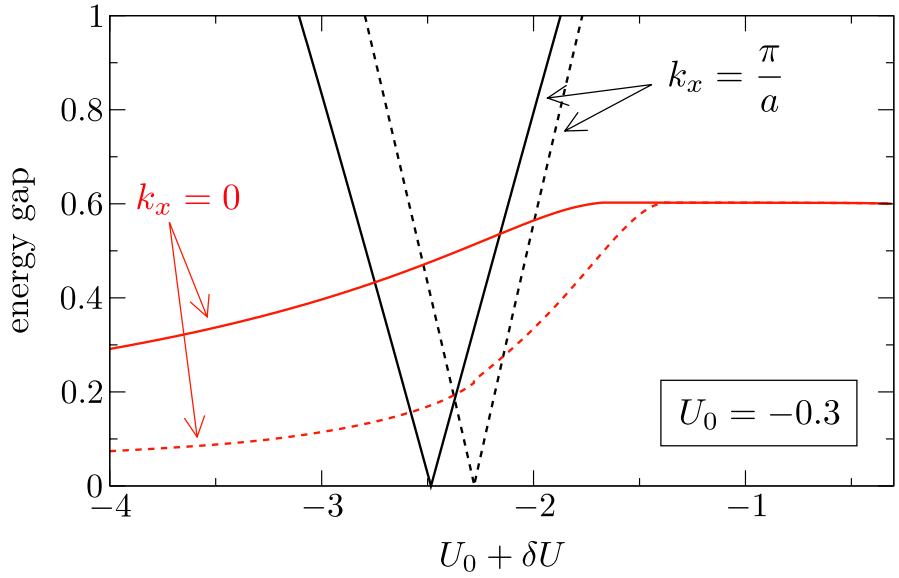

Figure 4.3. Closing and reopening of the excitation gap at $U_0 = -0.3$, $\beta = 0.4$ (in units of γ), for states with $k_x = 0$ (red curves) and $k_x = \pi/a$ (black curves). The results were obtained from numerical calculations using a constant isotropic pair potential Δ (solid lines) as in Fig. 4.2 as well as a spatially dependent, anisotropic pair potential $(\Delta_x(\boldsymbol{r}), \Delta_y(\boldsymbol{r}))$ determined self-consistently from the gap equation (dashed lines), Sec. 4.B.

Our reasoning so far has relied on the assumption of a constant pair potential Δ, unperturbed by the defect. In order to demonstrate the robustness of the Majorana-Shockley mechanism, we have performed numerical calculations that determine the pair potential self-consistently by means of the gap equation [44], Sec. 4.B. In Fig. 4.3 we show a comparison of the closing and reopening of the band gap as obtained from calculations with and without self-consistency, in the relevant weak pairing regime ($U_0 < 0$). The self-consistency does not change the qualitative behavior. In particular, the gap only closes at $k_x = \pi/a$ for the parameters chosen (c.f. inset in Fig. 4.2) and the self-consistent determination of Δ only shifts the critical potential δU slightly.

In Fig. 4.4 we demonstrate that the MS states are localized at the end points of the line defect. The exponentially small, but nonzero overlap of the pair of states displaces their energy from 0 to $\pm E$ (with corresponding eigenstates $\psi_- = \sigma_x \psi_+^*$ related by particle-hole symmetry). The unpaired

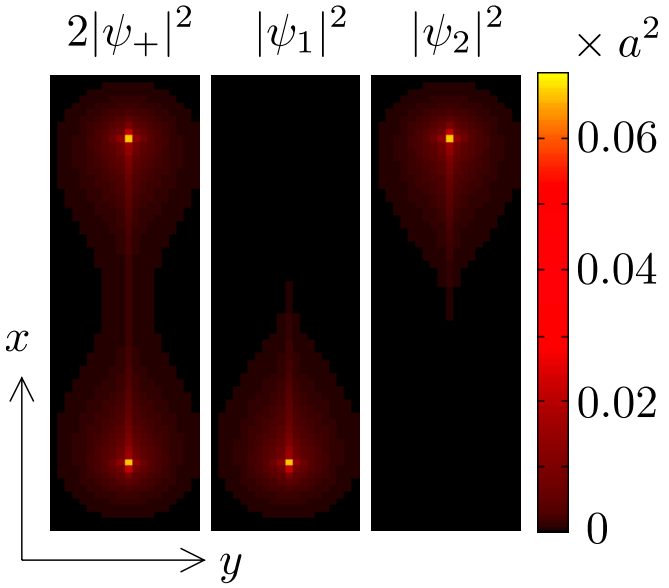

Figure 4.4. Probability density of the paired (ψ_+) and unpaired (ψ_1, ψ_2) Majorana bound states at the end points of a line defect of length $50\,a$, calculated for $U_0 = 0.1\,\gamma$, $U_0 + \delta U = -1.3\,\gamma$, $\beta = 0.4\,\gamma$.

Majorana bound states ψ_1 and ψ_2 are given by the linear combinations

$$\psi_1 = \tfrac{1}{2}(1-i)\psi_+ + \tfrac{1}{2}(1+i)\psi_-, \tag{4.4a}$$
$$\psi_2 = \tfrac{1}{2}(1+i)\psi_+ + \tfrac{1}{2}(1-i)\psi_-, \tag{4.4b}$$

shown also in Fig. 4.4. These states are particle-hole symmetric, $\psi_{1,2} = \sigma_x \psi_{1,2}^*$, so the quasiparticle in such a state is indeed equal to its own antiparticle (hence, it is a Majorana fermion).

If the line defect has a width W which extends over several lattice sites, multiple gap closings and reopenings appear at $k_x = 0$ upon increasing the defect potential $U_0 + \delta U \equiv -(\hbar k_F)^2/2m$ to more and more negative values at fixed positive background potential U_0. In the continuum limit $W/a \to \infty$, the gap closes when $qW = n\pi + \nu$, $n = 0, 1, 2, \ldots$ (Sec. 4.C), with $q = [k_F^2 - (m\Delta)^2]^{1/2}$ the real part of the transverse wave vector and $\nu \in (0, \pi)$ a phase shift that depends weakly on the potential. (Similar oscillatory coupling energies of zero-modes have been found in Refs. [26, 73].) The MS states at the two ends of the line defect alternatingly appear and disappear at each subsequent gap closing.

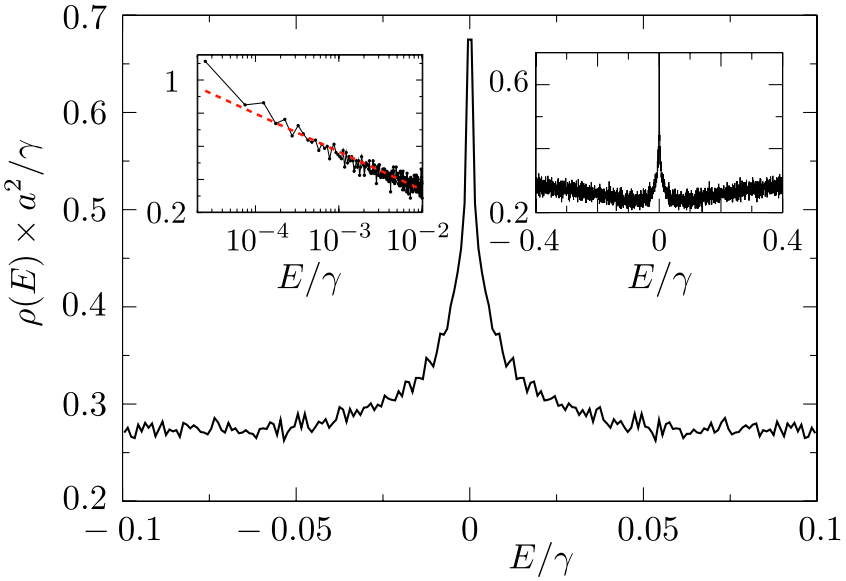

Figure 4.5. Average density of states for a potential that fluctuates randomly from site to site ($\bar{U} = 0.01\,\gamma$, $\Delta U = 2\,\gamma$, $\beta = 0.2\,\gamma$). The lattice has size $400\,a \times 400\,a$. The right inset shows the same data as in the main plot, over a larger energy range. The left inset has a logarithmic energy scale, to show the dependence $\rho \propto \ln|E|$ expected for a thermal metal (red dashed line).

4.3 Electrostatic disorder in p-wave superconductors

So far we constructed MS states for a linear electrostatic defect. More generally, we expect a randomly varying electrostatic potential to create a random arrangement of MS states. To test this, we pick $U(\mathbf{r})$ at each lattice point uniformly from the interval $(\bar{U} - \Delta U, \bar{U} + \Delta U)$ and calculate the average density of states $\rho(E)$. The result in Fig. 4.5 shows the expected peak at $E = 0$. This peak is characteristic of a thermal metal, studied previously in models where the Majorana bound states are due to vortices [17, 23, 80]. The theory of a thermal metal [109] predicts a logarithmic profile, $\rho(E) \propto \ln|E|$, for the peak in the density of states, which is consistent with our data.

Without Majorana bound states, the chiral p-wave superconductor would be in the thermal insulator phase, with an exponentially small thermal conductivity at any nonzero $\bar{U}$ [97, 17, 98, 12]. Our findings imply

that electrostatic disorder can convert the thermal insulator into a thermal metal, thereby destroying the thermal quantum Hall effect. Numerical results for this insulator-metal transition are shown in chapter 2.

4.4 Continuum limit for electrostatic defects

These results are all for a specific model of a chiral p-wave superconductor. We will now argue that our findings are generic for symmetry class D (along the lines of a similar analysis of solitons in a polymer chain [54]). Let p be the momentum along the line defect and α a parameter that controls the strength of the defect. Assume that the gap closes at $\alpha = \alpha_0$ and at $p = 0$. (Because of particle-hole symmetry the gap can only close at $p = 0$ or $p = \pm\hbar\pi/a$ and these two cases are equivalent.) For α near α_0 and p near 0 the Hamiltonian in the basis of left-movers and right-movers has the generic form

$$H(\alpha) = \begin{pmatrix} (v_0 + v_1)p & -i(\alpha - \alpha_0) \\ i(\alpha - \alpha_0) & -(v_0 - v_1)p \end{pmatrix}, \tag{4.5}$$

with velocities $0 < v_1 < v_0$. No other terms to first order in $p = -i\hbar\partial/\partial x$ and $\alpha - \alpha_0$ are allowed by particle-hole symmetry, $H(\alpha) = -H^*(\alpha)$.

The line defect is initially formed by letting α depend on x on a scale much larger than the lattice constant. We set one end of the defect at $x = 0$ and increase α from $\alpha(-\infty) < \alpha_0$ to $\alpha(+\infty) > \alpha_0$. Integration of $H[\alpha(x)]\psi(x) = 0$ then gives the wave function of a zero-energy state bound to this end point,

$$\psi(x) = \begin{pmatrix} \sqrt{v_0/v_1 - 1} \\ \sqrt{v_0/v_1 + 1} \end{pmatrix} \exp\left(- \int_0^x \frac{\alpha(x') - \alpha_0}{\sqrt{v_0^2 - v_1^2}}\, dx' \right). \tag{4.6}$$

This is one of the two MS states, the second being at the other end of the line defect. We may now relax the assumption of a slowly varying $\alpha(x)$, since a pair of uncoupled zero-energy states cannot disappear without violating particle-hole symmetry.

4.5 Outlook

We have identified a purely electrostatic mechanism for the creation of Majorana bound states in chiral p-wave superconductors. The zero-energy

(mid-gap) states appear in much the same way as Shockley states in non-superconducting materials, but now protected from any local perturbation by particle-hole symmetry. An experimentally relevant consequence of our findings is that the thermal quantum Hall effect is destroyed by electrostatic disorder (in marked contrast to the electrical quantum Hall effect). A recent proposal to realize Wilson fermions in optical lattices [16] also opens the possibility to observe Majorana-Shockley states using cold atoms.

Our analysis is based on a generic model of a two-dimensional class-D superconductor (broken time-reversal and spin-rotation symmetry). An interesting direction for future research is to explore whether Majorana-Shockley bound states exist as well in the other symmetry classes [6]. Since an electrostatic defect preserves time-reversal symmetry, we expect the Majorana-Shockley mechanism to be effective also in class *DIII* (when only spin-rotation symmetry is broken). That class includes proximity-induced s-wave superconductivity at the surface of a topological insulator [42] and other experimentally relevant topological superconductors [96, 103, 43].

It would also be interesting to investigate the braiding of two electrostatic defect lines, in order to see whether one obtains the same non-Abelian statistics as for the braiding of vortices [53].

Appendix 4.A Line defect in lattice fermion models

We calculate the closing and reopening of the excitation gap upon introduction of a line defect in a lattice fermion model with particle-hole symmetry. First we treat the Wilson fermion model [126] considered in the main text, and introduced in the context of topological insulators in Refs. [15, 41]. Then, in order to demonstrate the generic nature of the results, we consider an alternative lattice model, the staggered fermion (or Kogut-Susskind) model [63, 113, 14], introduced in the context of graphene in Refs. [119, 79].

4.A.1 Wilson fermions

The Wilson fermion model has Hamiltonian

$$H = \sum_n c_n^\dagger \mathcal{E}_n c_n - \sum_{n,m \text{ (nearest neighb.)}} c_n^\dagger \mathcal{T}_{nm} c_m. \tag{4.7}$$

Each site n on a two-dimensional square lattice (lattice constant a) has electron and hole states $|e\rangle$ and $|h\rangle$. Fermion annihilation operators for these two states are collected in a vector $c_n = (c_{n,e}, c_{n,h})$. States on the same site are coupled by the 2×2 potential matrix $\mathcal{E}_n$ and states on adjacent sites by the 2×2 hopping matrix $\mathcal{T}_{nm}$, defined by [15, 41]

$$\mathcal{E}_n = \begin{pmatrix} U_n & 0 \\ 0 & -U_n \end{pmatrix}, \quad \mathcal{T}_{nm} = \begin{pmatrix} \beta & \gamma e^{i\theta_{nm}} \\ \gamma e^{-i\theta_{mn}} & -\beta \end{pmatrix}. \tag{4.8}$$

Here U_n is the electrostatic potential on site n and $\theta_{nm} \in [0, \pi]$ is the angle between the vector $\boldsymbol{r}_n - \boldsymbol{r}_m$ and the positive y-axis (so $\theta_{mn} = \pi - \theta_{nm}$). In the continuum limit $a \to 0$, the tight-binding Hamiltonian (4.7) is equivalent to the chiral p-wave Hamiltonian (4.1), with $\beta = \hbar^2/2ma^2$ and $\gamma = \hbar\Delta/a$.

It is convenient to transform from position to momentum representation. For that purpose we take periodic boundary conditions in the y-direction, so that the transverse wavevector (in units of $1/a$) has the discrete values $k_l = 2\pi l/N$, $l = -(N-1)/2, \ldots, -1, 0, 1, \ldots, (N-1)/2$ (for an odd number N of sites in the y-direction). The Fourier transformation from position to momentum representation is carried out by the unitary matrix with elements $[\mathcal{F}]_{nl} = N^{-1/2} e^{ink_l}$. We take an infinitely long system in the x-direction, so the longitudinal wavevector k varies continuously in the interval $(-\pi, \pi]$.

For a uniform potential, $U_n \equiv U_0$ for all n, the Fourier transformed Hamiltonian $H_0(k)$ has matrix elements

$$[H_0(k)]_{ll'} = \delta_{ll'} \mathcal{E}_l(k), \tag{4.9}$$

$$\mathcal{E}_l(k) = U_0 \sigma_z + 2\beta\sigma_z(2 - \cos k - \cos k_l) + \gamma(\sigma_x \sin k + \sigma_y \sin k_l). \tag{4.10}$$

The corresponding dispersion relation is

$$\begin{aligned} E(k, k_l)^2 = {} & [U_0 + 2\beta(2 - \cos k - \cos k_l)]^2 \\ & + \gamma^2(\sin^2 k + \sin^2 k_l), \end{aligned} \tag{4.11}$$

cf. Eq. (4.2).

A line defect at row n_0 (parallel to the x-axis) adds to H_0 the perturbation

$$[\delta H]_{ll'} = N^{-1} e^{in_0(k_{l'} - k_l)} \delta U \sigma_z. \tag{4.12}$$

The determinantal equation $\mathrm{Det}\,(H_0 + \delta H - E) = 0$ for eigenenergy E reads

$$\mathrm{Det}\,(1 + \mathcal{F}_0^\dagger \delta U \sigma_z \mathcal{F}_0 (H_0 - E)^{-1}) = 0, \tag{4.13}$$

in terms of an $1 \times N$ matrix $\mathcal{F}_0$ with elements $[\mathcal{F}_0]_{1l} = N^{-1/2} e^{i n_0 k_l}$. Sylvester's theorem, $\mathrm{Det}(1 + AB) = \mathrm{Det}(1 + BA)$, allows us to rewrite the determinant in the form

$$\mathrm{Det}\,(1 + \delta U \sigma_z \mathcal{F}_0 (H_0 - E)^{-1} \mathcal{F}_0^\dagger) = 0, \tag{4.14}$$

which reduces to

$$\begin{aligned} 0 &= \mathrm{Det}\,\left(1 + \delta U \sigma_z \frac{1}{N} \sum_l \frac{1}{\mathcal{E}_l(k) - E}\right) \\ &= \mathrm{Det}\,\left(1 + \delta U \sigma_z \frac{1}{N} \sum_l \frac{\mathcal{E}_l(k) + E}{E(k,k_l)^2 - E^2}\right). \end{aligned} \tag{4.15}$$

A zero-mode is a pair of states (one left-mover and one right-mover) at energy $E = 0$. This can only occur at $k = 0$ or $k = \pi$ (because for any eigenenergy E at k there must also be an eigenenergy $-E$ at $-k$). From Eqs. (4.10) and (4.15) we obtain the condition for such a zero-mode,

$$\frac{1}{N} \sum_l \frac{U_0 + 2\beta(1 + \delta - \cos k_l)}{[U_0 + 2\beta(1 + \delta - \cos k_l)]^2 + \gamma^2 \sin^2 k_l} = -\frac{1}{\delta U}, \tag{4.16}$$

where $\delta = 0$ if $k = 0$ and $\delta = 2$ if $k = \pi$. In the limit $N \to \infty$ we may replace the sum by an integral, $N^{-1} \sum_l \to (2\pi)^{-1} \int_{-\pi}^{\pi} dk_l$, which can be evaluated by contour integration. The resulting critical value of δU is given in the main text [Eq. (4.3) and following].

4.A.2 Staggered fermions

The staggered fermion model is a discretization of the Hamiltonian (4.1) without the p^2 term. It is formulated in Refs. [113, 14, 119] in terms of the transfer matrix $\mathcal{M}_m$, which relates the transverse wave functions $\Psi_{m+1} = \mathcal{M}_m \Psi_m$ at columns m and $m + 1$ (parallel to the y-axis). For a line defect along the x-axis, the transfer matrix is m-independent, so we can omit the column number m.

The transfer matrix (at energy E) has the form

$$\mathcal{M} = \frac{1 - iX}{1 + iX}, \tag{4.17}$$

$$X = (\gamma\mathcal{J})^{-1}(\gamma\sigma_z\mathcal{K} + \tfrac{1}{2}E\sigma_x\mathcal{J} - \tfrac{1}{2}i\sigma_y\mathcal{U}). \tag{4.18}$$

In reference to Eq. (4.1), the parameter $\gamma = \hbar\Delta/a$ for lattice constant a. The $N \times N$ matrices $\mathcal{J}$ and $\mathcal{K}$ have nonzero elements

$$\mathcal{J}_{n,n} = 1, \;\; \mathcal{J}_{n,n+1} = \mathcal{J}_{n,n-1} = \tfrac{1}{2}, \tag{4.19}$$

$$\mathcal{K}_{n,n+1} = \tfrac{1}{2}, \;\; \mathcal{K}_{n,n-1} = -\tfrac{1}{2}, \tag{4.20}$$

while the potential matrix $\mathcal{U}$ (for a line defect at row n_0) is given by

$$\begin{aligned}\mathcal{U}_{nn'} = U_0\mathcal{J}_{nn'} + \tfrac{1}{2}\delta U(&\delta_{n,n'}\delta_{n,n_0} + \delta_{n,n'}\delta_{n,n_0+1} \\ &+ \delta_{n+1,n'}\delta_{n,n_0} + \delta_{n,n'+1}\delta_{n',n_0}).\end{aligned} \tag{4.21}$$

In momentum representation, the matrix X has elements

$$X_{ll'} = \mathcal{A}_l\delta_{ll'} - i(\delta U/2\gamma)\sigma_y\frac{v_l^* v_{l'}}{4\cos^2(k_l/2)}, \tag{4.22}$$

where we have defined

$$\mathcal{A}_l = i\sigma_z\tan(k_l/2) + (E/2\gamma)\sigma_x - i(U_0/2\gamma)\sigma_y, \tag{4.23}$$

$$v_l = N^{-1/2}e^{in_0k_l}(1 + e^{ik_l}). \tag{4.24}$$

The dispersion relation of the staggered fermions is $\tan^2(k/2) = A(k, k_l)^2$, with

$$A(k, k_l)^2 = (E/2\gamma)^2 - \tan^2(k_l/2) - (U_0/2\gamma)^2. \tag{4.25}$$

An eigenstate at energy E and longitudinal wavevector k is an eigenstate of X with eigenvalue $-\tan(k/2)$. The determinantal equation $\mathrm{Det}[X + \tan(k/2)] = 0$ can again be simplified using Sylvester's theorem. The result, analogous to Eq. (4.15), is

$$\begin{aligned}0 &= \mathrm{Det}\left(1 - \frac{\delta U}{2\gamma}i\sigma_y\frac{1}{N}\sum_l\frac{1}{\mathcal{A}_l + \tan(k/2)}\right) \\ &= \mathrm{Det}\left(1 - \frac{\delta U}{2\gamma}i\sigma_y\frac{1}{N}\sum_l\frac{\mathcal{A}_l - \tan(k/2)}{A(k, k_l)^2 - \tan^2(k/2)}\right).\end{aligned} \tag{4.26}$$

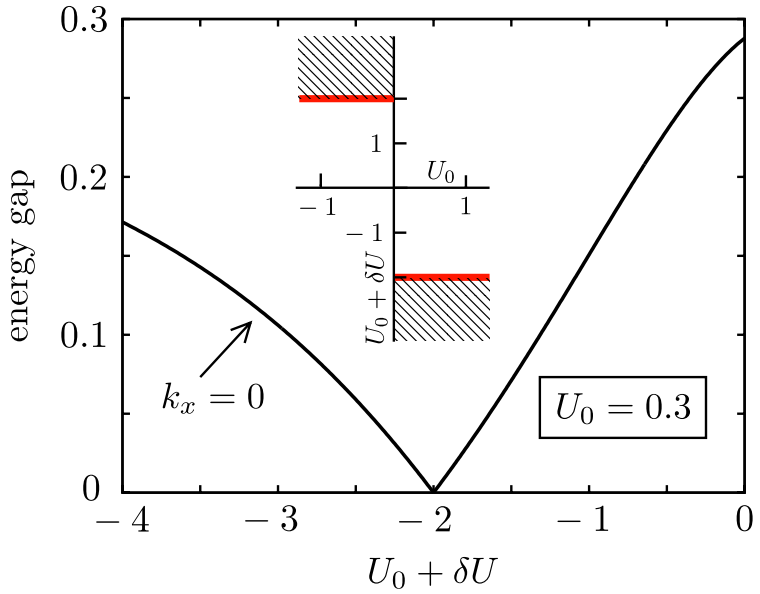

Figure 4.6. Main plot: Closing and reopening of the excitation gap in the staggered fermion model. The MS states exist for defect potentials in the shaded regions in the inset. (All energies are in units of γ.)

Because of the pole in the dispersion relation at $k = \pi$, the zero-mode now exists only at $k = 0$. The condition for this zero-mode, analogous to Eq. (4.16), is

$$\frac{1}{N} \sum_l \frac{U_0/2\gamma}{(U_0/2\gamma)^2 + \tan^2(k_l/2)} = -\frac{2\gamma}{\delta U}, \tag{4.27}$$

For $N \to \infty$ we may again transform the sum into an integral, and thus obtain the critical potential

$$\delta U = \begin{cases} -U_0 - 2\gamma & \text{if } U_0 > 0, \\ -U_0 + 2\gamma & \text{if } U_0 < 0. \end{cases} \tag{4.28}$$

Upon varying the potential $U_0 + \delta U$ of the line defect, at fixed bulk potential U_0, the closing and reopening of the gap thus happens at $U_0 + \delta U = -2\gamma\,\mathrm{sign}\,(U_0)$ (see Fig. 4.6). The inset shows the region in parameter space where the Majorana-Shockley states exist in the staggered fermion model. This phase diagram is much simpler than the corresponding phase diagram for Wilson fermions (Fig. 4.2, inset), because of the absence of

the extra parameter β (which quantifies the strength of the p^2 term in the Wilson fermion model).

Appendix 4.B Self-consistent determination of the pair potential

In order to determine the pair potential self-consistently in a spatially non-homogeneous situation, it is necessary to allow for a position-dependent, anisotropic pair potential $\boldsymbol{\Delta}(\boldsymbol{r}) = (\Delta_x(\boldsymbol{r}), \Delta_y(\boldsymbol{r}))$. The Hamiltonian then reads [44]

$$\begin{aligned} H =& \tfrac{1}{2} \{\Delta_x(\boldsymbol{r}), p_x\} \sigma_x + \tfrac{1}{2} \{\Delta_y(\boldsymbol{r}), p_y\} \sigma_y \\ &+ \big(U(\boldsymbol{r}) + p^2/2m\big)\sigma_z, \end{aligned} \tag{4.29}$$

where $\{\cdot, \cdot\}$ denotes the anticommutator. In the discretization of this Hamiltonian on a square lattice, the spatial dependence of $\boldsymbol{\Delta}(\boldsymbol{r})$ is taken into account in the hopping between neighbors as an average value of $\boldsymbol{\Delta}(\boldsymbol{r})$ on the two lattice points.

When the pair potential is homogeneous, the lattice Hamiltonian has the spectrum

$$\begin{aligned} E^2 = & [U_0 + 2\beta(2 - \cos ak_x - \cos ak_y)]^2 \\ &+ \gamma_x^2 \sin^2 ak_x + \gamma_y^2 \sin^2 ak_y \end{aligned} \tag{4.30}$$

with $\gamma_x = \hbar\Delta_x/a$, $\gamma_y = \hbar\Delta_y/a$ and $\beta = \hbar^2/2ma^2$.

The Hamiltonian must be solved self-consistently together with the equation for the pair potential. These read [44] (with derivatives discretized on the lattice)

$$\begin{aligned} \gamma_x(\boldsymbol{r}) = & -ig \sum_{E_n>0} \left(u_n(x+a,y) - u_n(x-a,y)\right) v_n^*(x,y) \\ & - u_n(x,y) \left(v_n^*(x+a,y) - v_n^*(x-a,y)\right), \\ \gamma_y(\boldsymbol{r}) = & \; g \sum_{E_n>0} \left(u_n(x,y+a) - u_n(x,y+a)\right) v_n^*(x,y) \\ & - u_n(x,y) \left(v_n^*(x,y+a) - v_n^*(x,y+a)\right). \end{aligned} \tag{4.31}$$

Here u_n and v_n are the electron and hole component of the wave function, respectively, and assumed to be from the tight-binding model, i.e. they

are dimensionless and represent the probability amplitude per lattice point (x, y).

The coupling constant g must be chosen such that it gives the correct pair potential γ in the bulk. It can be calculated as

$$\begin{aligned}\frac{\gamma}{g} =& \frac{1}{\pi^2}\int_{-\pi}^{\pi} d(ak_x)\int_{-\pi}^{\pi} d(ak_y)\,\sin(ak_x)\,u(\boldsymbol{k})v^*(\boldsymbol{k}) \\ =& \frac{-i}{\pi^2}\int_{-\pi}^{\pi} d(ak_x)\int_{-\pi}^{\pi} d(ak_y)\,\sin(ak_y)\,u(\boldsymbol{k})v^*(\boldsymbol{k}),\end{aligned} \tag{4.32}$$

where $u(\boldsymbol{k})$ and $v(\boldsymbol{k})$ are the electron and hole coefficients of the plane wave solutions of the bulk lattice Hamiltonian with $E > 0$.

In the particular case of a system that is translationally invariant in x-direction, as is the case for an infinitely extended line defect, the gap equations can be written as:

$$\begin{aligned}\gamma_x(\boldsymbol{r}) &= \frac{4g}{N_x}\sum_{E_n>0,k_x} u_n(k_x, y)v_n^*(k_x, y)\,\sin(ak_x) \\ \gamma_y(\boldsymbol{r}) &= \frac{g}{N_x}\sum_{E_n>0,k_x} \\ &\quad\Big(\left(u_n(k_x, y+a) - u_n(k_x, y+a)\right)v_n^*(k_x, y) \\ &\quad - u_n(k_x, y)\left(v_n^*(k_x, y+a) - v_n^*(k_x, y+a)\right)\Big),\end{aligned} \tag{4.33}$$

summing over N_x longitudinal momenta k_x, and solving the tight-binding problem for each k_x individually.

The self-consistent solution of the tight-binding Hamiltonian and the gap equation (4.33) is obtained in an iterative procedure. In the iteration, we neglect the influence of the vector potential arising from local currents [44] as those effects are expected to be minor for the examples considered in this work. Furthermore, we also avoid adjusting the chemical potential U_0 to obtain a fixed number of electrons in the system and instead use a large unit cell so that the bulk value of $\boldsymbol{\Delta}$ is recovered away from the defect.

Appendix 4.C Line defect in the continuum limit

We calculate the closing and reopening of the excitation gap upon introduction of a line defect in the Hamiltonian (4.1), which is the continuum

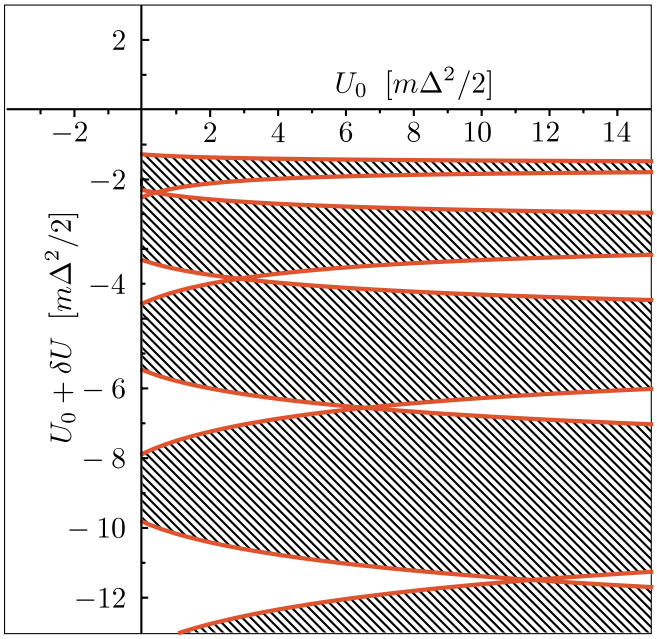

Figure 4.7. The red solid curves are the solution of Eq. (4.38) for $W = 4\hbar/m\Delta$. The MS states exist in the shaded regions.

limit ($a \to 0$) of the Wilson fermion lattice model of App. 4.A.1. The mode matching calculation presented here is the one-dimensional version of the two-dimensional calculation in Refs. [73, 72, 74].

The line defect, of width W, is formed by the electrostatic potential profile

$$U(\boldsymbol{r}) = \begin{cases} U_0 & \text{if } |y| > W/2, \\ U_0 + \delta U & \text{if } |y| < W/2. \end{cases} \tag{4.34}$$

A zero-mode $\psi = (u, v)$ is a (doubly degenerate) eigenstate of the Hamiltonian (4.1) at $E = 0$, $p_x = 0$. The zero-mode should thus satisfy

$$(U + p_y^2/2m)u = i\Delta p_y v, \tag{4.35a}$$
$$(U + p_y^2/2m)v = i\Delta p_y u. \tag{4.35b}$$

For uniform U the solution is a plane wave,

$$\psi_{ss'} = e^{ik_{ss'}y} \begin{pmatrix} 1 \\ s \end{pmatrix}, \quad s, s' = \pm 1, \tag{4.36}$$

with transverse wave vector

$$k_{ss'} = (m/\hbar)\big(is\Delta + s'\sqrt{-\Delta^2 - 2U/m}\big). \tag{4.37}$$

In the region $|y| < W/2$ the zero-mode ψ is a superposition of the four states $\psi_{++}, \psi_{+-}, \psi_{-+}, \psi_{--}$. For $y > W/2$ two decaying states with $\mathrm{Im}\, k_{ss'} > 0$ appear in the superposition, while for $y < -W/2$ the other two states with $\mathrm{Im}\, k_{ss'} < 0$ appear. In total ψ has eight unknown coefficients, which we determine by demanding continuity of ψ and $d\psi/dy$ at $y = W/2$ and $y = -W/2$. The determinant of this set of equations should vanish, in order to have a nontrivial solution. There is only a zero-mode for $U_0 > 0$, $U_0 + \delta U < -m\Delta^2/2$, determined by

$$\tan qW = \frac{2qq_0}{q^2 - q_0^2}. \tag{4.38}$$

We have defined

$$q = (m/\hbar)\sqrt{-\Delta^2 - (2/m)(U_0 + \delta U)}, \tag{4.39}$$

$$q_0 = (m/\hbar)\sqrt{\Delta^2 + 2U_0/m}. \tag{4.40}$$

The MS states exist in between subsequent gap closings, as indicated in Fig. 4.7 (shaded regions).

Chapter 5

Effects of disorder on the transmission of nodal fermions through a d-wave superconductor

5.1 Introduction

As pointed out by Lee in an influential paper [70], disorder has two competing effects on the microwave conductivity of a layered superconductor with d-wave symmetry of the pair potential. On the one hand, disorder increases the density of low-energy quasiparticle excitations, located in the Brillouin zone near the intersection of the Fermi surface with the nodal lines of vanishing excitation gap. On the other hand, disorder reduces the mobility of these nodal fermions. For short-range scattering the two effects cancel [40], producing a disorder independent microwave conductivity $\sigma_0 \simeq (e^2/h)k_F\xi_0$ per layer in the low-temperature, low-frequency limit (with ξ_0 the coherence length and k_F the Fermi wave vector). For long-range scattering the first of the two effects wins [34, 90], which explains the conductivity enhancement measured in the high-T_c cuprates [71, 49] (where long-range scattering dominates [32]).

The microwave conductivity is a bulk property of an unbounded system, of length L and width W large compared to the mean free path l. A finite system makes it possible to study the crossover from diffusive to ballistic transport, as L and W become smaller than l. We have recently

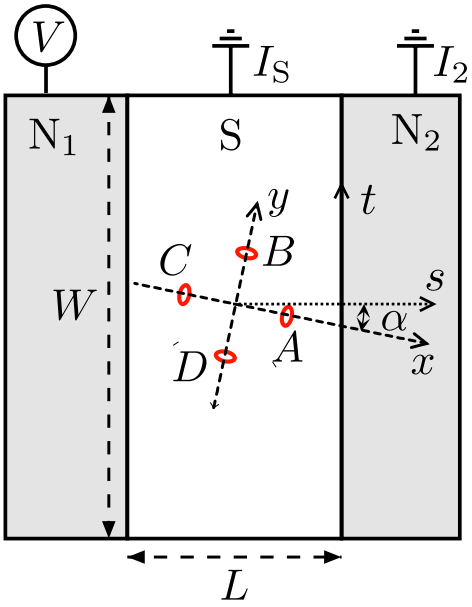

Figure 5.1. Geometry to measure the transmission of quasiparticles at the nodes (red circles) of the pair potential with d_{xy} symmetry.

shown [9] that the transmission of nodal fermions over a length L in the range $\xi_0 \ll L \ll l, W$ is pseudodiffusive: The transmission probability has the W/L scaling of a diffusive system, even in the absence of any disorder. The corresponding conductance G_0 is close the value $(W/L)\sigma_0$ which one would expect from the microwave conductivity, up to a small correction of order $(k_F\xi_0)^{-2} \ll 1$.

It is the purpose of this Chapter to investigate the effects of disorder on the pseudodiffusive conductance, as L becomes larger than l. We find a qualitatively different behavior than for the microwave conductivity, with an exponentially suppressed conductance in the case of short-range scattering and an unaffected conductance $G \simeq G_0$ for long-range scattering.

5.2 Formulation of the problem

The geometry to measure the transmission of nodal fermions is illustrated in Fig. 5.1. It consists of a superconducting strip S between two normal metal contacts N_1 and N_2. The transverse width W of the superconductor is assumed to be large compare to the separation L of the NS interfaces, in

order to avoid edge effects. Contact N_1 is at an elevated voltage V, while S and N_2 are both grounded. The current I_2 through contact N_2 measures the transmitted charge, which is carried entirely by nodal fermions if $L \gg \xi_0$. The nodal lines are the x and y axes, oriented at an angle α relative to the normal to the NS interfaces. There are four nodal points A, B, C, D in the Brillouin zone, at the intersection of the nodal lines and the Fermi surface. The nodal fermions have an anisotropic dispersion relation, with a velocity v_F parallel to the nodal axis and a much smaller velocity $v_\Delta = v_F/k_F\xi_0$ perpendicular to the nodal axis.

The (three-terminal) conductance $G = I_2/V$ was calculated in Ref. 9 in the clean limit $L \ll l$, with the result (per layer)

$$G_{\rm clean} = \frac{2e^2}{h}\frac{W}{L}\frac{v_F^2+v_\Delta^2}{\pi v_F v_\Delta}\frac{\Gamma_1\Gamma_2}{(2-\Gamma_1)(2-\Gamma_2)}, \tag{5.1}$$

independent of α. The factors $\Gamma_1, \Gamma_2 \in (0,1)$ are the (mode-independent) transmission probabilities of tunnel barriers at the N_1S and N_2S interfaces. We have assumed that the tunnel barriers do not couple the nodes, which requires $\alpha \gg \xi_0/L$ and $\pi/4 - \alpha \gg \xi_0/L$. Since $\xi_0/L \ll 1$, this is the generic case.

We now wish to move away from the clean limit and include scattering by electrostatic potential fluctuations. We distinguish two regimes, depending on the magnitude of the correlation length l_c of the potential fluctuations. In the regime $k_F l_c \gg 1$ of long-range disorder, the nodes remain uncoupled and can be treated separately. We consider this regime of *intranode* scattering first, and then include the effects of *internode* scattering when l_c becomes smaller than $1/k_F$.

5.3 Intranode scattering regime

In the absence of internode scattering, the electron and hole components of the wave function $\Psi = (\Psi_e, \Psi_h)$ of nodal fermions (at excitation energy ε) are governed by the anisotropic Dirac equation $H\Psi = \varepsilon\Psi$. Near node A the Hamiltonian takes the form [5]

$$H = -i\hbar(v_F\sigma_z\partial_x + v_\Delta\sigma_x\partial_y) + V_\mu\sigma_z + V_\Delta\sigma_x. \tag{5.2}$$

The two terms $V_\mu(x,y)$ and $V_\Delta(x,y)$ describe, respectively, long-range disorder in the electrostatic potential and in the s-wave component of

the pair potential. These two types of disorder preserve time-reversal symmetry. The Hamiltonian anti-commutes with the Pauli matrix σ_y, belonging to the chiral symmetry class AIII of Ref. 5.

Following Refs. 108, 117, at zero energy, the disorder potentials can be transformed out from the Dirac equation by means of the transformation $\Psi \mapsto \exp(i\phi + \chi\sigma_y)\Psi_0$, with fields ϕ and χ determined by

$$v_F\partial_x\phi + v_\Delta\partial_y\chi = -V_\mu/\hbar, \tag{5.3a}$$
$$v_F\partial_x\chi - v_\Delta\partial_y\phi = V_\Delta/\hbar. \tag{5.3b}$$

If $H\Psi = 0$ then also $H_0\Psi_0 = 0$, where H_0 is the Dirac Hamiltonian without disorder ($V_\mu \equiv 0$ and $V_\Delta \equiv 0$).

The transformation from Ψ to Ψ_0 leaves the particle current density unaffected but not the electrical current density: The particle current density $\mathbf{j}$ reads

$$(j_x, j_y) = \Psi^\dagger(v_F\sigma_z, v_\Delta\sigma_x)\Psi = \Psi_0^\dagger(v_F\sigma_z, v_\Delta\sigma_x)\Psi_0, \tag{5.4}$$

while for the electrical current density $\mathbf{i}$ one has

$$i_y = 0, \quad i_x = ev_F\Psi^\dagger\Psi = ev_F\Psi_0^\dagger\exp(2\chi\sigma_y)\Psi_0. \tag{5.5}$$

This is consistent with the findings of Durst and Lee [34], that the low-energy effects of intranode scattering on the density-of-states and on the mobility cancel for the thermal conductivity (proportional to the particle current) but not for the electrical conductivity (which is increased by disorder).

As we now show, for the conductance of a finite system, the effect of intranode scattering is entirely different. Following Ref. [9], the conductance is determined by the transfer matrix $\mathcal{M}$ relating right-moving and left-moving states $\Phi_1 = (\Phi_1^+, \Phi_1^-)$ in N_1 to right-moving and left-moving states $\Phi_2 = (\Phi_2^+, \Phi_2^-)$ in N_2. It is convenient to rotate the coordinate system from x and y along the nodal axes to coordinates s and t perpendicular and parallel to the NS interfaces. The transfer matrix is defined by

$$\Phi_2(L,t) = \int dt'\,\mathcal{M}(t,t')\Phi_1(0,t'). \tag{5.6}$$

For wave vectors in the normal metal coupled to node A, the right-movers are electrons Φ_e^+ and the left-movers are holes Φ_h^-, so an electron incident from contact N_1 can only be transmitted into contact N_2 as an electron,

not as a hole. The corresponding transmission matrix t_{ee} is determined by the transfer matrix via

$$t_{ee} = \left(\mathcal{M}_{11}^{\dagger}\right)^{-1}, \quad \mathcal{M} = \begin{pmatrix} \mathcal{M}_{11} & \mathcal{M}_{12} \\ \mathcal{M}_{21} & \mathcal{M}_{22} \end{pmatrix}. \tag{5.7}$$

The contribution G_A to the electrical conductance from node A then follows from

$$G_A = \frac{2e^2}{h} \mathrm{Tr}\, t_{ee} t_{ee}^{\dagger}, \tag{5.8}$$

with a factor of two to account for both spin directions. The full conductance contains an additional contribution from node B, determined by similar expressions with α replaced by $\alpha - \pi/2$.

The Hamiltonian (5.2) does not apply within a coherence length ξ_0 from the NS interfaces, where the depletion of the pair potential should be taken into account. We assume weak disorder, $l \gg \xi_0$, so that we can use the clean-limit results of Ref. [9] in this interface region. For simplicity, we do not include tunnel barriers at this stage ($\Gamma_1 = \Gamma_2 = 1$). The transfer matrix through the superconductor is then given by

$$\begin{aligned} \mathcal{M} = {} & \exp(i\phi_{\mathrm{R}} + \sigma_y \chi_{\mathrm{R}}) \exp(-iLv_F v_\Delta v_\alpha^{-2} \sigma_y \partial_t + L\varphi_\alpha \partial_t) \\ & \times \exp(-i\phi_{\mathrm{L}} - \sigma_y \chi_{\mathrm{L}}), \end{aligned} \tag{5.9}$$

with the abbreviations

$$v_\alpha = \sqrt{v_F^2 \cos^2\alpha + v_\Delta^2 \sin^2\alpha}, \tag{5.10}$$

$$\varphi_\alpha = \tfrac{1}{2} v_\alpha^{-2} (v_F^2 - v_\Delta^2) \sin 2\alpha. \tag{5.11}$$

The fields $\phi_{\mathrm{L}}(t), \chi_{\mathrm{L}}(t)$ are evaluated at the left NS interface ($s = 0$) and the fields $\phi_{\mathrm{R}}(t), \chi_{\mathrm{R}}(t)$ are evaluated at the right NS interface ($s = L$).

We now follow Ref. [108] and use the freedom to impose boundary conditions on the solution of Eq. (5.3). Demanding $\chi = 0$ on the NS interfaces fixes both χ and ϕ (up to an additive constant). The transfer matrix (5.9) then only depends on the disorder through the terms $\exp(i\phi_{\mathrm{R}})$ and $\exp(-i\phi_{\mathrm{L}})$, which are unitary transformations and therefore drop out of the conductance (5.8). We conclude that the electrical conductance (5.1) is not affected by long-range disorder.

Tunnel barriers affect the conductance in two distinct ways. Firstly, at both NS interfaces, we need to consider all four states $\Phi_{e,h}^{\pm}$ that have the same component of the wave vector parallel to the NS interface (Φ_e^+, Φ_h^-

have the opposite perpendicular component than Φ_e^-, Φ_h^+). However, only one right-moving and one left-moving superposition of these modes, $\Phi_n^\pm$, is coupled by the transfer matrix to the other side of the system:

$$\Phi_n^+ = (2-\Gamma_n)^{-1/2}\big[\Phi_e^+ + (1-\Gamma_n)^{1/2}\Phi_h^+\big], \tag{5.12a}$$

$$\Phi_n^- = (2-\Gamma_n)^{-1/2}\big[(1-\Gamma_n)^{1/2}\Phi_e^- + \Phi_h^-\big]. \tag{5.12b}$$

The superposition of incoming electron and hole states orthogonal to Φ_n^+ is fully reflected by the tunnel barrier and the superconductor, and so plays no role in the conductance. For a detailed derivation of these formulas see Appendix 5.A.

Secondly, the modes Φ_n^+ are only partially transmitted through the barriers. We have calculated the transmission probability (see Appendix 5.A for details), and found that it can be accounted for by the following transformation of the transfer matrix,

$$\mathcal{M} \mapsto e^{\gamma_2\sigma_y}\mathcal{M}e^{\gamma_1\sigma_y}, \quad \gamma_n = \tfrac{1}{2}\ln\big(2/\Gamma_n - 1\big). \tag{5.13}$$

With tunnel barriers, the transmission matrix contains mixed electron and hole elements,

$$\mathcal{T} = \begin{pmatrix} t_{ee} & t_{eh} \\ t_{he} & t_{hh} \end{pmatrix} = U_2^\dagger \begin{pmatrix} (\mathcal{M}_{11}^\dagger)^{-1} & 0 \\ 0 & 0 \end{pmatrix} U_1, \tag{5.14}$$

where the unitary matrices U_n transform from the electron-hole basis to the basis state Φ_n^+ and its (fully reflected) orthogonal complement,

$$U_n = (2-\Gamma_n)^{-1/2}\begin{pmatrix} 1 & (1-\Gamma_n)^{1/2} \\ (1-\Gamma_n)^{1/2} & -1 \end{pmatrix}. \tag{5.15}$$

Finally, the contribution G_A to the electrical conductance from node A follows from

$$G_A = \frac{2e^2}{h}\mathrm{Tr}\left(t_{ee}t_{ee}^\dagger - t_{he}t_{he}^\dagger\right). \tag{5.16}$$

With tunnel barriers, not just nodes A and B, but nodes C and D also contribute to the full conductance.

Collecting results, we substitute Eq. (5.9) (with χ_L and χ_R both fixed at zero) into Eq. (5.13) to obtain the transfer matrix, and then substitute the $1,1$ block into Eq. (5.14) for the transmission matrix. Disorder only enters through the factors $\exp(i\phi_\mathrm{R})$ and $\exp(-i\phi_\mathrm{L})$, which mix the modes

on the superconducting side of the tunnel barriers. Since the tunnel probabilities are assumed to be mode independent, these factors commute with the U_n's and cancel upon taking the trace in Eq. (5.16). We thus recover the clean-limit result (5.1), independent of any disorder potential. Disorder would have an effect on the conductance for mode-dependent tunnel probabilities, but since the modes in the normal metal couple to a narrow range of transverse wave vectors in the superconductor, the assumption of mode-independence is well justified.

As an aside we mention that the thermal (rather than electrical) conductance $G_{\text{thermal}} \propto \text{Tr}\, \mathcal{T}\mathcal{T}^\dagger$ would be independent of disorder also for the case of mode-dependent tunnel probabilities, since the U_n's drop out of the trace. The tunnel barriers would then still enter in the transfer matrix through the terms $e^{\gamma_n \sigma_y}$ in Eq. (5.13), but these terms have the same effect as delta function contributions to V_μ and can therefore be removed by including them in Eq. (5.3). The conclusion is that the thermal conductance is independent of both disorder and tunnel barriers, while the electrical conductance is independent of disorder but dependent on tunnel barriers through the factors $\Gamma_n/(2-\Gamma_n)$. Notice that the Wiedemann-Franz relation between thermal and electrical conductance does not apply.

5.4 Effect of internode scattering

So far we have only considered intranode scattering. For short-range disorder we have to include also the effects of internode scattering. Internode scattering suppresses the electrical conductance, measured between the normal metals N_1 and N_2, because an electron injected from N_1 into nodes A or B and then scattered to nodes C or D will exit into N_2 as a hole, of opposite electrical charge. (The charge deficit is drained to ground via the superconductor.) The thermal conductance, in contrast, remains unaffected by internode scattering because electrons and holes transport the same amount of energy. (Again, the Wiedemann-Franz relation does not apply.)

We first give a semiclassical analytical theory, and then a fully quantum mechanical numerical treatment.

5.4.1 Semiclassical theory

We assume that the mean free path l for intranode scattering is short compared to the internode scattering length. Semiclassically we may then

describe the internode scattering by a (stationary) reaction-diffusion equation for the carrier densities n_ν,

$$\boldsymbol{\nabla}\cdot\boldsymbol{D}_\nu\cdot\boldsymbol{\nabla}n_\nu+\sum_{\nu'\neq\nu}\bigl(\gamma_{\nu\nu'}n_{\nu'}-\gamma_{\nu'\nu}n_\nu\bigr)=0. \tag{5.17}$$

The labels $\nu,\nu'\in\{A,B,C,D\}$ indicate the nodes, with diffusion tensor $\boldsymbol{D}_\nu$ and scattering rate $\gamma_{\nu\nu'}$ from ν' to ν. For simplicity we assume there is no tunnel barrier at the NS interfaces, and seek a solution $n_\nu(s)$ with boundary conditions

$$n_\nu(0)=\frac{1}{2}(\delta_{\nu,A}+\delta_{\nu,B})eV\rho_F,\quad n_\nu(L)=0. \tag{5.18}$$

Here ρ_F is the density of states per node at the Fermi energy, and we have chosen the sign of the applied voltage V such that electrons (rather than holes) are injected into the superconductor from N_1.

The diffusion tensor is diagonal in the $x-y$ basis, with components D_μ and D_Δ in the direction of v_μ and v_Δ, respectively. The average diffusion constant is $\bar{D}=\frac{1}{2}(D_\mu+D_\Delta)$ and we also define $D_\alpha=D_\mu\cos^2\alpha+D_\Delta\sin^2\alpha$. We distinguish internode scattering between opposite nodes, with rate γ_1, and between adjacent nodes, with rate γ_2. Because the solution $n_\nu(s)$ in the $s-t$ basis is independent of the transverse coordinate t, we may replace the Laplacian $\boldsymbol{\nabla}\cdot\boldsymbol{D}_\nu\cdot\boldsymbol{\nabla}\mapsto D_\nu d^2/ds^2$ with $D_A=D_C=D_\alpha$ and $D_B=D_D=2\bar{D}-D_\alpha$.

We seek the current into N_2, given by

$$I_2=-eW\lim_{s\to L}\frac{d}{ds}\bigl[D_An_A+D_Bn_B-D_Cn_C-D_Dn_D\bigr]. \tag{5.19}$$

This can be obtained by integrating the reaction-diffusion equation (5.17) in the way explained in Ref. 114. The result is

$$I_2=e^2V\rho_FW\frac{1}{2}\biggl[\frac{\sqrt{2(\gamma_1+\gamma_2)D_\alpha}}{\sinh\sqrt{2L^2(\gamma_1+\gamma_2)/D_\alpha}}+\frac{\sqrt{2(\gamma_1+\gamma_2)(2\bar{D}-D_\alpha)}}{\sinh\sqrt{2L^2(\gamma_1+\gamma_2)/(2\bar{D}-D_\alpha)}}\biggr]. \tag{5.20}$$

In the small-L limit (when intervalley scattering can be neglected) we recover an α-independent conductance $I_2/V\to e^2\rho_F\bar{D}W/L$, consistent with

the expected result (5.1). For large L the conductance decays exponentially $\propto e^{-L/l_{\rm inter}}$, with

$$l_{\rm inter} = \sqrt{\tfrac{1}{2}\min(D_\alpha, 2\bar{D} - D_\alpha)/(\gamma_1 + \gamma_2)} \tag{5.21}$$

the internode scattering length. For weak disorder ($k_F l \gg 1$) this decay length is much shorter than the Anderson localization length $\simeq l e^{k_F l}$, so we are justified in treating the transport semiclassically by a diffusion equation.

5.4.2 Fully quantum mechanical solution

The Hamiltonian in the presence of internode scattering belongs to symmetry class CI of Ref. [5], restricted by time-reversal symmetry and electron-hole symmetry — but without the chiral symmetry that exists in the absence of internode scattering.

To write the Hamiltonian $\mathcal{H}$ of the four coupled nodes in a compact form we use three sets of Pauli matrices: For each $i = x, y, z$ the 2×2 Pauli matrix σ_i couples electrons and holes, γ_i couples opposite nodes (A to C and B to D), and τ_i couples adjacent nodes (A to B and C to D). The requirements of time-reversal symmetry and electron-hole symmetry are given, respectively, by

$$\gamma_x \mathcal{H}^* \gamma_x = \mathcal{H}, \quad (\gamma_x \otimes \sigma_y)\mathcal{H}^*(\gamma_x \otimes \sigma_y) = -\mathcal{H}. \tag{5.22}$$

In the absence of disorder, the Hamiltonian is given by

$$\begin{aligned}\mathcal{H}_{\rm clean} = {} & p_x \left(v_F \tau_+ \otimes \sigma_z + v_\Delta \tau_- \otimes \sigma_x\right) \otimes \gamma_z \\ & + p_y \left(v_F \tau_- \otimes \sigma_z + v_\Delta \tau_+ \otimes \sigma_x\right) \otimes \gamma_z.\end{aligned} \tag{5.23}$$

The momentum operator is $\boldsymbol{p} = -i\hbar\partial/\partial\boldsymbol{r}$ and we have defined $\tau_\pm = \frac{1}{2}(\tau_0 \pm \tau_z)$, with τ_0 the 2×2 unit matrix.

Since the effects of disorder in the electrostatic potential $V_\mu(\boldsymbol{r})$ and in the pair potential $V_\Delta(\boldsymbol{r})$ are equivalent [5], we restrict ourselves to the former. The relevant Fourier components of $V_\mu(\boldsymbol{r})$ can be represented by the expansion

$$\begin{aligned}V_\mu(\boldsymbol{r}) = {} & \mu_0(\boldsymbol{r}) \\ & + \mu_1(\boldsymbol{r}) e^{i(\boldsymbol{k}_C - \boldsymbol{k}_A)\cdot\boldsymbol{r}} + \mu_2(\boldsymbol{r}) e^{i(\boldsymbol{k}_D - \boldsymbol{k}_B)\cdot\boldsymbol{r}} \\ & + \mu_3(\boldsymbol{r}) e^{i(\boldsymbol{k}_B - \boldsymbol{k}_A)\cdot\boldsymbol{r}} + \mu_4(\boldsymbol{r}) e^{i(\boldsymbol{k}_C - \boldsymbol{k}_B)\cdot\boldsymbol{r}},\end{aligned} \tag{5.24}$$

where $\boldsymbol{k}_X$ is the wave vector of node $X = A, B, C, D$ (see Fig. 5.1). The Fourier amplitudes $\mu_p(\boldsymbol{r})$ are all slowly varying functions of $\boldsymbol{r}$, with correlation length $\xi \gg 1/k_F$. The amplitude μ_0 is responsible for intranode scattering, arising from spatial Fourier components of $V(\boldsymbol{r})$ with wave vector $\ll k_F$ (long-range scattering). The other four amplitudes arise from Fourier components with wave vector $\gtrsim k_F$ (short-range scattering). Of these internode scattering potentials, μ_1, μ_2 scatter between opposite nodes and μ_3, μ_4 scatter between adjacent nodes.

The Hamiltonian $\mathcal{H} = \mathcal{H}_{\rm clean} + \mathcal{H}_{\rm disorder}$ contains an electrostatic disorder contribution $\mathcal{H}_{\rm disorder} \propto \sigma_z$. Six combinations of Pauli matrices are allowed by the symmetry (5.22), five of which have independent amplitudes:

$$\mathcal{H}_{\rm disorder} = \sum_{n=0}^{4} \mathcal{H}_p \otimes \sigma_z, \quad \text{with} \tag{5.25}$$

$$\begin{aligned} \mathcal{H}_0 &= \mu_0(\boldsymbol{r})\left[\tau_+ \otimes \gamma_0 + \tau_- \otimes \gamma_0\right] = \mu_0(\boldsymbol{r})\tau_0 \otimes \gamma_0, \\ \mathcal{H}_1 &= \mu_1(\boldsymbol{r})\tau_+ \otimes \gamma_x, \quad \mathcal{H}_2 = \mu_2(\boldsymbol{r})\tau_- \otimes \gamma_x, \\ \mathcal{H}_3 &= \mu_3(\boldsymbol{r})\tau_x \otimes \gamma_0, \quad \mathcal{H}_4 = \mu_4(\boldsymbol{r})\tau_x \otimes \gamma_x. \end{aligned} \tag{5.26}$$

We have solved the quantum mechanical scattering problem of the four coupled Dirac Hamiltonians numerically, by discretizing $\mathcal{H}$ on a grid. Since the electrostatic potential appears in the form of a vector potential in the Dirac Hamiltonian, in our numerical discretization we are faced with a notorious problem from the theory of lattice fermions: How to avoid fermion doubling while preserving gauge invariance [113]. The transfer matrix discretization method we use, from Ref. [11], satisfies gauge invariance only in the continuum limit. We ensure that we have reached that limit, by reducing the mesh size of the grid until the results have converged.

We fixed the width of the d-wave strip at $W = 150\,\xi$, oriented at an angle $\alpha = \pi/8$ with the nodal lines, and increased L at fixed ξ. We set the anisotropy at $v_F/v_\Delta = 2$ and did not include tunnel barriers for simplicity. All five amplitudes $\mu_p(\boldsymbol{r})$ are taken as independently fluctuating Gaussian fields, with the same correlation length ξ. The Gaussian fields have zero ensemble average, $\langle \mu_p(\boldsymbol{r}) \rangle = 0$, and second moment

$$K_p = (\hbar v_F)^{-2} \int d\boldsymbol{r}\, \langle \mu_p(0)\mu_p(\boldsymbol{r}) \rangle. \tag{5.27}$$

We took $K_0 = 1$ and either $K_1 = K_2 = K_3 = K_4 = 0$ (only intranode scattering) or $K_1 = K_2 = K_3 = K_4 = 0.4$ (both intranode and intern-

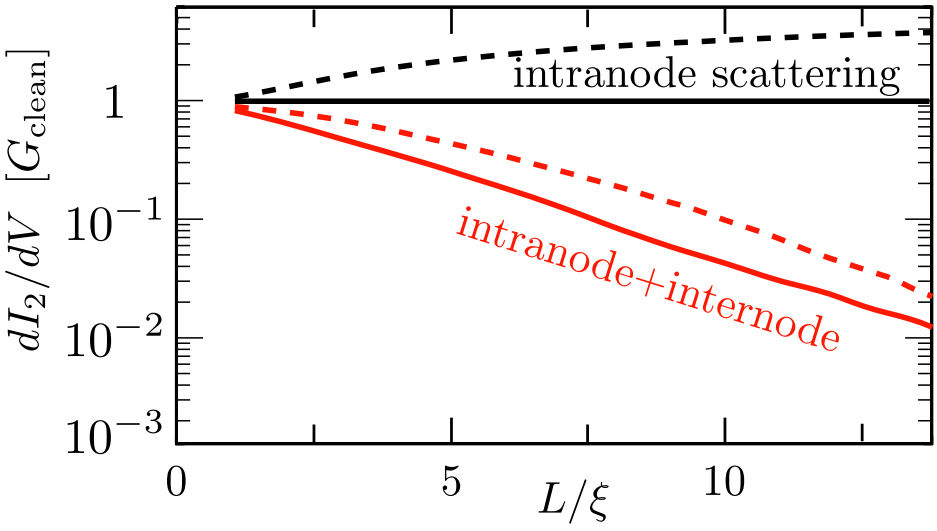

Figure 5.2. Differential conductance as a function of sample length, calculated numerically from the four coupled Dirac Hamiltonians of nodal fermions. The solid curves are at zero voltage and the dashed curves at nonzero voltage. If only intranode scattering is present (upper curves), the differential conductance is close to the value G_{clean} from Eq. (5.1). Including also internode scattering (lower curves) causes the conductance to decay strongly below G_{clean}.

ode scattering). The results in Fig. 5.2 give the differential conductance dI_2/dV, both at zero voltage and at a voltage of $V = 0.2\,\hbar v_F/e\xi$.

Without internode scattering, we recover precisely the analytical result $dI_2/dV = G_{\text{clean}}$ at $V = 0$. At nonzero voltages, dI_2/dV rises above G_{clean} with increasing L, consistent with the expectations [108] for the crossover from pseudo-diffusive to ballistic conduction at $V \simeq \hbar v_F/eL$. Internode scattering causes dI_2/dV to drop strongly below G_{clean} with increasing L, both at zero and at nonzero voltages. The decay is approximately exponential, consistent with our semiclassical theory (although the range accessible numerically is not large enough to accurately extract a decay rate).

5.5 Conclusion

In summary, we have shown that the effect of disorder on the electrical current transmitted through a normal-metal–d-wave-superconductor–normal metal junction is strikingly different depending on the range of the disorder potential: Long-range scattering has no effect, while short-range scattering suppresses the current exponentially. This behavior is dual to what is known [34, 90] for the bulk conductivity, which is unaffected by short-range scattering and increased by long-range scattering. Because of the exponential sensitivity $\propto e^{-L/l_{\text{inter}}}$, we propose the setup of Fig. 5.1 as a way to measure the internode scattering length l_{inter}.

As a direction for future research, it would be interesting to study the transmission in the geometry of Fig. 5.1 of low-energy excitations that are not located near the nodal points of the pair potential. A mechanism for the formation of non-nodal zero-energy states in d-wave superconductors has been studied in Refs. [2, 3].

Appendix 5.A Tunnel barrier at the NS interface

We consider a tunnel barrier between the normal metal contact N_1 and the superconductor. To be specific, we describe the left end of our setup, the derivations for the right contact follow analogously. We introduce an additional normal metal of zero length between the tunnel barrier and the superconductor, as illustrated in Fig. 5.3. For simplicity we assume translation invariance along the NS interface holds: then the energy and the wave number along the NS interface are good quantum numbers. The

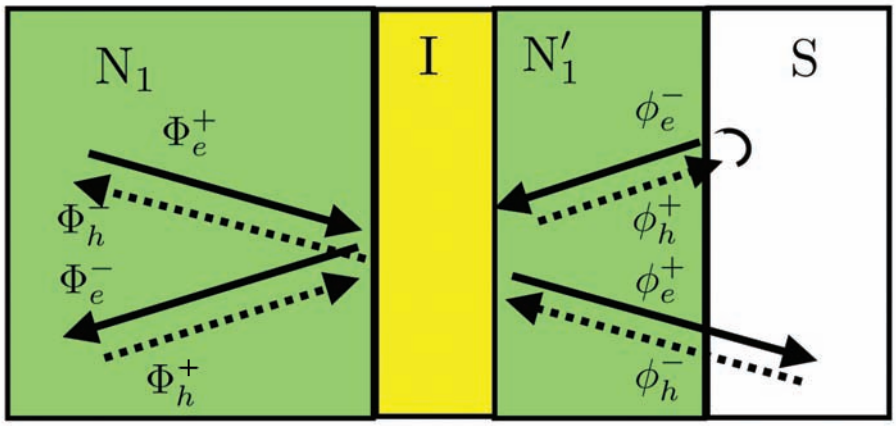

Figure 5.3. Sketch of the normal-superconducting interface, with the plane wave modes taking part in conduction with a fixed energy and transverse momentum. To define the modes $\phi_{e,h}^{+,-}$, a piece of normal metal with length $\to 0$ is inserted between the tunnel barrier I and the superconductor S.

tunnel barrier mixes the 4 modes with these constants in the normal lead N_1: $\Phi_e^{+,-}$ for right-/left-propagating electrons, and Φ_h^{+-} for right-/left-propagating holes, with the 4 modes with these constants in N_1': $\phi_e^{+,-}$ and $\phi_h^{+,-}$. We have

$$\begin{pmatrix} \Phi_e^- \\ \phi_e^+ \\ \Phi_h^- \\ \phi_h^+ \end{pmatrix} = \begin{pmatrix} \mathfrak{r} & \mathfrak{t}' & 0 & 0 \\ \mathfrak{t} & \mathfrak{r}' & 0 & 0 \\ 0 & 0 & \mathfrak{r}^* & \mathfrak{t}'^* \\ 0 & 0 & \mathfrak{t}^* & \mathfrak{r}'^* \end{pmatrix} \begin{pmatrix} \Phi_e^+ \\ \phi_e^- \\ \Phi_h^+ \\ \phi_h^- \end{pmatrix}. \tag{5.28}$$

Here $\mathfrak{t} = \sqrt{\Gamma_1} e^{i\chi}$ and $\mathfrak{t}' = \sqrt{\Gamma_1} e^{i\chi'}$ are the electron transmission amplitudes, $\chi, \chi' \in \mathbb{R}$, and $\mathfrak{r}$ and $\mathfrak{r}'$ are the electron reflection amplitudes.

Since the angle α between the normal to the NS interface and the nodal line is taken to be generic, $0 \ll \alpha \ll -\pi/4$, the modes ϕ_h^+ and ϕ_e^- cannot propagate in the superconductor. They are localized near the NS interface, and follow Andreev reflection: $\phi_e^- = -i\phi_h^+$. Using this, we can write the scattering matrix S representing the combined effect of the tunnel barrier

and the Andreev reflections on the propagating modes as

$$\begin{pmatrix} \Phi_e^- \\ \Phi_h^- \\ \phi_e^+ \end{pmatrix} = S \begin{pmatrix} \Phi_e^+ \\ \Phi_h^+ \\ \phi_h^- \end{pmatrix}; \quad S = \begin{pmatrix} \mathfrak{r} & -\mathfrak{t}'i\mathfrak{t}' & -\mathfrak{t}'i\mathfrak{r}'^* \\ 0 & \mathfrak{r}' & \mathfrak{t}'^* \\ \mathfrak{t} & -\mathfrak{r}'i\mathfrak{t}' & -\mathfrak{r}'i\mathfrak{r}'^* \end{pmatrix} \tag{5.29}$$

Now there are two incoming propagating modes from the left, but only one outgoing propagating mode to the right. This implies that there is a superposition of Φ_e^+ and Φ_h^+ that is reflected with unit probability into a superposition of Φ_e^- and Φ_h^-. Orthogonal to these uncoupled superpositions are the *relevant modes* $\Phi_1^+ = u_e\Phi_e^+ + u_h\Phi_h^+$ and $\Phi_1^- = v_e\Phi_e^- + v_h\Phi_h^-$, which are coupled to the propagating modes in the superconductor. We can find them from Eq. (5.29) by just observing what $S^\dagger$ and S take $(0,0,1)^\dagger$ to:

$$\begin{pmatrix} u_e \\ u_h \end{pmatrix} = \frac{1}{\mathcal{N}} \begin{pmatrix} e^{-i\chi} \\ i\mathfrak{r}'^* e^{i\chi} \end{pmatrix}; \qquad \begin{pmatrix} v_e \\ v_h \end{pmatrix} = \frac{1}{\mathcal{N}} \begin{pmatrix} i\mathfrak{r}'^* e^{i\chi'} \\ e^{-i\chi'} \end{pmatrix}, \tag{5.30}$$

where $\mathcal{N} = \sqrt{2-\Gamma_1}$ is a normalizing factor. For our setup, all phase factors here can be absorbed into the definitions of the plane wave modes in contact N_1, and we obtain Eqs. (5.12).

Acting with S on $(u_e^*, u_h^*, 0)^\dagger$ allows us to infer the transmission and reflection amplitudes of the relevant modes, from which we can obtain the transfer matrix,

$$\begin{pmatrix} \phi_e^+ \\ \phi_h^- \end{pmatrix} = \mathcal{M}_1 \begin{pmatrix} \Phi_1^+ \\ \Phi_1^- \end{pmatrix}; \qquad \mathcal{M}_1 = \frac{1 + (1-\Gamma_1)\sigma_y}{\sqrt{\Gamma_1(2-\Gamma_1)}}. \tag{5.31}$$

This transfer matrix can be written in a succint form with a real parameter γ_1 characterizing the tunnel barrier:

$$\mathcal{M}_1 = \exp[\gamma_1\sigma_y]; \quad \gamma_1 = \frac{1}{2}\ln\frac{2-\Gamma_1}{\Gamma_1}. \tag{5.32}$$

This and the analagous calculation for the right edge of the system lead directly to Eq. (5.13).

Chapter 6

Piezoconductivity of gated suspended graphene

6.1 Introduction

Graphene is a novel material with highly unusual electron properties, related to the Dirac form of its energy spectrum at low energies, and demonstrated in many seminal experiments (for review see [13, 22]). Experiments on single-layer graphene have been performed on the flakes obtained by exfoliation as well as grown on a substrate.

Graphene also has excellent mechanical properties. Indeed, the elastic properties have been measured on suspended graphene flakes mechanically deposited over a hole by indentation in an atomic force microscope [67, 94, 39]; the results showed that graphene is incredibly stiff, with the breaking strength of the order of 40N/m, the Young modulus of 1 TPa, and possibility to be stretched elastically up to 20%. Bending properties have been determined experimentally for several-layer graphene flakes [94] and are not yet available for a monolayer. Theoretically, these properties have been predicted from the calculations using the analytical form of the interatomic potential, and from molecular dynamic studies [52, 51]. Graphene is currently one of the most prospective candidates for high-frequency nanomechanical resonators [21, 25], with the quality factor and eigenfrequency extracted from measurements to be $Q \approx 75$, $f_0 = 70.5$ MHz for a monolayer, and $Q \approx 120$, $f_0 = 42$ MHz for 15nm thick graphite. Quality factor further increases with decreasing temperature. An alternative method to investigate elastic properties of graphene

is to put the film on a flexible substrate and deform the substrate [60, 82]. The strain influences optical phonon spectrum [82], which has been measured by Raman spectroscopy.

Recent experiments combine mechanical and electrical properties of graphene by measuring conductivity [18, 19, 120, 33] of suspended graphene flakes. This is a very promising direction since suspended graphene flakes exhibit much higher mobility than graphene on substrate due to much weaker disorder [18, 19]. Potentially electrons can produce back-action on the resonator. Graphene resonators are expected to have high sensitivity to mass and prebuilt strain [25], so that they can be used to ultra-sensitive mass detection.

Suspension of graphene flakes always leads to their deformation, which in turn affects the conduction properties of graphene. Deformation creates inhomogeneous elongation of the lattice constant [92, 38] which locally affects the electron spectrum of graphene. One way to look at the variations of the band structure of the strained graphene is to perform density functional calculations [99]. Alternatively, the variation of the lattice constant can be represented at the level of Dirac equation in the form of pseudomagnetic fields [115]. Ref. [38] pointed out that local shifts of the Fermi surface in suspended graphene in the vicinity of the Dirac point can block the conductivity — if the Fermi-surfaces at different parts of the flake do not overlap, the conduction is tunnel rather than metallic. Effects of disorder due to charged impurities and midgap states, optical and acoustic phonons were taking into account for calculating conductivity of gated graphene in [112]. For strong enough deformation, graphene quasiparticles can become localized [61].

In experiments, graphene flakes are typically suspended over a backgate. This gate redistributes the electron density in the flake due to the spatial variation of the capacitance. The regions in the center of the suspended part of the flake have higher electron density then the regions near the clamping edges, as the central part is closer to the gate. This density redistribution affects the transmission coefficients through the entire flake. The corresponding effect on the piezoresistivity in ballistic regime is of the first order in the maximum deformation of the flake in the transverse direction, and it increases the conductivity. This has to be contrasted with the effect of the pseudomagnetic fields which suppress the conductivity. The contribution from pseudovector potential depends on the strain [38] over the flake and is of the second order in the maximum deformation. Thus,

this contribution is expected to be weaker than effect from the charge redistribution. We will show however that this effect can be important for graphene under high enough residual stress. Inhomogeneous deformation of graphene yields the corrections to the conductivity which are of the fourth order in the maximum deformation, which is even smaller.

In this Chapter, we calculate the effect of the gate-induced density redistribution on the conductivity of the graphene flake. We find that, indeed, for high residual stress the correction resulting from the pseudovector potential is important, and the correction to the conductivity is negative. We mostly focus on the regime of low residual stress and show that the correction from the charge redistribution becomes the most important.

Experimentally, influence of deformation on the conductivity would be difficult to observe on a suspended graphene flake with one gate since the main effect of the gate is the global shift of the density rather than its redistribution. To separate density redistribution and elastic deformation, one needs to employ two gates. For instance, one can use the configuration with a large bottom gate and a narrow top gate. The bottom gate deforms the graphene flake and determines the maximum transverse deformation ξ_{max}. When voltage is switched on the narrow top gate it does not influence much of deformation of the flake depleting the charge density below the top gate. Since the region under the top gate has the lowest density it determines the conductivity of the whole flake. If this region is brought to the Dirac point, the correction to conductivity is determined only by the deformation of graphene [38] and is proportional to $(\xi_{max}(V_g)/L)^2$, with V_g and L being the voltage applied to the bottom gate and the length of the strip under the top gate. However, for higher voltages the charge redistribution is more important, and the correction to conductivity is proportional to $\xi_{max}(V_g)/d$, d being the distance to the bottom gate. Instead of the top gate, one can use an AFM tip.

The chapter is organized as follows. In Section 6.2 we derive equations for the deformation of suspended graphene from general theory of elasticity. We consider two situations — graphene deformed homogeneously by a gate and graphene deformed locally by an AFM tip. The capacitance between the gate and suspended graphene varies due to deformation of the flake. We calculate the density redistribution over the flake taking into account the shape of the flake. In Section 6.3, we use these results to evaluate correction to the conductivity. We use the perturbation theory to calculate the transmission eigenvalues, and the correction to the conduc-

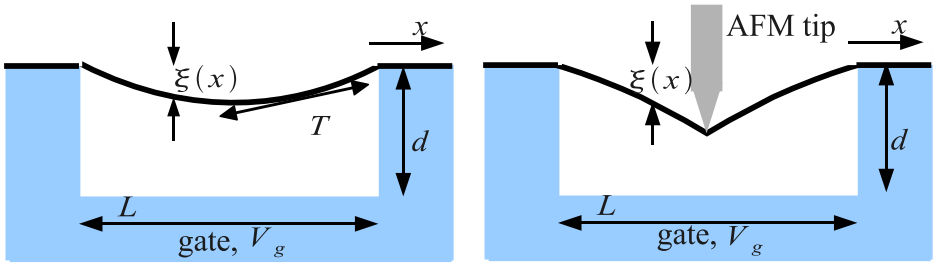

Figure 6.1. Side view of a deformed graphene flake suspended over a gate. The deformation is caused only by the interaction with a gate (left) or by the gate and an AFM-tip (right).

tivity is obtained using the Landauer formula. This correction can be big for sufficiently strong deformations of the flake which can be produced by an AFM tip. In Section 6.4 we discuss the results and the not considered in this Chapter.

6.2 Deformation of the graphene sheet

In this Section, we calculate the profile of the graphene sheet formed by electrostatic forces induced by the gates. For this purpose, we decompose the total energy of the flake as the sum of electrostatic and elastic energies. We consider a graphene flake of the length L (direction x) and the width W (direction y). For simplicity, we assume $W \gg L$. An undeformed sheet occupies a part of the plain $z = 0$; the electrostatically induced deflection is $\xi(x, y)$. Below we only consider small deformations so that we can stay within the limits of linear theory of elasticity (Hooke's law). At stronger deformations, as expected from the general theory [66] and also confirmed by theoretical modeling [10] and by experiments [21] on graphene, non-linear terms become important. However, there is a considerable parameter range, with the displacements up to 50 nm for length of the flake about 1 μm, where the linear regime is still valid. We discuss the terms which go beyond Hooke's law [10] in Section 6.4.

For electrostatic energy, similarly to Ref. [104], we model the system as a capacitor between the flake and the gate, with the distributed capac-

itance C_g dependent on the profile of the flake,

$$C_g = \int c[\xi(x,y)]dxdy. \tag{6.1}$$

Electrostatic coupling to the leads is modeled via contact capacitances C_L, C_R and resistances R_L, R_R, see. Fig (6.1). The total electrostatic energy of the system carrying the charge Q is

$$F_{electr} = -\frac{Q^2}{2C_0} + \frac{Q}{C_0}(C_L V_L + C_g V_g) - \frac{C_L C_g V_L V_g}{2C_0} + \\ + \frac{C_L V_L^2 (C_0 - C_L)}{2C_0} + + \frac{C_g V_g^2 (C_0 - C_g)}{2C_0} ,$$

with $C_0 = C_L + C_R + C_g$.

From now on, we assume that the contacts are ideal, $C_L = C_R = 0$, and thus the electrostatic energy is

$$F_{electr} = -\frac{Q^2}{2C_g} + QV_g. \tag{6.2}$$

The effect of non-ideal contacts is discussed in Section 6.4.

6.2.1 Elastic energy

We evaluate the elastic energy in the thin-plate approximation. The elastic energy consists of the bending contribution $F_1(\xi(x,y))$ and the stretching contribution $F_2(u_{\alpha\beta}(x,y))$, where $u_{\alpha\beta}(x,y)$ is the deformation tensor, and α and β denote the coordinates in the plane of the sheet (x and y). In the linear regime, the bending contribution is less important than the stretching one, however, we consider both contributions for completeness. Explicitly, we have [66]

$$F_1(\xi) = \frac{D}{2}\int\int dxdy \left(\frac{\partial^2\xi}{\partial x^2} + \frac{\partial^2\xi}{\partial y^2}\right)^2 + \\ + \int\int dxdy(1-\nu^2)\left[\left(\frac{\partial^2\xi}{\partial x \partial y}\right)^2 - \frac{\partial^2\xi}{\partial x^2}\frac{\partial^2\xi}{\partial y^2}\right] \tag{6.3}$$

and

$$F_2(u_{\alpha\beta}) = h_0 \frac{u_{\alpha\beta}\sigma_{\alpha\beta}}{2} . \tag{6.4}$$

Here $D = Eh_0^3/(12(1-\nu^2))$ is the bending rigidity, E is the Young modulus, ν is the Poisson ratio, h_0 is the thickness of the plate (graphene flake) , and $\sigma_{\alpha\beta}$ is the stress tensor.

In addition, if a local force (for instance, an AFM tip) acts on the graphene flake, it is best represented by external pressure $P_{ext}(x,y)$. The work of this external pressure to deform the flake by $\delta\xi(x,y)$ is $F_3 = \int P_{ext}\delta\xi(x,y)df$, where df is the surface element.

The profile of the sheet is determined by minimizing its total energy. Performing the variation, we find the equation describing the shape of the flake,

$$D\Delta^2\xi - \frac{\partial}{\partial x_\beta}(h_0\sigma_{\alpha\beta}\frac{\partial\xi}{\partial x_\alpha}) = P_{el}(x,y) + P_{ext}(x,y), \tag{6.5}$$

$$\frac{\partial\sigma_{\alpha\beta}}{\partial x_\beta} = 0, \tag{6.6}$$

with $P_{el}(x,y)$ being the electrostatic pressure on the plate, induced by the variation of electrostatic energy (6.2). For ideal contacts, $P_{el}(x,y) = n^2(x,y)/2\epsilon_0$. Here $n(x,y)$ is the electron density. Eq. (6.5) is the most general equation for $\xi(x,y)$ in the linear approximation of elasticity theory. For an infinitely wide graphene flake, $W \gg L$, the deformation in the y direction is homogeneous.

At sufficiently small deformations, the tension along the sheet is constant over the sheet (6.6), $h_0\sigma^0_{\alpha\beta} = T\delta_{\alpha\beta}$. The tension T is the sum of two contributions:

$$T = T_0 + T_H,\ T_H = \frac{Eh_0}{1-\nu^2}\Delta L/L \tag{6.7}$$

The first one, T_0, is the residual stress which results from the fabrication process or is induced by the ripple formation [94, 67]. The second contribution, T_H, is an internal force due to the relative elongation $\Delta L/L$ (Hooke's law). If we take this term into account, we can go beyond the thin-plate approximation and consider deformations bigger then the thickness of the graphene layer.

In the two following Subsections, we solve the above equations for two specific situations: homogeneous external force (which can be produced by a bulk bottom gate), and local force (produced for example by an AFM tip).

6.2.2 Homogeneous force: Deformation by a bottom gate

Applying a voltage on a bottom gate is a standard way to vary electron density in graphene. If the suspended graphene flake is charged, it is subject to a mechanical force proportional to the charge density. If the area of the gate is much larger than the area of the flake, the electron density induced by the gate is constant almost everywhere, $n = Q/WL$, except for the clamping points of the flake, where it is determined not only by the solution of the Poisson equation (providing singularities at the capacitor edges), but also by the metallic leads to which the flake is clamped. Indeed, experimental evidence for this charge inhomogeneity exist and can be accessed by asymmetry of the Dirac peak in conductivity [102]. However, these density inhomogenities at the clamping areas very little affect the deformation, since the displacement vanishes at the edges of the flake. Therefore we can approximate the effect of the gate by homogeneous electrostatic pressure over the flake, $P = \epsilon_0 V_g^2/2d^2$, V_g and d being the gate voltage and the distance to the gate. The profile of the graphene sheet is found from the equation

$$D\frac{\partial^4 \xi}{\partial x^4} - T\frac{\partial^2 \xi}{\partial x^2} = P, \tag{6.8}$$

where the stress T is constant over the sheet (6.7) and the deformation-dependent contribution to it depending has to be found self-consistently,

$$T_H = \frac{Eh_0}{2(1-\nu^2)} \int_0^L \xi'^2(x) dx \tag{6.9}$$

(the case for inhomogeneous T_H derived in Ref. [10] is discussed in Section 6.4 and does not induce significant difference in results). For the boundary condition corresponding to the clamping the sheet, $\xi(0) = \xi(L) = \xi'(0) = \xi'(L) = 0$, the profile is

$$\begin{aligned} \xi(x) &= \frac{PL}{2T\mu}\left[\frac{\sinh \mu L}{\cosh \mu L - 1}(\cosh \mu x - 1) - \sinh \mu x + \mu x\right. \\ &- \left.\frac{\mu x^2}{L}\right], \quad \mu = \sqrt{\frac{T}{D}}\,. \end{aligned} \tag{6.10}$$

The profile (6.10) is parabolic in the middle of the strip (as noted in Ref. [38]). As we show below, in graphene the dimensionless parameter μL

assumes large values. In this case, the profile can be simplified, and near the middle of the strip has the form

$$\xi(x) = \frac{PL}{2T}\left(x - \frac{x^2}{L}\right). \tag{6.11}$$

Close to the edges, the profile becomes $\xi(x) = P\mu L x^2/4T$. Substituting this shape into Eqs. (6.3) and (6.4), we find the values of the parameters F_1 and F_2,

$$F_1 = \frac{P^2 LW}{16T\mu^2(-8+\mu L)}, \tag{6.12}$$

and

$$F_2 = \frac{T^2 WL(1-\nu^2)}{Eh_0}. \tag{6.13}$$

The maximum vertical displacement obeys the equation

$$\xi_{max} = \frac{PL^2}{8(T_0 + 8Eh_0\xi_{max}^2/(3(1-\nu^2)L^2))}. \tag{6.14}$$

The deformation of the sheet leads to the redistribution of the electron density, which in the Thomas-Fermi approximation is

$$n(x) = V_g\epsilon_0/(d - \xi(x)).$$

In its turn, the density redistribution affects the profile of the sheet, and needs, in principle, to be calculated self-consistently. However, as soon as the displacement ξ_{max} is much smaller than the distance to the gate, the later effect is insignificant (of the order of ξ_{max}/d), and we will use the shape (6.10) not modified by the density redistribution.

The charge over the graphene flake is determined from minimization of the total energy of the system with respect to electron density n,

$$-V_g + \frac{nd}{\epsilon_0}\left[1 - \frac{8}{3}\frac{\xi_{max}}{d} + \left(1+\frac{1}{2}\right)\frac{\xi_{max}}{d\mu L} + \frac{1}{3}\frac{\xi_{max}}{d}\right] = 0, \tag{6.15}$$

where the maximum deformation of the sheet in the middle, ξ_{max} (6.14), depends on charge density. The second term in the brackets and 1 from the third term come from electrostatic energy and originate from the redistribution of the charge density due to variation of the distance between parts of deformed graphene and the gate. The rest (1/2) of the third term comes from bending energy. The fourth term takes into account dependence of

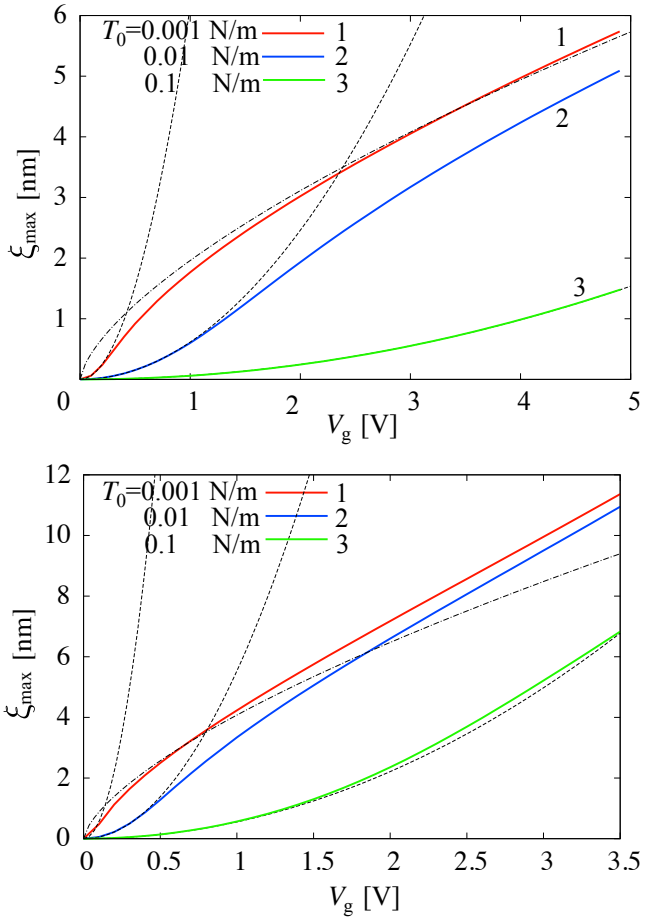

Figure 6.2. Dependence of the maximum deviation on the gate voltage, $\xi_{max}(V_g)$. The solid curves represent the self-consistent solution of nonlinear coupled equations for the deformation of the flake and the charge induced by the gate, Eqs. (6.14) and (6.16). The distance to the gate is $d = 300$ nm (top panel) and $d = 100$ nm (bottom panel). Other parameters of the graphene flake, length $L = 1$ μm, Young's modulus $E = 1$ TPa, Poisson ratio $\nu = 0.15$, and the thickness of the flake $h_0 = 0.34$ nm, are chosen in order to model real experimental data. The results are given for the different values of the residual stress: the curve 1 is for $T_0 = 0.001$ N/m, 2 is for $T_0 = 0.01$ N/m, 3 is for $T_0 = 0.1$ N/m. For each value of the residual stress, the asymptotic curves at low gate voltages (6.17) are shown as dashed lines, the curve 3 for high residual stress coincide perfectly with its asymptote. The asymptotic curves for low residual stress, Eq. (6.19), are shown by dashed-dotted lines. The correspondence between the solution of equations and asymptotes for low residual stress is not perfect. The reason is that the asymptotes are calculated for the linear charge-voltage dependence, and $n(V_g)$ is non-linear according to Eq. (6.16) for sufficiently high gate voltages on the flake.

the stretching force T over the flake on the charge density via the deflection (Eq. (6.9)). Calculations are made under the assumption $\mu L \gg 1$, which is realistic for available experiments. Simplifying Eq. (6.15), we obtain

$$-V_g + \frac{nd}{\epsilon_0}\left(1 - \frac{7}{3}\frac{\xi_{max}}{d} + \frac{3}{2}\frac{\xi_{max}}{d\mu L}\right) = 0 \tag{6.16}$$

At low gate voltages, Eq. (6.16) yields the linear gate voltage dependence of the electron density, $n_0 \equiv V_g\epsilon_0/d$. There is non-linear deviation from this dependence at higher gate voltages and at rather low initial strain T_0.

The maximum deformation can be expressed analytically in two limiting cases. First, if the residual stress T_0 is stronger than the induced stress T_H, it mostly accounts for the deformation of the sheet,

$$\begin{aligned} T_H &= \frac{Eh_0P^2L^2}{24(1-\nu^2)T_0^2} \ll T_0, \left(\frac{Eh_0P^2L^2}{24(1-\nu^2)}\right)^{1/3} \ll T_0, \\ \xi_{max} &= \frac{\epsilon_0 V_g^2 L^2}{16 d^2 T_0}\,, \qquad (6.17) \\ \frac{n-n_0}{n_0} &= \frac{7}{3}\frac{\xi_{max}}{d}\left(1 - \frac{72}{7\sqrt{T_0/D}L}\right). \qquad (6.18) \end{aligned}$$

In the case of low residual stress, one obtains

$$\begin{aligned} T_0 \ll T_H &= \frac{1}{2}\left(\frac{Eh_0P^2L^2}{3(1-\nu^2)}\right)^{1/3}, \\ \xi_{max} &= \frac{1}{4}\left(\frac{3V_g^2\epsilon_0(1-\nu^2)L^4}{2d^2Eh_0}\right)^{1/3}, \qquad (6.19) \\ \frac{n-n_0}{n_0} &= \frac{7}{3}\frac{\xi_{max}}{d} - 12\sqrt{\frac{3D(1-\nu^2)}{2Eh_0}}. \qquad (6.20) \end{aligned}$$

The maximum deviation ξ_{max}, obtained from the numerical solution of coupled nonlinear equations Eqs. (6.14), (6.16), as well as asymptotic expressions (6.17) and (6.19), are shown in Fig. 6.2 for different values of initial stress T_0. According to Eqs. (6.18) and (6.20), the nonlinear part of the charge induced on the graphene flake follows the dependence $\xi_{max}(V)/d$. Consequently, we encounter several regimes for the deformation,

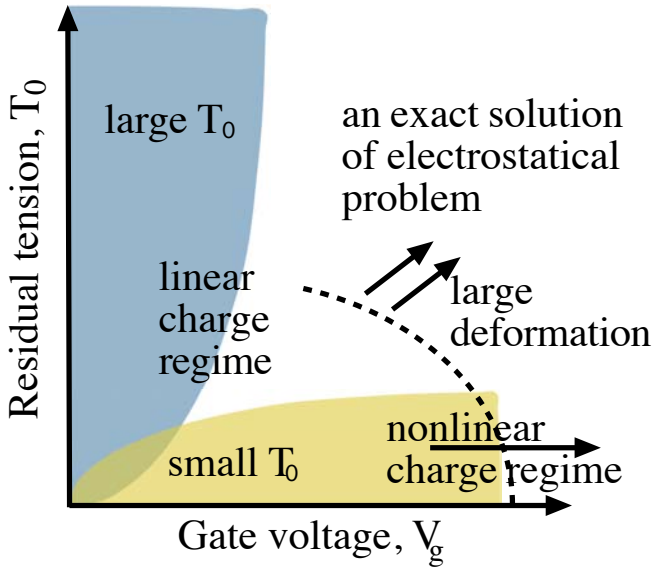

Figure 6.3. Regimes of the deformation of suspended graphene. For large residual stress T_0 the asymptotics Eq. (6.17) are valid, and the charge on the flake follows the gate voltage linearly. For small T_0 the asymptotes Eq. (6.19) are valid, the charge is linear with the gate voltage at low gate voltages and starts to follow non-linear dependence with increasing voltage. At high gate voltages, when the deformation of the flake is bigger than $\xi_{max}/d \sim 0.1$, one needs to solve self-consistently the electrostatic problem and the problem of elasticity, analytical results for this region are not available.

- at large T_0 the charge–voltage dependence is linear for realistic parameters because the maximum deformation is not too large for realistic characteristics of graphene flake. It is shown in Fig. 6.2 for $T_0 = 0.1$ N/m that the maximum deformation is in a good agreement with Eq. (6.17);

- at small T_0 and low gate voltages V_g the charge–voltage dependence can be in linear regime, and the maximum deformation follows Eq. (6.19). We illustrate this for the flake with the parameters $T_0 = 0.001$ N/m and distance to the gate $d = 300$ nm (See. Fig. 6.2, top), where the solutions of coupled electrostatic and elastic equations, Eq. (6.14), (6.16), follow asymptotic expression Eq. (6.19). The charge redistribution does not need to be taken into account;

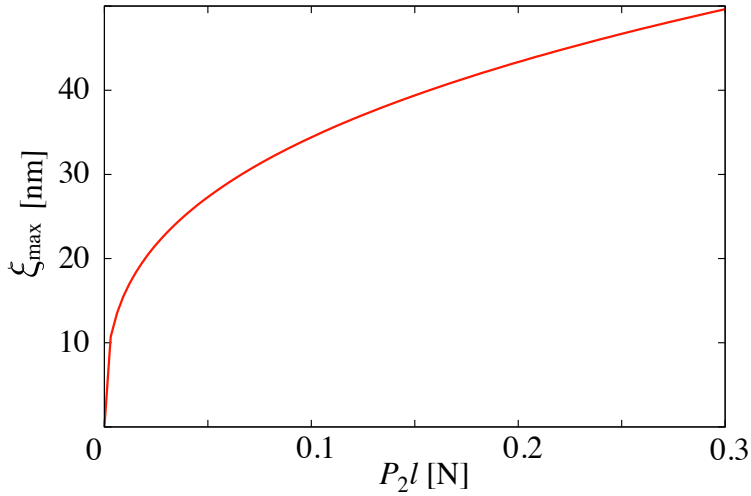

Figure 6.4. Dependence of the maximum deformation ξ_{max} on the applied force $P_2 l$ for the case of the point force in the middle of the graphene sheet. Only the curve for $T_0 = 0$ is shown, since the residual stress is not important for this case: The strain created by deformation becomes large (more than 0.1 N/m) already at moderate deformations in the middle, $\xi_{max} \sim 10$ nm. Other parameters of the flake are $L = 1\mu m$, $d = 300$ nm, $E = 1$ TPa, $\nu = 0.15$, $h_0 = 0.34$nm.

- at small T_0 and large V_g the system is in the non-linear charge regime. This situation can be realized for small distances to the gate when the coupling of the graphene sheet to the gate is large, so that it is possible to create large deformations using low gate voltages. For example, at $d = 100$ nm the non-linear charge regime influences the deformation already at voltage $V_g = 2$ V, at the bottom plot Fig. 6.2 we can see the intersection of the asymptotical curve (6.19) and the actual solution of Eqs. (6.14), (6.16).

The schematic representation of these regimes is shown in Fig. 6.3.

6.2.3 Local force: Deformation by an AFM tip

Next, we consider a concentrated force acting on graphene. This force can be provided, for example, by an AFM tip. The effect of the tip is modeled by strong pressure exerted on a narrow area of the width $l \ll L$. We assume that the problem is still homogeneous in the y-direction, which simplifies the calculations enormously. Inclusion of a pressure action in a narrow

circle, which is experimentally relevant for an AFM tip, is not expected to bring qualitatively new features. We consider pressure $P(x) = P_1, 0 < x < L/2 - l/2, L/2 + l/2 < x < L$ and $P(x) = P_2, L/2 - l/2 < x < L/2 + l/2$. Here P_2 is the local pressure, and P_1 can describe homogeneous pressure due to electrostatics, for realistic setups local pressure is much larger than pressure due to interaction with the gate $P_1 \ll P_2$.

The maximum displacement of the flake (realized at the central point) is easy to write down for $\mu L \gg 1$ and $l \ll L$:

$$\begin{aligned} \xi_{max} &= \frac{P_1\left((\mu L/2)^2 e^{\mu l/2} - 2e^{-\mu l}\right)}{2\mu^2 T} + \\ &+ \frac{P_2\left(e^{-\mu l} + e^{\mu l}\mu^2 l L/4\right)}{\mu^2 T}. \end{aligned} \tag{6.21}$$

For $P_1 \ll P_2$ and $1 \ll e^{\mu l/2} L\mu l\mu/4$ we obtain

$$\xi_{max} = \frac{P_2 l L}{4T}. \tag{6.22}$$

The profile of the graphene sheet in this approximation becomes

$$\xi(x) = \frac{2\xi_{max}}{L}|x - L/2|. \tag{6.23}$$

In the limits of weak and strong residual stress the deformation is determined by

$$T_H = \frac{Eh_0}{8(1-\nu^2)}\left(\frac{P_2 l}{T_0}\right)^2 \ll T_0, \left(\frac{Eh_0}{8(1-\nu^2)}P_2^2 l^2\right)^{1/3} \ll T_0,$$

$$\xi_{max} = \frac{P_2 l L}{4T_0}; \tag{6.24}$$

and

$$T_0 \ll T_H = \frac{1}{2}\left(\frac{Eh_0 P_2^2 l^2}{1-\nu^2}\right)^{1/3},$$

$$\xi_{max} = L\left(\frac{P_2 l(1-\nu^2)}{8Eh_0}\right)^{1/3}. \tag{6.25}$$

The dependence of the maximum deformation on the applied external local force is shown in Fig. 6.4. The deformation produced by this force is much bigger than the deformation caused by electrostatic pressure of the gate. The electrostatic problem for this case can be solved separately from the problem of elasticity.

6.3 Piezoconductivity of graphene flake

It was shown experimentally [19] that suspended graphene flakes are described with good precision as purely ballistic. Theoretically, conductance is determined by Landauer formula [118]

$$G = 4e^2/h \sum_{n=0}^{N-1} T_n, \tag{6.26}$$

where T_n is the transmission eigenvalue in the transport channel n, and the factor $4e^2/h$ is conductance of a single transport channel which takes into account valley and spin degeneracy. The number of open transport channels $N = Wk_F/\pi$ is proportional to the Fermi momentum $k_F = (\pi n/e)^{1/2}$, and thus the conductivity, $\sigma = GL/W$, is proportional to the square root of the electron density n, $\sigma \propto \sqrt{n}$.

The conductivity of graphene flake suspended over a gate can deviate from this dependence. To start with, due to electrostatic interaction with the gate, the density becomes inhomogeneous [111]. In particular, Poisson equation leads to the square root divergence of the electron density at the clamping points, as in any capacitor (see e.g. Ref. [83], [1]). To treat this divergence properly, one has to take into account electrostatic interaction with the contacts near the edge of the graphene strip, which modifies significantly the electron density near the edge, removing the divergence. However, the effect of this inhomogeneous density close to the contacts does not affect the piezoconductivity of the flake, since the deformation close to the clamping points is very weak, and thus it can be included into the contact resistance at the clamping points.

We now turn to the effects of the deformation on the conductivity. Deformation of graphene can change the conductivity by inducing changes in the band structure (which results in pseudo-magnetic fields) as well as by changing the electron density over the flake. We consider both these mechanisms and will show that typically the effect of the density redistribution dominates.

Electrons in graphene obey Dirac equation. Deformation of the flake influences on the Dirac equation in three ways — it shifts the K-points by a certain amount $\delta k/k_F$ (pseudomagnetic field), renormalizes the Fermi

[1] For the case of edges of half-infinite capacitor [83] and the distance between the plates of capacitor $d = 300$ nm the region near the edge where the electrostatic divergence plays role is about 200 nm.

velocity by $\delta v_F/v_F$, and induces the variation of the electron density on the flake $\delta n/n$. The deformation correction to the conductivity is thus a function of these three dimensionless parameters.

The pseudomagnetic field, produced by the shift of the K-point, is caused by stretching and bending. The shift of the K-point due to stretching generates the vector potential [115, 38]

$$A_y^{str} = \frac{C\tilde{\beta}}{a}(u_{xx} - u_{yy}), \quad A_x^{str} = -2\frac{C\tilde{\beta}}{a}u_{xy}, \tag{6.27}$$

where C is the order of 1, and $\tilde{\beta} = -\partial \log(t)/\partial \log(a)$, t and a being the overlap integral in the tight-binding model and the lattice parameter, respectively. For $L \ll W$ one has $u_{xy} = 0$, and hence $A_x^{str} = 0$. The deformation is homogeneous within the limits of applicability of Hooke's law, and thus $u_{xx} = \text{const}$ and $A_y^{str} = \text{const}$. This means that there is no pseudomagnetic field over the graphene flake. The pseudomagnetic field only appears in the region where the flake goes from the substrate to the suspended state [38] and, as noted above, its effect to the piezoconductivity is small, of the second order in ξ_{max}/L,

$$\frac{\delta\sigma_K}{\sigma} = \frac{A_y^{str}}{k_F}, \tag{6.28}$$

where the deformation on the edges has been estimated as

$$u_{xx} = \xi_{max}^2/L^2 + T_0(1-\nu^2)/Eh_0,$$

and $k_F = \sqrt{\pi\epsilon_0 V_g/de}$. Taking into account the value of $C\tilde{\beta}/a$ [2], we obtain

$$\frac{\delta\sigma_K}{\sigma} = 205\sqrt{\frac{d[\mu\text{m}]}{V_g[\text{V}]}}\left(\frac{\xi_{max}^2}{L^2} + \frac{T_0(1-\nu^2)}{Eh_0}\right). \tag{6.29}$$

Note the contribution from two terms induced by deformation stress and residual stress, as well as multiplication with the big prefactor 205.

[2] Parameter $C\tilde{\beta}/a$ can be taken in the form $3t_{str}\beta/ka$, where according to calculations [128] $k = 8.98N/m^2$, $\beta/a = 0.4$ N/m^2, and the parameter $\beta/(ka) = 0.0445$, t_{str} can be determined by different methods, it is approximately $t_{str} = 2\text{Å}^{-1}$ (from femtosecond time-resolved photoemission experiement [48], $t_{str} \approx 1\text{Å}^{-1}$, from analitycal estimations [93] and optical spectrum of polyacetylene, $t_{str} \approx 2.0\text{Å}^{-1}$, from tight-binding approximation $t_{str} \approx 2.5\text{Å}^{-1}$). Finally, the estimation of the $C\tilde{\beta}/a$ is 0.27Å^{-1}.

The underlying physical picture for the model of Ref. [38] is that the graphene flake is "glued" to the walls at the suspension point. Whereas this has been realized in some experiments [67], it describes the situation when the residual strain T_0 is of the same order or higher than the strain induced by the gate voltage. The residual strain results from the fabrication process and is most likely to be created by impurities in the substrate. It can be made low on purpose since the strain is reduced after annealing [25]. In the opposite situation, when the residual stress is not significant, the pseudomagnetic field is inhomogeneous and distributed over the whole suspension area.

The pseudomagnetic field is also inhomogeneous if one considers the bending contribution. Bending leads to the inhomogeneous modification of the overlap of the orbitals, and the resulting pseudovector potential has the form [50]

$$A_y^{bend} = \frac{t_{bend}}{a}\left(\frac{\theta^2(a,x)}{2} - \frac{\theta^2(\frac{a}{2},x)}{2}\right) , \tag{6.30}$$

$\theta(a,x)$ being the angle between normal vectors to the graphene surface at the points x and $x+a$, and the constant [59] $t_{bend} = 3.21$ [3]. The shape dependence of $\theta(a,x)$ has the form

$$\theta^2(a,x) = a^2\left(\frac{\partial^2\xi}{\partial x^2}\right)^2\left(1+\left(\frac{\partial\xi}{\partial x}\right)^2\right)^{-1} .$$

This yields $A_y^{bend} \approx (3t_{bend}/8a)(\xi_{max}a/L^2)^2$. Hence the contribution from bending is approximately $(a/L)^2$ times smaller than from stretching without residual stress, and is thus negligibly small, even though the resulting magnetic field is not homogeneous.

The easiest way to estimate inhomogeneous stretching of graphene is to take Hooke's law in the local form, $T_H(x) = Eh_0u_{xx}(x)$. Since the maximum relative deformation can be estimated as $u_{xx} = \xi_{max}^2/L^2$, naively, the correction from non-homogeneous stretching is of the same order as the one from delta-functional pseudomagnetic field at the clamping edges. We show below, however, that the correction from non-uniform stretching is of the order of ξ_{max}^4/L^4, but still due to large prefactor it can reduce the conductivity at low gate voltages.

Another effect induced by the deformation is the renormalization of the Fermi velocity. The renormalized value of the velocity can be derived

[3] follows from consideration of orbital overlapping.

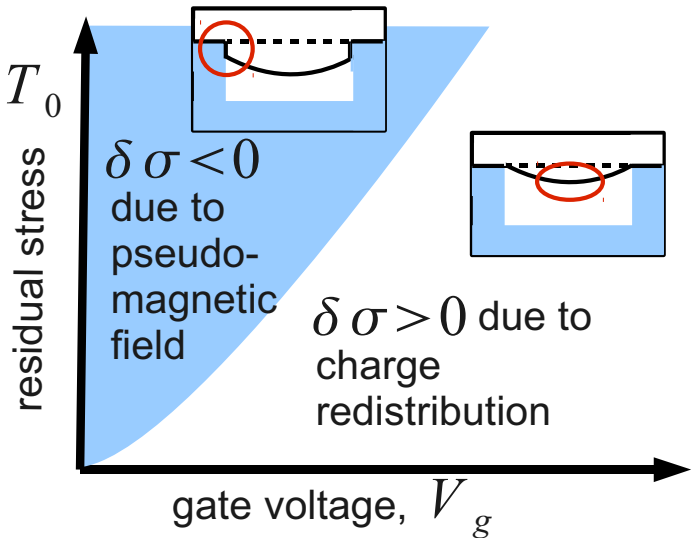

Figure 6.5. Schematic behavior of piezoconductivity. For low residual stress T_0 the correction is mainly due to the charge redistribution and has positive sign. For high residual stress the correction is negative.

from the tight-binding model. Assuming that the graphene sheet is only deformed in the x-direction, we find that the x-component of the Fermi velocity is unchanged wheres the y-component is renormalized,

$$v_{Fy} = v_F(1 - C\tilde{\beta}u_{xx}), \tag{6.31}$$

so that approximately $v_{Fy} \approx v_F(1-\xi_{max}^2/L^2)$. The effect of the renormalization on the conductivity is not significant and has the order of magnitude ξ_{max}^2/L^2. Note that this is the same dependence on ξ_{max}/L as for pseudomagnetic fields, however, it is not enhanced by a big prefactor.

The influence on conductivity of such change in Fermi velocity is not significant. This influence can be in principle measured experimentally as the conductivity variation at the Dirac point, similarly to how we explain below in Subsection 6.3.2.

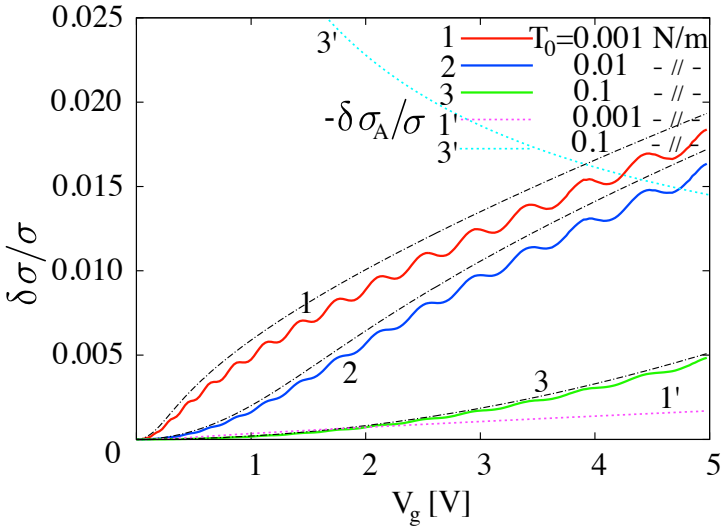

Figure 6.6. The correction to conductivity. Parameters of the flake are the same as for Fig. 6.2 (top). Asymptotic expressions for the high gate voltage are shown by the dashed-dotted lines. Additionally, the correction (with the opposite sign) due to the delta-functional pseudomagnetic field at the suspension regions [38], Eq. (6.29), is shown by dotted lines (1', 3').

6.3.1 Correction to conductivity due to the charge redistribution

Redistribution of electric charge due to interactions with the gate is found from the assumption that the potential along the graphene sheet is constant, $U(x) = \delta Q(x)/\delta C(x) = const$, where $\delta C(x)$ is the capacitance of the element of the length δx of graphene, $\delta C(x) = \epsilon_0 W \delta x/(d - \xi(x))$, and $\delta Q(x) = n(x) W \delta x$ is the charge of this element. In the first order approximation, this gives $\delta n(x)/n_0 = \xi(x)/d$.

The conductivity of graphene is proportional to charge density n, and thus the contribution to conductivity due to charge redistribution is expected to be linear in the maximum deviation from the homogeneous density, δn_{max}. Thus, the correction to conductivity is expected to be $\delta\sigma/\sigma \sim \xi_{max}/d$. Before starting the calculation of the correction to conductivity, we estimate the range where this correction of the order of ξ_{max}/d is more important than the correction due to pseudovector po-

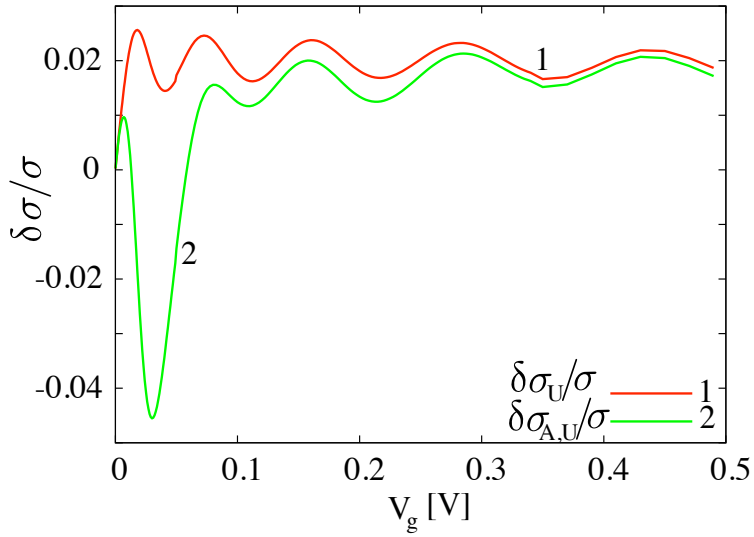

Figure 6.7. Dependence of the piezocorrection to conductivity on the gate voltage for fixed deformation, obtained by solving the Dirac equation by exact transfer matrix method. Here, $\delta\sigma_U$, the curve marked 1, is the correction with only charge redistribution taken into account, and $\delta\sigma_{A,U}$, the curve 2, encompasses both contributions, the one due to non-uniform tension and the one due to charge redistribution. At low gate voltages the correction $\delta\sigma_{A,U}$ is mostly caused by pseudomagnetic field and is negative, for higher gate voltages it changes sign and approaches $\delta\sigma_U$. The correction only due to pseudomagnetic field according to Eq. (6.40) is proportional to $1/\sqrt{V_g}$, so that it vanishes at large gate voltages. The parameters of the graphene flake are $L = 1\mu m$, $d = 300$ nm, $E = 1$ TPa, $\nu = 0.15$, $h_0 = 0.34$nm.

tential which we considered above, Fig. 6.5,

$$T_0[\mathrm{N/m}] < 10^{-3}\frac{L}{d}\sqrt{\frac{V_g^{5/2}[\mathrm{V}]}{d^{3/2}[\mu\mathrm{m}]}}. \tag{6.32}$$

As noticed in Ref. [38] the pseudovector potential at low gate voltages blocks conductivity, this is seen from Eq. (6.29). For large deformation the expressions (6.19) are valid, residual stress is not important any more, and thus the gate voltage should be large enough to see the decrease of conductivity,

$$V_g[\mathrm{V}] > 2.8\frac{L^4}{d^4}\frac{1}{d[\mu\mathrm{m}]}. \tag{6.33}$$

This deformation is so strong that in can not be reached in practice.

For the deformation with AFM the residual stress is not important and at deviations

$$\xi_{max}[\text{nm}] > 2.5\frac{L^2[\mu\text{m}]}{d[\mu\text{m}]}\sqrt{\frac{V_g[\text{V}]}{d[\mu\text{m}]}} \tag{6.34}$$

correction to pseudovector potential starts to suppress the conductivity.

To calculate the correction due to the charge redistribution, we notice that the density variation is translated into the correction for conductivity via the variation of the transmission probabilities T_n, which are the eigenvalues of the matrix $\hat{t}^\dagger\hat{t}$, $\hat{t}$ being the transmission matrix of the graphene sheet. The transmission eigenvalues t_q are determined in Appendix by the transfer matrix method. The correction to the conductivity is linear in the density shift δn, and consequently in the maximum deformation ξ_{max} (as is shown above from simple qualitative considerations). It has the form (see Appendix)

$$\begin{aligned}\delta\sigma_U &= \tfrac{L}{W} \sum_q 4\left|t_q\right|^2 \frac{q^2k_F^2}{k^3}\sin kL \\ &\times \int_0^L dx\frac{\xi(x)}{d}\sin k(L-x)\sin kx,\end{aligned} \tag{6.35}$$

where $|t_q|^2 = (\cos^2 kL + k_F^2\sin^2 kL/k^2)^{-1}$ is the transmission probability for the mode labeled by the transverse momentum $q = 2\pi n/W$, n being an integer number, and k is a wave number in the direction along the strip, so that $k_F^2 = k^2 + q^2$.

To carry out more detailed analysis, we consider specific deformation setups discussed in Section 6.2 — homogeneous and local deformation.

Eq. (6.35) can be analyzed analytically for small and large values of the parameter k_FL, which characterizes the charge density over the flake. The correction to conductivity for the homogeneous deformation (bottom gate) has the following asymptotic behavior for small and large values of k_FL (for more details, see Appendix),

$$\frac{\delta\sigma_U}{\sigma} = \begin{cases}\xi_{max}/2d, & 1 \ll k_FL; \\ 0.021\xi_{max}(k_FL)^2/d, & k_FL \ll 1.\end{cases} \tag{6.36}$$

Taking into account the functional dependence of the maximum deviation for small and large initial stress T_0, Eqs. (6.19) and (6.17), we get

the asymptotic dependence of the correction to conductivity on the gate voltage, for $T_H \ll T_0$:

$$\frac{\delta\sigma_U(V_g)}{\sigma(V_g)} \propto \begin{cases} L^2 V_g^2/T_0 d^3, & 1 \ll k_F L; \\ L^4 V_g^3/T_0 d^4, & k_F L \ll 1, \end{cases} \tag{6.37}$$

and for $T_0 \ll T_H$:

$$\frac{\delta\sigma_U(V_g)}{\sigma(V_g)} \propto \begin{cases} L^{4/3} V_g^{2/3}/d^{5/3}, & 1 \ll k_F L; \\ \left(V_g L^2/d^2\right)^{5/3}, & k_F L \ll 1. \end{cases} \tag{6.38}$$

Fig. 6.6 shows the exact result of summation over modes Eq. (6.35). At both high ($k_F L \gg 1$) and low ($k_F L \ll 1$) gate voltages, the correction follows the asymptotic behavior both for weak and strong residual stress T_0, Eqs. (6.38) and (6.37). On the same plot we compare the correction we found with the correction due to pseudomagnetic fields at the edges [38]. The latter one has a different sign (conductivity decreases with an increasing the stress). For high residual stress this correction is more important than due to charge redistribution, according to Ref. [38] it can block conductivity. For low residual stress it is about 10 times lower than the increasing conductivity correction. The oscillations of $\delta\sigma/\sigma$ have the period of $k_F L$ and are associated with the shift of Fabry-Perot resonances in conductivity for deformed graphene flake as compared with an undeformed flake. This shift occurs since the effective longitudinal wave vector of an electron in graphene depends on the deformation since it feels different charge density over the graphene flake. Note also that the contribution from pseudomagnetic fields does not oscillate since the value of k_F is the same for the whole flake. The first order perturbation theory in ξ_{max}/d is valid until this parameter reaches a rather large value, $\xi_{max}/d \sim 0.1$ (see Appendix for more details).

For the case of local deformation, using the graphene profile (6.23) and using the same technique as in Appendix, we find the correction for conductivity due to the charge redistribution,

$$\frac{\delta\sigma_U}{\sigma} = \begin{cases} \xi_{max}/2d, & 1 \ll k_F L; \\ 0.088\xi_{max}(k_F L)^2/d, & k_F L \ll 1. \end{cases} \tag{6.39}$$

Note that the asymptotic behavior for large $k_F L$ has the same form as for homogeneous deformation.

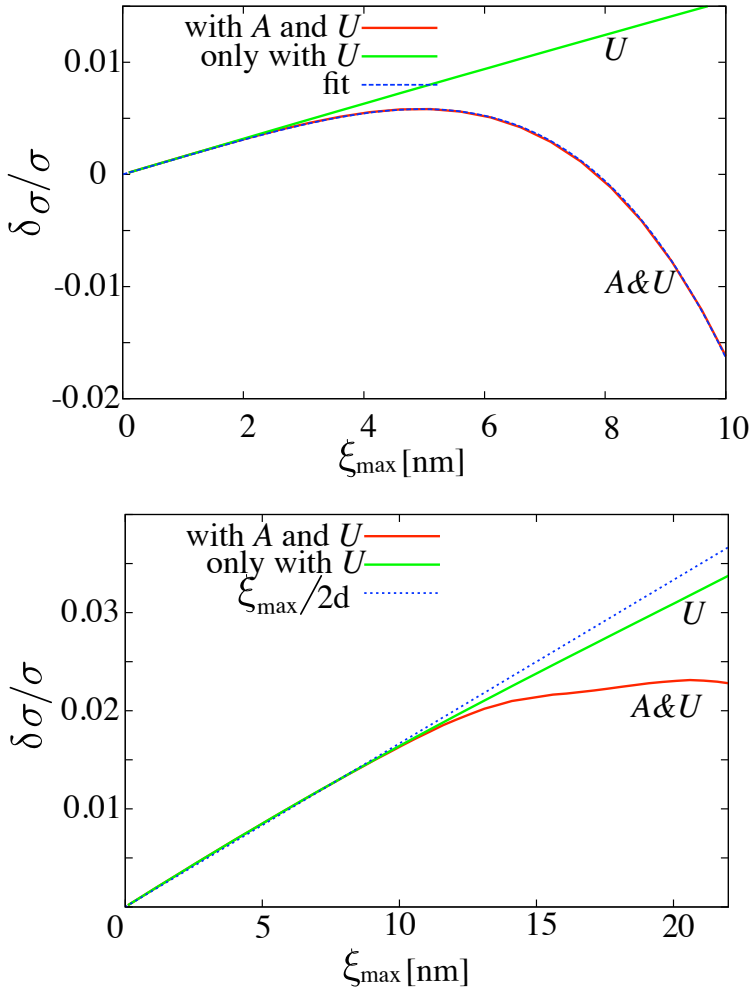

Figure 6.8. Dependence of the piezocorrection to conductivity on the maximum deviation, $\delta\sigma(\xi_{max})/\sigma$, at the fixed gate voltage $V_g = 0.03$ V (top), 3 V (bottom). We show both the correction related to the term due to non-uniform pseudovector potential, and the contribution without this term. For $V_g = 0.03$ V, we also include the best fit $V = \alpha\xi_{max} + \beta\xi_{max}^4$ which represent the sum of linear in ξ_{max} correction due to charge redistribution and the correction due to nonuniform pseudovector potential $\beta\xi_{max}^4$. The parameters of the graphene flake are $L = 1\mu m$, $d = 300$ nm, $E = 1$ TPa, $\nu = 0.15$, $h_0 = 0.34$nm.

We can also estimate the influence of inhomogeneous pseudomagnetic field assuming the local form of Hooke's law as in [10] and using the perturbation theory for the transfer matrix, as detailed in Appendix. We find that the first order perturbation theory correction in pseudovector potential vanishes, whereas the second order correction can be estimated as

$$\frac{\delta\sigma_A}{\sigma} \approx 5.5 \cdot 10^5 \frac{\xi_{max}^4}{L^4} \sqrt{\frac{d[\mu\mathrm{m}]}{V_g[\mathrm{V}]}}. \tag{6.40}$$

At low gate voltages and large deformations (for instance, induced by local deformation), this correction can be more important that the one from the charge redistribution, and thus the conductivity will be suppressed. From comparison of Eqs. (6.40) and (6.39) this supression happens for deformations:

$$\frac{\xi_{max}}{L} > 10^{-2} \sqrt[6]{\frac{d[\mu\mathrm{m}]}{V_g[\mathrm{V}]}} \left(\frac{L}{d}\right)^{1/2}. \tag{6.41}$$

We demonstrate this by solving numerically by transfer matrix method the Dirac equation with additional potential due to charge redistribution and pseudovector potential, Fig. 6.7. At fixed large $\xi_{max} = 12$ nm (estimated using Eq. (6.41)) and at low voltages the conductivity starts to decrease due to inhomogeneous tension distribution in the flake, and at higher voltages increases again due to the effect of charge redistribution. Fig. 6.8 shows that for small gate voltages lower maximum deformation ξ_{max} is required to reach the point where the conductivity starts to decrease, in agreement with Eq. (6.40). For high gate voltages $V_g \sim 3$ V pseudomagnetic fields lead to saturation of the conductivity rather than to its decrease.

6.3.2 Two-gate geometry

Conductivity can also be used to measure relative stretching of deformed suspended graphene. Note that the influence of stretching on the conductivity of graphene deposited on a substrate has been demonstrated experimentally [60]. For suspended graphene it is more difficult to extract the value of stretching than from the graphene on the substrate, since the gate voltage simultaneously varies the concentration and deforms graphene, as shown above.

To measure relative stretching of suspended graphene, we propose the two-gate geometry (Fig. 6.9). The deformation of the graphene flake is

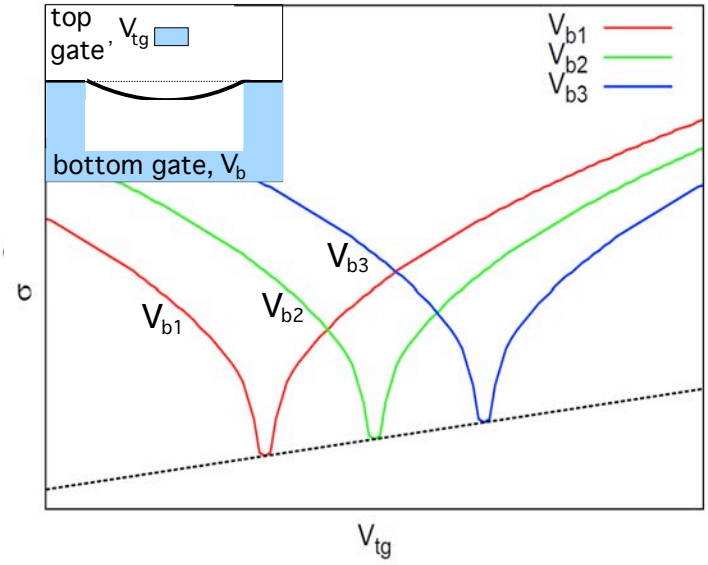

Figure 6.9. Schematic dependence of conductivity of suspended graphene on the top gate voltage for several fixed bottom gate voltages. The conductivity at the Dirac point is slightly shifted due to change in Fermi velocity caused by deformation. The difference between the values of conductivity of the Dirac peaks for different bottom gate voltages, V_{b1} and V_{b2}, is proportional to the difference in relative deformations, $(\sigma_D(V_{b1}) - \sigma_D(V_{b2}))/\sigma_D \sim u_{xx}(V_{b1}) - u_{xx}(V_{b2})$.

created by the large bottom gate, the influence of the top gate on the deformation is small as the top gate is narrow. The top gate is used to vary the charge density in the region underneath it. In this geometry at the fixed voltage at the bottom gate one can move through the Dirac point by varying the voltage at the top gate (the experiment for bilayer with two gates on the substrate [91]). The value of conductivity at this point depends on the deformation.

The stretching of the graphene flake, as discussed above, induces variations of the conductivity for two reasons. First, it induces pseudomagnetic fields. These, however, can be gauged away of Dirac equation [75] at the Dirac point and do not influence the conductivity. Second, it shifts the Fermi velocity. The relative shift is proportional to the deformation, $\delta v_F/v_F \sim \xi^2_{max}/L^2$, and leads to the positive correction of the conductivity at the Dirac point, $\delta\sigma/\sigma \sim \delta v_F/v_F \sim \xi^2_{max}/L^2$. Thus, for different bottom gate voltages, which is equivalent to different maximum deforma-

tions ξ_{max}, the conductivity at the Dirac point is slightly different, and the relative graphene stretching can be restored from this dependence. For example, consider the dependence of conductivity on the top gate voltage for different bottom gate voltages (Fig. 6.9). At a fixed value of the bottom gate voltage, the conductivity as a function of the top gate voltage exhibits a peak dependence, with the minimum corresponding to the Dirac point. The difference between the values of conductivity at Dirac peaks, σ_D, for different bottom gate voltages, V_{b1} and V_{b2}, is proportional to the difference in relative deformation, $(\sigma_D(V_{b1}) - \sigma_D(V_{b2}))/\sigma_D \sim u_{xx}(V_{b1}) - u_{xx}(V_{b2})$ (we remember that $u_{xx} \sim \xi_{max}^2/L^2$).

6.4 Discussion

In this Chapter, we investigated two mechanisms which affect the conductivity of suspended graphene — charge redistribution induced by the gate(s), and pseudomagnetic fields induced by the deformation of graphene. We find that for the small residual stress T_0, the charge redistribution mechanism dominates. For low gate voltages and strong deformation, which experimentally is best realized by using AFM, the correction due to nonuniform pseudomagnetic fields is more significant. The correction due to pseudovector potential at the region of suspension can decrease conductivity at the large residual stress [38]. It is important that the two mechanisms provide corrections to conductivity which are of different signs. Indeed, the correction from pseudomagnetic fields suppresses the conductivity [38] by shifting K-points due to the vector potential. The shift is different at different points of the suspended sample, and if the deformation is big enough, the Fermi circles at the clamping points and at the centre of the flake do not overlap: The system becomes insulating. If now we take into account the effects of the gate, not only the Fermi circles are shifted, but their radii are greater at the center of the flake since the charge density is greater in the areas closer to the gate. The increase of the radii and the shift of the center compete, and we find that typically the radius increase is more important.

It is difficult to measure piezoconductivity only by using a bottom gate since the gate voltage not only bends graphene and produces the correction to the conductivity, but also shifts the overall charge density. The density dependence of the conductivity is different from the density dependence of the correction. Thus, to extract the value of piezoconductivity, one has

to compare the conductance of deformed and undeformed graphene sheet at the same density, which can only be done in the one-gate geometry by comparing the results with the theoretical prediction. In contrast, the two-gate setup, with a bottom gate fixing the overall density and the top gate (which can be an AFM tip) creating the deformation is more convenient to extract piezoconductivity. One can fix the voltage on the bottom gate and start to deform the flake with the AFM tip. At low gate voltages the conductivity decreases due to the pseudomagnetic fields, whereas at higher voltages it starts to grow due to the charge redistribution.

In the real experimental situation, the AFM tip has a point shape, whereas in this Chapter we considered for illustration the deformation homogeneous in one direction, *i.e.* replaced the tip by a rod. Non-homogeneous deformation in all directions creates pseudomagnetic fields, with the conductivity depending not only on the transverse displacement, but also locally on the position over the graphene sheet. The conductivity is the largest if the tip is placed in the middle of the sheet, and decreases if the tip moves to the side. We can understand this behavior from a simple reasoning. Indeed, the electrons which from the two sides of the tip feel the pseudomagnetic fields and interfere similarly to an Aharonov-Bohm ring. The interference is more destructive if the tip is further from the center, and thus the conductivity decreases.

Another parameter which affects the conductivity is the residual stress T_0. It can be varied experimentally for instance if one uses graphene suspended over piezosubstrate. Putting voltage on the substrate would induce extra stress on graphene, and one can move from the situation where pseudovector potential blocks the conductivity at low gate voltages to the case where residual stress does not play a role and the correction due to charge redistribution increases the conducitivity.

In this Chapter, we considered ideal ballistic graphene. In particular, we disregarded the contact resistance, assuming the clamping points to be ideal contacts. Finite transparency of the contacts would suppress both the conductivity itself and the piezocorrection to the conductivity; in addition, it would raise the amplitude of Fabry-Perot resonances.

For strong deformations of the graphene sheet, the problem becomes much more complicated, since one has now to solve elasticity equations self-consistently, taking into account that the displacement depends on the charge redistribution. This leads to additional terms in the equations of the elasticity theory. Taking into account influence of the density

redistribution on the term with electrostatic pressure in the equation of deformation, one can show that the self-consistency condition increases the deformation in the middle of the graphene sheet. This effect only becomes important at sufficiently strong deformations.

In real experiments the charge inhomogeneity of the graphene flake is not only due to surrounding electrodes but also *e.g.* charge redistribution due to charge impurities in the substrate, puddles in the non-suspended part of graphene, or left-over dopants from the process of fabrication.

First we consider the effect of the leads and inhomogeneities in the substrate or over the substrate. These density inhomogeneities are created by external electrostatic potential (see Sec. 6.2.2). This potential is not expected to change by gate voltage and merely shifts the position of the Dirac point. In this case all results involving gate voltage V_g should be corrected by the finite gate voltage offset of the Dirac point V_{gD} as $V_g \longrightarrow (V_g - V_{gD})$. Moreover, due to the screening effects in graphene the influence of the substrate impurities is weakened.

Second, we consider intrinsic charge puddles in graphene, though according to the experiments where fractional quantum Hall effect was observed [33] in suspended graphene, even in the presence of charge puddles the overall electron density remains almost homogeneous. For instance, it is reasonable to assume that every puddle contains an extra electron[78]. The gate voltage variation leads to the variation of the total potential (intrinsic plus electrostatic) over the graphene flake, and eventually one more electron enters the system. This additional electron is delocalized over the flake and shifts the conductance as discussed above. estimation by the means discussed in the Chapter. The gate voltage at which this extra electron enters the system is approximately e/C ($\delta V \approx 1meV$ for $d = 300nm$, $L = W = 1\mu m$). Thus, at noticeable gate voltages ($V > 0.1V$ for these parameters), when the number of delocalized electrons is large, the influence of intrinsic puddles is insignificant with respect to the contribution of delocalized electrons, and the conclusions of the Chapter remain unchanged. At low gate voltages, however, the puddle contribution may become significant.

Finally, we assumed that undeformed graphene is flat. In reality, it is always rippled, and, in principle, one needs to use the elasticity theory for membranes. However, we do not expect that taking ripples into account would significantly affect the results of this chapter. First, the ripples are small and have a large radius of curvature, which means they are very

little affected by the overall deformation of the graphene sheet. Second, the main effect of the ripples is to renormalize the energy over the graphene sheet [108]. We thus expect that our results are valid, but for renormalized energy over the flake (energy is determined by gate voltage in clean case, and is renormalized in the rippled case).

Appendix 6.A Perturbative corrections to conductivity

In this Appendix, we calculate the corrections to the conductivity due to both charge redistribution and pseudomagnetic fields, using the perturbation theory.

The Dirac equation for one valley in graphene has the form

$$v_F \vec{\sigma}\vec{p} + \delta U(x,y) = E \ , \tag{6.42}$$

with $\vec{\sigma} = (\sigma_x, \sigma_y)$, $\vec{p} = (p_x, p_y)$,

$$p_x = -i\hbar\partial_x + A_x, p_y = -i\hbar\partial_y + A_y,$$

$A_x(x,y)$ and $A_y(x,y)$ being the components of the pseudomagnetic vector-potential, given by Eq. (6.27), and $\delta U(x,y)$ is the additional electrostatic potential due to the charge redistribution over the graphene flake. It is determined by local variations of the Fermi energy over the flake. Since the Fermi energy depends on the charge density over the flake, $E_F(x) = \hbar v_F k_F(x)$, $k_F(x) = \sqrt{\pi n(x)/e}$, one has

$$\delta U(x)/E = \delta k_F(x)/k_F = \delta n(x)/2n = \xi(x)/2d.$$

We only consider the deformation homogeneous in y-direction.Then both A_y and δU only depend on the coordinate x, and $A_x = 0$ (see Section 6.3). The problem becomes effectively one-dimensional since the momentum q in y-direction is conserved. It is convenient to use the transfer matrix representation of Dirac equation [108] to calculate the correction to the conductivity caused by the deformation $A_y(x)$, $\delta U(x)$,

$$\begin{aligned} \mathcal{T}_H \quad & (x_2, x_1) = \mathcal{T}_{0H}(x_2, x_1) - \\ - \quad & \int_{x_1}^{x_2} dx \mathcal{T}_{0H}(x_2, x) \left(\sigma_z \delta U(x) + i\sigma_x A_y(x)\right) \mathcal{T}_{\mathcal{H}}(x, x_1) \ , \end{aligned} \tag{6.43}$$

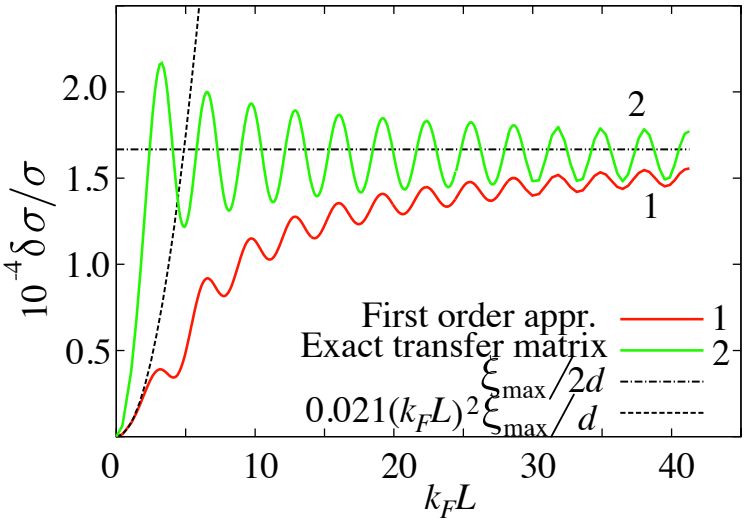

Figure 6.10. Dependence of the relative correction to conductivity on $k_F L$, $\delta\sigma/\sigma(k_F L)$ for constant $\xi_{max}/d = 1/3000$, for the correction of the first order in ξ_{max}/d, Eq. (6.47), the curve 1, and exact transfer matrix solution of integral equation, the curve 2. The correction from the exact solution has the same dependence on $k_F L$ as the first order correction, the oscillations are in the same phase. Asymptotes for small and large $k_F L$, Eq. (6.35), are shown as dashed lines. The parameters of the graphene flake are $L = 1\mu m$, $d = 300$ nm, $E = 1$ TPa, $\nu = 0.15$, $h_0 = 0.34$nm.

where $\mathcal{T}_H$ is the Hadamard transformed transfer matrix, and $\mathcal{T}_{0H}$ is the Hadamard transformed transfer matrix of the unperturbed system,

$$\mathcal{T}_{0H} = \exp\left(i\sigma_z k_F L + \sigma_x q L\right). \tag{6.44}$$

We perform the perturbation expansion of the integral form for Eq. (6.44), and in the first order in $\delta U(x)$ and $A_y(x)$ we obtain

$$\mathcal{T}_1(x_2, x_1) = \mathcal{T}_0(x_2, x_1) - \tag{6.45}$$
$$-i\int_{x_1}^{x_2} dx \mathcal{T}_0(x_2, x)\left(\sigma_z \delta U(x) + i\sigma_x A_y(x)\right)\mathcal{T}_0(x, x_1).$$

The conductance of the graphene sheet is determined by Landauer formula (6.26). According to general scattering theory [108], the transmission matrix element $\hat{t}$ is an inverse element of $\mathcal{T}_H$,

$$\hat{t} = \left(\mathcal{T}_H^{--}\right)^{-1}. \tag{6.46}$$

Taking into account Eq. (6.45), Landauer formula (6.26), and the definition (6.46), the first order corrections to conductivity due to electrostatics and pseudo-magnetic field are

$$\begin{aligned}
\delta\sigma_U &= \frac{L}{W}\sum_q 4\left|t_q\right|^4 I_U k_F L \frac{q^2 k_F}{k^3}\sin kL, && (6.47)\\
I_U &= \int_0^L \frac{dx}{L}\frac{\xi(x)}{2d}\sin k(L-x)\sin kx,\\
\delta\sigma_A &= \frac{L}{W}\sum_q 2\left|t_q\right|^4 \frac{k_F q}{k^2} I_A, && (6.48)\\
I_A &= \int_0^L dx\delta A(x)\times\\
&\times \ (\sin^2 kL - 2\cos kL\sin kx\sin k(L-x)), && (6.49)
\end{aligned}$$

where $q = 2\pi n/W$ is a wave vector in the y-direction, n is an integer number, and k is a wave vector along the strip,

$$k^2 + q^2 = k_F^2.$$

Furthermore, t_q is the transmission probability for clean system for the mode q, and

$$\left|t_q\right|^2 = (\cos^2 kL + k_F^2\sin^2 kL/k^2)^{-1}.$$

Note that the first-order correction due to the pseudo-vector potential (6.48) only contains odd powers of q, so that the sum over q vanishes. Thus, the first-order correction to the conductivity is determined solely by the density redistribution. It is linear in the maximum deviation ξ_{max}/d for small deviations.

First, we remark on the validity of Eq. (6.47). The expansion of the expression

$$1 - 4(t_q t_q^\dagger)^2 I_U k_F L\frac{q^2 k_F}{k^3}\sin kL$$

has been made under assumption that the second term is small in comparison with unity due to the small prefactor $\xi_{max}k_F L/d$. Following this argument, the expression for the first order correction to the conductivity in ξ_{max}/d is formally only valid for $\xi_{max}/dk_F L \ll 1$. However, solving the integral equation numerically, we find that this expression is valid for a broader parameter range. We compare results of calculations for the first

order correction Eq. (6.47) and numerical solution of Eq. (6.44) for the two cases: for the fixed ratio ξ_{max}/d and for the fixed value of $k_F L$. For the first case, the dependence of $\delta\sigma/\sigma$ on $k_F L$ shows the same oscillation period and the same asymptotic behavior at large $k_F L$, Fig. 6.10. For the second case, at large $k_F L \sim 40$ (for the distance to the gate $d = 300$ nm this corresponds to the gate voltage $V_g = 3$ V) the expansion clearly ceases to be valid, see Fig. 6.11. We thus conclude from the results of our numerical solution that the expression for the correction linear in ξ_{max}/d is applicable until $\xi_{max}/d \ll 1$, which is weaker than the perturbation theory suggestion $\xi_{max} k_F L/d \ll 1$.

The second order correction to conductivity contains also a term with the pseudo-vector potential, the magnitude of the term being $(\xi_{max}/L)^4$.

We consider both corrections separately. Now we perform the analysis of Eq. (6.47) for deformation with constant pressure. For this case, the shape of the strip is nearly parabolic (Section 6.2) and can be approximated as

$$\xi(x) = \frac{4\xi_{max}}{L^2}(x - L/2)^2.$$

The integral with the induced potential $\delta U(x)$ from Eq. (6.47), I_U, is

$$I_U = \frac{\xi_{max}}{12d} \frac{kL(6 - (kL)^2)\cos kL - 3(2 - (kL)^2)\sin kL}{(kL)^3}. \tag{6.50}$$

Now we can perform the summation over modes for $\delta\sigma$, Eq. (6.47), analytically in two asymptotic cases: $k_F L \ll 1$ and $k_F L \gg 1$.

For $k_F L \ll 1$, the evanescent modes give the most important contribution to the conductivity [13],

$$\sigma(k_F L \ll 1) = \frac{L}{W}\frac{W}{2\pi L}\int_{-\infty}^{\infty} \frac{dx}{\cosh^2 x} = \frac{1}{\pi}, \tag{6.51}$$

and to the correction to the conductivity,

$$\delta\sigma_U(k_F L \ll 1) = \frac{L}{W}\frac{\xi_{max}}{3d}\frac{W}{2\pi L}(k_F L)^2 I\ , \tag{6.52}$$

with

$$I = 2\int_0^{\infty} \frac{dx \sinh x(x(6 + x^2)\cosh x - 3(2 + x^2)\sinh x)}{x^4 \cosh^4 x},$$

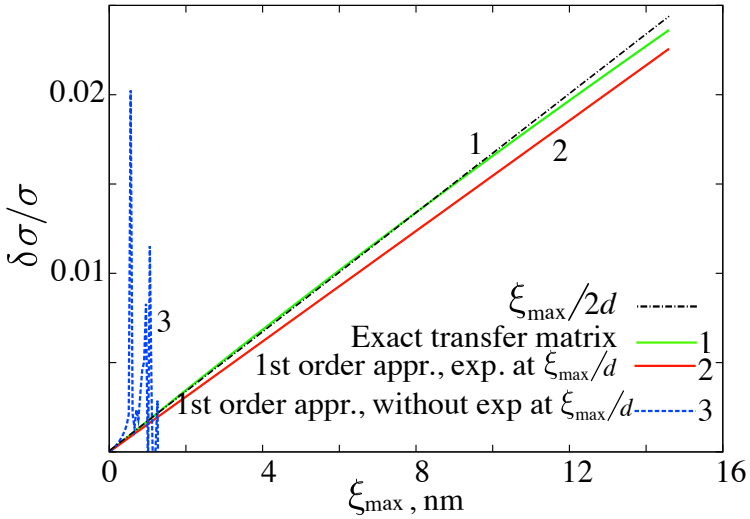

Figure 6.11. Dependence of the relative correction to conductivity on the maximum deformation, $\delta\sigma(\xi_{max})/\sigma$ for constant $k_F L = 40$, in the first order in ξ_{max}/d, Eq. (6.47), the curve 2, and the exact transfer matrix solution of integral equation, the curve 2. Both the expansion and summation of the $(\mathcal{T}^{--})^{-1}$ are not valid for $\xi_{max}k_F L/d > 1$ for small parameter as mentioned in the text. The dashed line, the curve 3, is the summation result. The exact solution shows linear dependence on deviation even for rather large deviation, and this linear dependence is close both to the correction Eq. (6.47) and to the correction averaged over fast oscillations, $\xi_{max}/2d$. The parameters of the graphene flake are $L = 1\mu m$, $d = 300$ nm, $E = 1$ TPa, $\nu = 0.15$, $h_0 = 0.34$nm.

and its numerical value is $I \approx 0.124$. The relative correction to conductivity reads

$$\frac{\delta\sigma_U}{\sigma} = \frac{\xi_{max} I}{6d}(k_F L)^2 \approx 0.021\frac{\xi_{max}}{d}(k_F L)^2. \tag{6.53}$$

For $k_F L \gg 1$ we average over fast oscillations. In this case, only the propagating modes contribute significantly to the conductivity.

To perform the averaging, we replace the summation over q by the integration,

$$\sum_q \longrightarrow \frac{W}{2\pi}\int dq.$$

To simplify subsequent calculations, we make the change of variables $q = k_F \sin\phi$, $k = k_F \cos\phi$, and then go from the integral over dq to the integral

over $d\phi$. The correction to the conductivity Eq. (6.47) has the form

$$\delta\sigma_U = \frac{L}{W}\frac{k_F W}{\pi}\frac{\xi_{max}}{d} \times$$
$$\times \int_0^{\pi/2} d\phi \frac{\cos\phi \sin^2\phi \sin^2(k_F L\cos\phi)}{(\cos^2\phi\cos^2(k_F L\cos\phi) + \sin^2(k_F L\cos\phi))^2}.$$

In this expression only the term with $3\sin kL/kL$ from Eq.(6.50) survived: All terms with $\cos kL$ vanish after averaging, and the term with $-6\sin kL/(kL)^3$ is smaller than one which is taken into account). For large $k_F L$ the terms $\cos(k_F L\cos\phi)$ and $\sin(k_F L\sin\phi)$ in Eq. (6.47) oscillate very rapidly. We can represent $\int_0^{\pi/2} d\phi$ as a sum of fast oscillating terms, with each term being an average over the period,

$$\int_0^{\pi/2} d\phi \longrightarrow$$
$$\sum_{n=0}^{N_{max}} \int_{\phi_n}^{\phi_{n+1}} d\phi f(\phi_{n+1/2}, \cos(k_F L\cos\phi), \sin(k_F L\cos\phi)),$$

with $k_F L\sin\phi_n = 2\pi n$. The integrand f is determined by structure of Eq. (6.47) and Eq. (6.50),

$$\int_0^{2\pi} f(\phi) = \int_0^{2\pi} \frac{\sin^2 x dx}{(a^2\cos^2 x + \sin^2 x)^2} = \frac{2\pi}{a}.$$

The sum over n remains, and this yields to What is left is the sum over n,

$$\delta\sigma_U = \frac{L}{W}\frac{\xi_{max}}{d}\frac{k_F W}{\pi} 2\pi \sum_n \sqrt{1-(x_n/k_F L)^2}, \tag{6.54}$$

$x_n = \pi(2n+1)$. Finally,

$$\delta\sigma_U = \frac{L}{W}\frac{\xi_{max}}{8d} k_F W. \tag{6.55}$$

The conductivity after averaging over fast oscillations becomes $\sigma = k_F W/4L/W$, and the relative correction to the conductivity is

$$\frac{\delta\sigma_U}{\sigma} = \frac{\xi_{max}}{2d}.$$

From general physical considerations about the correction (see main text), one also expects the dependence $\delta\sigma/\sigma \sim \xi_{max}/d$ for $\delta\sigma/\sigma$.

Concerning the correction due to the pseudomagnetic fields, it is of the second order in δA, and the analytical expressions are too cumbersome. Instead, we illustrate our conclusions using the numerical solution of the integral equation (6.44). It is done by multiplying transfer matrices for small intervals of the length δx. Convergence with the size of δx is reached.

References

[1] E. Abrahams, P. W. Anderson, D. C. Licciardello, and T. V. Ramakrishnan, Phys. Rev. Lett. **42**, 673 (1979).

[2] I. Adagideli, D. E. Sheehy, and P. M. Goldbart, Phys. Rev. B **66**, 140512(R) (2002).

[3] I. Adagideli and Ph. Jacquod, Phys. Rev. B **69**, 020503(R) (2004).

[4] J. Alicea, Phys. Rev. B **81**, 125318 (2010).

[5] A. Altland, B. D. Simons, and M. R. Zirnbauer, Phys. Rep. **359**, 283 (2002).

[6] A. Altland and M. R. Zirnbauer, Phys. Rev. B **55**, 1142 (1997).

[7] P. W. Anderson, Phys. Rev. **109**, 1492 (1958).

[8] Y. Asada, K. Slevin, and T. Ohtsuki, Phys. Rev. B **70**, 035115 (2004).

[9] J. K. Asbóth, A. R. Akhmerov, A. C. Berceanu, and C. W. J. Beenakker, Phys. Rev. B **80**, 224517 (2009).

[10] J. Atalaya, A. Isacsson, and J. M. Kinaret, Nano Lett. **8**, 4196, (2008).

[11] J. H. Bardarson, J. Tworzydło, P. W. Brouwer, and C. W. J. Beenakker, Phys. Rev. Lett. **99**, 106801 (2007).

[12] J. H. Bardarson, M. V. Medvedyeva, J. Tworzydło, A. R. Akhmerov, and C. W. J. Beenakker, Phys. Rev. B **81**, 121414(R) (2010).

[13] C. W. J. Beenakker, Rev. Mod. Phys. **80**, 1337 (2008)

[14] C. M. Bender, K. A. Milton, and D. H. Sharp, Phys. Rev. Lett. **51**, 1815 (1983).

[15] B. A. Bernevig, T. L. Hughes, and S.-C. Zhang, Science **314**, 1757 (2006).

[16] A. Bermudez, L. Mazza, M. Rizzi, N. Goldman, M. Lewenstein, and M. A. Martin-Delgado, Phys. Rev. Lett. **105**, 190404 (2010).

[17] M. Bocquet, D. Serban, and M. R. Zirnbauer, Nucl. Phys. B **578**, 628 (2000).

[18] K. I. Bolotin, K. J. Sikes, Z. Jiang, M. Klima, G. Fudenberg, J. Hone, P. Kim, and H. L. Stormer, Solid State Commun. **146**, 351 (2008).

[19] K. I. Bolotin, K. J. Sikes, J. Hone, H.L. Stormer and P. Kim, Phys. Rev. Lett. **101**, 096802 (2008).

[20] A. Bostwick, J. L. McChesney, K. V. Emtsev, T. Seyller, K. Horn, S. D. Kevan, and E. Rotenberg, Phys. Rev. Lett. **103**, 056404 (2009).

[21] J. S. Bunch, A. M. van der Zande, S. S. Verbridge, I. W. Frank, D. M. Tanenbaum, J. M. Parpia, H. G. Craighead, and P. L. McEuen, Science **315**, 490 (2007).

[22] A. H. Castro Neto, F. Guinea, N. M. R. Peres, K. S. Novoselov, A. K. Geim, Rev. Mod. Phys. **81**, 109 (2009).

[23] J. T. Chalker, N. Read, V. Kagalovsky, B. Horovitz, Y. Avishai, and A. W. W. Ludwig, Phys. Rev. B **65**, 012506 (2001).

[24] J. T. Chalker and P.D. Coddington, J. Phys. C **21**, 2665 (1998).

[25] C. Chen, S. Rosenblatt, K. I. Bolotin, W. Kalb, P. Kim, I. Kymissis, H. L. Stormer, T. F. Heinz, and J. Hone, Nature Nanotechnology **4**, 861 (2009).

[26] M. Cheng, R. M. Lutchyn, V. Galitski, and S. Das Sarma, Phys. Rev. Lett. **103**, 107001 (2009).

[27] V. V. Cheianov, O. Syljuasen, B. L. Altshuler, V. I. Fal'ko, Euro-Phys. Lett. **89**, 56003 (2010).

[28] S. Cho and M. P. A. Fisher, Phys. Rev. B **55**, 1025 (1997).

[29] M. Creutz, Rev. Mod. Phys. **73**, 119 (2001).

[30] M. Creutz and I. Horváth, Phys. Rev. D **50**, 2297 (1994).

[31] S. G. Davison and M. Stęślicka, *Basic Theory of Surface States* (Oxford University, Oxford, 1996).

[32] O. V. Dolgov, O. V. Danylenko, M. L. Kulic, and V. Oudovenko, Int. J. Mod. Phys. B **12**, 3083 (1998).

[33] X. Du, I. Skachko, F. Duerr, A. Luican, and E. Y. Andrei, Nature, **462**, 192 (2009).

[34] A. C. Durst and P. A. Lee, Phys. Rev. B **62**, 1270 (2000).

[35] D. C. Elias, R. R. Nair, T. M. G. Mohiuddin, S. V. Morozov, P. Blake, M. P. Halsall, A. C. Ferrari, D. W. Boukhvalov, M. I. Katsnelson, A. K. Geim, and K. S. Novoselov, Science **323**, 610 (2009).

[36] F. Evers and A. D. Mirlin, Rev. Mod. Phys. **80**, 1355 (2008).

[37] G. Feher, Phys. Rev. **114**, 1219 (1959); R. Dalichaouch, J. P. Armstrong, S. Schultz, P. M. Platzmann, and S. L. McCall, Nature **354**, 53 (1991); D. S. Wiersma, P. Bartolini, A. Lagendijk, and R. Righini, Nature **390**, 671 (1997).

[38] M. M. Fogler, F. Guinea, and M. I. Katsnelson, Phys. Rev. Lett. **101**, 226804 (2008).

[39] I. W. Frank, D. M. Tanenbaum, A. M. Van der Zande, and P. L. McEuen, J. Vac. Sci. Technol. B **25**, 2558 (2007)

[40] E. Fradkin, Phys. Rev. B **33**, 3263 (1986).

[41] L. Fu and C. L. Kane, Phys. Rev. B **76**, 045302 (2007).

[42] L. Fu and C. L. Kane, Phys. Rev. Lett. **100**, 096407 (2008).

[43] L. Fu and E. Berg, Phys. Rev. Lett. **105**, 097001 (2010).

[44] A. Furusaki, M. Matsumoto, and M. Sigrist, Phys. Rev. B **64**, 054514 (2001).

[45] A. K. Geim and K. S. Novoselov, Nature Mat. **6**, 183 (2007).

[46] G. Giovannetti, P. A. Khomyakov, G. Brocks, P. J. Kelly, and J. van den Brink, Phys. Rev. B **76**, 073103 (2007).

[47] V. Gurarie and L. Radzihovsky, Phys. Rev. B **75**, 212509 (2007).

[48] T. Hertel and G. Moos, Phys. Rev. Lett. **84**, 5002 (2000).

[49] A. Hosseini, R. Harris, S. Kamal, P. Dosanjh, J. Preston, R. Liang, W. N. Hardy, and D. A. Bonn, Phys. Rev. B **60**, 1349 (1999).

[50] Y. Huang, J. Wu, and K. C. Hwang, Phys. Rev. B **74**, 245413 (2006).

[51] J. Zhou and R. Huang, J. Mech. Phys. Solids **56**, 1609 (2008).

[52] Q. Lu, M. Arroyo, and R. Huang, J. Phys. D **42**, 102002 (2009).

[53] D. A. Ivanov, Phys. Rev. Lett. **86**, 268 (2001).

[54] R. Jackiw and G. Semenoff, Phys. Rev. Lett. **50**, 439 (1983).

[55] V. Kagalovsky and D. Nemirovsky, Phys. Rev. Lett. **101**, 127001 (2008).

[56] V. Kagalovsky and D. Nemirovsky, Phys. Rev. B **81**, 033406 (2010).

[57] C. Kallin and A. J. Berlinsky, J. Phys. Cond. Matt. **21**, 164210 (2009).

[58] M. I. Katsnelson, Eur. Phys. J. B **51**, 157 (2006).

[59] E. Kim and A. H. Castro Neto, Europhys. Lett. **84**, 57007 (2008).

[60] Keun S. Kim, Y. Zhao, H. Jang, S. Y. Lee, J. M. Kim, Kwang S. Kim, J.-H. Ahn, P. Kim, J.-Y. Choi, and B. H. Hong, Nature **457**, 706 (2009).

[61] K.-Y. Kim, Ya. M. Blanter, and K.-H. Ahn (unpublished).

[62] A. Yu. Kitaev, Phys. Usp. **44** (suppl.), 131 (2001).

[63] J. Kogut and L. Susskind, Phys. Rev. B **11**, 395 (1975).

[64] N. B. Kopnin and M. M. Salomaa, Phys. Rev. B **44**, 9667 (1991).

[65] B. Kramer, T. Ohtsuki, and S. Kettemann, Phys. Rep. **417**, 211 (2005).

[66] L. D. Landau and E. M. Lifshits, *Theory of Elasticity* (Pergamon, Oxford, 1986).

[67] C. Lee, X. Wei, J. W. Kysar, and J. Hone, Science **321**, 385 (2008).

[68] P. A. Lee, arXiv:0907.2681.

[69] P. A. Lee and T. V. Ramakrishnan, Rev. Mod. Phys. **57**, 287 (1985).

[70] P. A. Lee, Phys. Rev. Lett. **71**, 1887 (1993).

[71] S.-F. Lee, D. C. Morgan, R. J. Ormeno, D. Broun, R. A. Doyle, J. R. Waldram, and K. Kadowaki, Phys. Rev. Lett. **77**, 735 (1996).

[72] J. Linder, T. Yokoyama, and A. Sudbø, Phys. Rev. B **80**, 205401 (2009).

[73] C.-X. Liu, H. Zhang, B. Yan, X.-L. Qi, T. Frauenheim, X. Dai, Z. Fang, and S.-C. Zhang, Phys. Rev. B **81**, 041307 (2010).

[74] H. Lu, W. Shan, W. Yao, Q. Niu, and S. Shen, Phys. Rev. B **81**, 115407 (2010).

[75] A. W. W. Ludwig, M. P. A. Fisher, R. Shankar, and G. Grinstein, Phys. Rev. B **50**, 7526 (1994).

[76] A. MacKinnon and B. Kramer, Phys. Rev. Lett. **47**, 1546 (1981).

[77] N. Malkova, I. Hromada, X. S. Wang, G. Bryant, and Z. G. Chen, Opt. Lett. **34**, 1633 (2009).

[78] J. Martin, N. Akerman, G. Ulbricht, T. Lohmann, J. H. Smet, K. von Klitzing, and A. Yacoby, Nat. Phys. **4**, 144 (2008).

[79] M. V. Medvedyeva, J. Tworzydło, and C. W. J. Beenakker, Phys. Rev. B **81**, 214203 (2010).

[80] A. Mildenberger, F. Evers, A. D. Mirlin, and J. T. Chalker, Phys. Rev. B **75**, 245321 (2007).

[81] V. P. Mineev, and K. Samokhin, *Introduction to Unconventional Superconductivity* (Gordon and Breach Science Publishers, 1999).

[82] T. M. G. Mohiuddin, A. Lombardo, R. R. Nair, A. Bonetti, G. Savini, R. Jalil, N. Bonini, D.M. Basko, C. Galiotis, N. Marzari, K. S. Novoselov, A. K. Geim, and A. C. Ferrari, Phys. Rev. B, **79**, 205433 (2009).

[83] P. Morse, and H. Feshbach *Methods of Theoretical Physics*, (University Press, Cambridge, 1953).

[84] C. Nayak, S. Simon, A. Stern, M. Freedman, S. Das Sarma, Rev. Mod. Phys. **80**, 1083 (2008).

[85] H. B. Nielsen and M. Ninomiya, Nucl. Phys. B **185**, 20 (1981); H. B. Nielsen and M. Ninomiya, Nucl. Phys. B **193**, 173 (1981); D. Friedan, Comm. Math. Phys., **85**, 481 (1982).

[86] K. Nomura, M. Koshino, and S. Ryu, Phys. Rev. Lett. **99**, 146806 (2007).

[87] K. Nomura, S. Ryu, M. Koshino, C. Mudry, and A. Furusaki, Phys. Rev. Lett. **100**, 246806 (2008).

[88] K. S. Novoselov, E. McCann, S. V. Morozov, V. I. Fal'ko, M. I. Katsnelson, U. Zeitler, D. Jiang, F. Schedin, and A. K. Geim, Nature Physics **2**, 177 (2006).

[89] K. Novoselov, Nat. Materials, **6**, 720 (2007).

[90] T. S. Nunner and P. J. Hirschfeld, Phys. Rev. B **72**, 014514 (2005).

[91] J. B. Oostinga, H. B. Heersche, X. Liu, A. F. Morpurgo and L. M. K. Vandersypen, Nature Materials **7**, 151 (2007).

[92] V. M. Pereira and A. H. Castro Neto, Phys. Rev. Lett. **103**, 046801 (2009).

[93] L. Pietronero, S. Strassler, H. R. Zeller, and M. J. Rice, Phys. Rev. B **22**, 904 (1980).

[94] M. Poot and H. S. J. van der Zant, Appl. Phys. Lett. **92**, 063111 (2008)

[95] X.-L. Qi, Y.-S. Wu, and S.-C. Zhang, Phys. Rev. B **74**, 085308 (2006).

[96] X.-L. Qi, T. L. Hughes, S. Raghu, and S.-C. Zhang, Phys. Rev. Lett. **102**, 187001 (2009).

[97] N. Read and D. Green, Phys. Rev. B **61**, 10267 (2000).

[98] N. Read and A. W. W. Ludwig, Phys. Rev. B **63**, 024404 (2000).

[99] R. M. Ribeiro, Vitor M. Pereira, N. M. R. Peres, P. R. Briddon, and A. H. Castro Neto, New J. Phys. **11**, 115002 (2009).

[100] H. J. Rothe, *Lattice gauge theories*, World Scientific Lecture Notes in Physics, Vol. 74 (2005).

[101] R. Roy, Phys. Rev. Lett. **105**, 186401 (2010)

[102] S. Russo, M. F. Craciun, M. Yamamoto, A. F. Morpurgo, and S. Tarucha, Phys. E **42**, 677 (2010); B. E. Feldman, J. Martin, and A. Yacoby, Nature Physics **5**, 889 (2009).

[103] S. Ryu, A. P. Schnyder, A. Furusaki, and A. W. W. Ludwig, New J. Phys. **12**, 065010 (2010).

[104] S. Sapmaz, Ya. M. Blanter, L. Gurevich, and H. S. J. van der Zant, Phys. Rev. B **67**, 235414 (2003).

[105] M. Sato, Y. Takahashi, and S. Fujimoto, Phys. Rev. Lett. **103**, 020401 (2009).

[106] J. D. Sau, R. M. Lutchyn, S. Tewari, and S. Das Sarma, Phys. Rev. Lett. **104**, 040502 (2010).

[107] A. V. Savin and Y. S. Kivshar, Appl. Phys. Lett. **94**, 111903 (2009).

[108] A. Schuessler, P. M. Ostrovsky, I. V. Gornyi, and A. D. Mirlin, Phys. Rev. B **79**, 075405 (2009).

[109] T. Senthil and M. P. A. Fisher, Phys. Rev. B **61**, 9690 (2000).

[110] W. Shockley, Phys. Rev. **56**, 317 (1939).

[111] P. G. Silvestrov and K. B. Efetov, Phys. Rev. B **77**, 155436 (2008).

[112] T. Stauber, N. M. R. Peres, and A. H. Castro Neto, Phys. Rev. B **78**, 085418 (2008).

[113] R. Stacey, Phys. Rev. D **26**, 468 (1982).

[114] M. Starzak and S. Ledakowicz, Chem. Eng. J. **32**, 15 (1986).

[115] H. Suzuura and T. Ando, Phys. Rev. B **65**, 235412 (2002).

[116] S. Tewari, S. Das Sarma, C. Nayak, C. Zhang, and P. Zoller, Phys. Rev. Lett. **98**, 010506 (2007).

[117] W.-R. Hannes and M. Titov, EPL **89**, 47007 (2010).

[118] J. Tworzydlo, B. Trauzettel, M. Titov, A. Rycerz, and C. W. J. Beenakker, Phys. Rev. Lett. **96**, 246802 (2006).

[119] J. Tworzydło, C. W. Groth, and C. W. J. Beenakker, Phys. Rev. B **78**, 235438 (2008).

[120] J. Velasco Jr., G. Liu, W. Bao, and C. N. Lau, New J. Phys. **11**, 095008 (2009).

[121] A. Vishwanath, Phys. Rev. Lett. **87**, 217004 (2001).

[122] G. E. Volovik, *The Universe in a Helium Droplet* (Oxford University Press, 2009).

[123] G. E. Volovik, JETP Lett. **67**, 1804 (1988); JETP Lett. **66**, 522 (1997).

[124] G. E. Volovik, JETP Lett. **70**, 601 (1999).

[125] F. Wegner, Nucl. Phys. B **316**, 663 (1989); S. Hikami, Nucl. Phys. B **215** [FS7], 555 (1983).

[126] K. G. Wilson, Phys. Rev. D **10**, 2445 (1974).

[127] M. Wimmer, A. R. Akhmerov, M. V. Medvedyeva, J. Tworzydło, and C. W. J. Beenakker, Phys. Rev. Lett. **105**, 046803 (2010).

[128] L. M. Woods and G. D. Mahan, Phys. Rev. B **61**, 10651 (2000).

[129] Y. Zhang, Y.-W. Tan, H. L. Stormer, P. Kim, Nature **438**, 201 (2005).

[130] S. Y. Zhou, G.-H. Gweon, A. V. Fedorov, P. N. First, W. A. de Heer, D.-H. Lee, F. Guinea, A. H. Castro Neto, and A. Lanzara, Nature Mat **6**, 770 (2007).

[131] K. Ziegler, Phys. Rev. Lett. **102**, 126802 (2009); Phys. Rev. B **79**, 195424 (2009).

[132] K. Ziegler and A. Sinner, Phys. Rev. B **81**, 241404(R) (2010).

Samenvatting

Dit proefschrift is gewijd aan het effect van wanorde in twee-dimensionale systemen van Dirac fermionen. Deze quasi-deeltjes komen voor in grafeen (monolagen van koolstofatomen), in supergeleiders waarbij de orde parameter een p-golf of d-golf symmetrie heeft en in topologische isolatoren.

We richten onze aandacht op een specifiek gevolg van deze wanorde, namelijk het verschijnsel van lokalisatie. Het is bekend dat gewone elektronen (wier gedrag beschreven wordt door de Schrödinger vergelijking, en niet door de Dirac vergelijking), gelokaliseerd worden onder invloed van wanorde. Concreet betekent dit dat de golffunctie van een excitatie exponentieel vervalt, en geen uitgebreide vlakke golf is. Lokalisatie maakt zodoende van een metaal een isolator.

De reactie van Dirac fermionen op wanorde is kwalitatief anders dan die van gewone elektronen. Al vroeg is ontdekt dat Dirac fermionen niet gelokaliseerd kunnen worden met behulp van elektrostatische wanorde, als deze wanorde glad is op de schaal van de roosterconstante. In dit proefschrift concentreren we ons op een ander type wanorde, die in de Dirac vergelijking optreedt als een plaatsafhankelijke massa. In grafeen ontstaat dit door wanorde in het substraat. Tegen de verwachtingen van eerder onderzoek in, hebben we ontdekt dat door een wanordelijke massa in grafeen er geen overgang plaatsvindt naar een metallische toestand. Alle golffuncties blijven dus gelokaliseerd en grafeen is isolerend.

De situatie is volledig anders voor Dirac fermionen in een p-golf supergeleider. In dit type supergeleiders verschijnt de plaatsafhankelijke massa in de Dirac vergelijking ten gevolge van elektrostatische wanorde. Voor zwakke wanorde is er lokalisatie, maar in tegenstelling tot onze bevindingen bij grafeen, vindt bij sterke wanorde een overgang naar een metallische toestand plaats.

Met behulp van een roostermodel van zogenaamde “staggered” fermionen, dat voortkomt uit de kwantumchromodynamica, onderzoeken we

de metaal-isolator overgang in p-golf supergeleiders. We berekenen de kritische exponent en identificeren een afstotend trikritisch punt in het fasediagram.

Het kwalitatieve verschil tussen het gevolg van wanorde in het gedrag van Dirac fermionen in grafeen en in p-golf supergeleiders vraagt om een verklaring. Deze vinden we in de aanwezigheid van gebonden Majorana toestanden in de p-golf supergeleider. Deze "mid-gap" excitaties in p-golf supergeleiders maken resonant tunnelen en een metallische toestand mogelijk. Grafeen heeft geen gebonden Majorana toestanden en dus geen metallische toestand in de aanwezigheid van een wanordelijke massa.

Elektrostatische wanorde in een d-golf supergeleider manifesteert zichzelf op een volledig andere wijze, namelijk als een wanordelijke vector potentiaal in de Dirac vergelijking. Met behulp van een ijktransformatie kan dit type wanorde worden verwijderd op het Fermi niveau, mits de wanorde glad is op de schaal van de roosterconstante. Hieruit volgt dat de transmissie van Dirac fermionen door een d-golf supergeleider slechts beperkt beïnvloed wordt door lange-dracht fluctuaties in de elektrostatische potentiaal. Fluctuaties van korte dracht hebben wel een sterk effect. Zij onderdrukken exponentieel de elektrische stroom die gedragen wordt door de excitaties, terwijl ze de thermische stroom niet beïnvloeden.

In het laatste hoofdstuk van dit proefschrift keren we terug naar grafeen, en bestuderen we twee van zijn prominente eigenschappen, namelijk het vormen van een sterk geleidend twee-dimensionaal elektronengas en tegelijkertijd het vormen van een mechanisch stabiel membraan. Het samenspel tussen de elektrische en mechanische eigenschappen wordt bestudeerd door het berekenen van de verandering van de geleidbaarheid van opgehangen grafeen als gevolg van de vervorming door een "gate" elektrode.

Summary

This thesis is devoted to the effects of disorder on two-dimensional systems of Dirac fermions. These quasiparticles appear in condensed matter in graphene (carbon monolayers), and also in superconductors with p-wave or d-wave symmetry of the order parameter, as well as in topological insulators.

The effect of disorder on which we focus our attention is the phenomenon of localization. It is known that ordinary electrons (described by the Schrödinger equation, rather than the Dirac equation) are localized by disorder, meaning that the wave function of an excitation decays exponentially, rather than being an extended plane wave. Localization thus transforms a metal into an insulator.

Dirac fermions respond qualitatively different to disorder. An early discovery was that electrostatic disorder cannot localize Dirac fermions in graphene, if it is smooth on the scale of the lattice constant. We concentrate on a different type of disorder, namely on a random mass term in the Dirac equation. It is realized in graphene by randomness in the substrate. We have discovered, somewhat unexpectedly in view of earlier work on this problem, that Dirac fermions in graphene are localized by a random mass, without any transition into a metallic state.

The situation is entirely different for Dirac fermions in a p-wave superconductor. There electrostatic disorder appears in the Dirac equation as a random mass, which localizes the excitation, but only if the disorder is relatively weak. For large mass fluctuations a transition into a metallic state appears, in contrast to what we found in graphene. We investigate the metal-insulator transition in p-wave superconductors using a lattice model of staggered fermions (originally proposed in the context of QCD). We calculate the critical exponents and identify a repulsive tricritical point at the phase diagram.

The qualitatively different response to disorder of Dirac fermions in

graphene and in p-wave superconductors calls for an explanation, which we find in the appearance of Majorana bound states.

These midgap excitations in a p-wave superconductor allow for resonant tunneling and a metallic state. Graphene has no Majorana bound states, hence no metallic state in the presence of a random mass.

Electrostatic disorder in a d-wave superconductor manifests itself in an alltogether different form, as a random vector potential in the Dirac equation. A gauge transformation can eliminate this type of disorder at zero energy, if it is smooth on the scale of the lattice constant. The transmission of Dirac fermions through a d-wave superconductor is therefore only slightly affected by long-range electrostatic potential fluctuations. Short-range fluctuations do have a strong effect, exponentially suppressing the electrical current carried by the excitations, while leaving the thermal current unaffected.

We return to graphene in the final chapter of the thesis, to study two of its prominent properties: it forms a highly conducting two-dimensional electron gas and at the same time is a mechanically stable membrane. The interplay of electrical and mechanical properties is studied by calculating the correction to the conductivity of suspended graphene due to its deformation by a gate electrode.

List of Publications

- *Cyclotron enhancement of tunneling* , M. V. Medvedeva, I. A. Larkin, S. Ujevic, L. N. Shchur, and B. I. Ivlev, Phys. Rev. B **78**, 165325 (2008).

- *Hartman effect and spin precession in graphene*, R. A. Sepkhanov, M. V. Medvedyeva, and C. W. J. Beenakker, Phys. Rev. B **80**, 245433 (2009).

- *Absence of a metallic phase in charge-neutral graphene with a random gap* , J. H. Bardarson, M. V. Medvedyeva, J. Tworzydło, A. R. Akhmerov, and C. W. J. Beenakker, Phys. Rev. B **81**, 121414(R) (2010) [Chapter 3].

- *Majorana bound states without vortices in topological superconductors with electrostatic defects*, M. Wimmer, A. R. Akhmerov, M. V. Medvedyeva, J. Tworzydło, and C. W. J. Beenakker, Phys. Rev. Lett. **105**, 046803 (2010) [Chapter 4].

- *Effective mass and tricritical point for lattice fermions localized by a random mass*, M. V. Medvedyeva, J. Tworzydło, and C. W. J. Beenakker, Phys. Rev. B **81**, 214203 (2010) [Chapter 2].

- *Piezoconductivity of gated suspended graphene*, M. V. Medvedyeva and Ya. M. Blanter, Phys. Rev. B **83**, 045426 (2011) [Chapter 6].

- *Effects of disorder on the transmission of nodal fermions through a d-wave superconductor*, J. K. Asbóth, A. R. Akhmerov, M. V. Medvedyeva, and C. W. J. Beenakker, to be published in Phys. Rev. B [Chapter 5].

Curriculum Vitæ

I was born in Dnipropetrovsk, Ukraine on the 9th of June 1985, where I also received my primary and secondary education. During my school years I participated in the science competitions for Physics, Chemistry, and Mathematics, winning prizes at the regional level and for Physics also at the national level. In the last year of the secondary school my research project on analogues of geometrical equalities and nonequalities in non-Euclidean geometry was awarded the first prize at the national level.

In 2002 I entered the Faculty of General and Applied Physics of the Moscow Institute of Physics and Technology. In 2006 I received my Bachelor degree with a thesis on *Enhancement of tunneling in magnetic field*, under the supervision of professors Boris Ivlev and Lev Shchur. The Masters diploma followed in 2008 with the thesis *Cyclotron enhancement of tunneling*. During the last three years at the University I took part in a special project on computational physics, constructing and administrating a computer cluster at the Landau Institute for Theoretical Physics in Chernogolovka.

After graduating I joined the group of prof. Carlo Beenakker at Leiden University, employed by the *Foundation for Fundamental Research on Matter* (FOM), to pursue the research reported in this thesis. Part of my research was carried out together with experimentalists at the Delft University of Technology, in the context of a FOM research program on graphene.

As a Ph.D. student I have attended summer schools in Les Houches and Windsor, and presented my work at seminars and conferences in Italy, Sweden, and the United Kingdom. I also participated in the 2010 Lorentz Center Workshop on "Physics with Industry".

Stellingen

behorende bij het proefschrift

On localization of Dirac fermions by disorder

1. The phase diagram of a chiral p-wave superconductor has a *repulsive* tricritical point.

   This thesis, Chapter 2.

2. A sheet of graphene with a spatially varying band gap has no metallic phase.

   This thesis, Chapter 3.

3. Unlike the electrical quantum Hall effect, the thermal quantum Hall effect is destroyed by strong impurity scattering.

   This thesis, Chapter 4.

4. The transmission probability of nodal fermions in a d-wave superconductor is unaffected by intra-node scattering.

   This thesis, Chapter 5.

5. A magnetic field can increase the tunnelling probability of an electron by an order of magnitude.

   M. V. Medvedyeva, I. A. Larkin, S. Ujevic, L. N. Shchur, and B. I. Ivlev, Phys. Rev. B **78**, 165325 (2008).

6. The transmission time over a distance L of massless electrons (having velocity v) in undoped graphene equals $0.9L/v$.

   R. A. Sepkhanov, M. V. Medvedyeva, and C. W. J. Beenakker, Phys. Rev. B **80**, 245433 (2009).

7. The Josephson effect in graphene can coexist with the quantum Hall effect if the superconducting electrodes are narrower than the magnetic length.

8. The gauge-gravity (AdS/CFT) duality suggests a purely geometric mechanism for superconductivity, not mediated by any quasiparticle.

9. Using only the front part of the foot when running both prevents and cures knee injuries.

10. Creativity can be easily reduced by applying pressure.

Mariya Medvedyeva,
3 May 2011